UNIVERSIDADE DE SANTIAGO DE COMPOSTELA

FACULTADE DE FÍSICA

DEPARTAMENTO DE FÍSICA DA MATERIA CONDENSADA

Laboratorio de Baixas Temperaturas e Supercondutividade (LBTS)

PhD THESIS

Superconducting pair condensation and phase coherence in cuprates: experimental determination of the corresponding phase diagram in $La_{2-x}Sr_xCuO_4$

Author:
Noelia Cotón Sánchez

PhD supervisors:
Manuel Vázquez Ramallo
Félix Vidal Costa

Santiago de Compostela, May 2013

USC
UNIVERSIDADE
DE SANTIAGO
DE COMPOSTELA

Dr. Félix Vidal Costa, Catedrático do Departamento de Física da Materia Condensada da Universidade de Santiago de Compostela e **Dr. Manuel Vázquez Ramallo**, Profesor Titular do Departamento de Física da Materia Condensada da Universidade de Santiago de Compostela,

CERTIFICAN

Que a presente memoria titulada *Superconducting pair condensation and phase coherence in cuprates: experimental determination of the corresponding phase diagram in* $La_{2-x}Sr_xCuO_4$ foi realizada por **Dª Noelia Cotón Sánchez** baixo a súa dirección no Departamento de Física da Materia Condensada da Universidade de Santiago de Compostela e constitúe a Tese que presenta para optar ao título de Doutor pola Universidade de Santiago de Compostela.

Santiago de Compostela, maio de 2013

Félix Vidal Costa
Director da tese

Manuel Vázquez Ramallo
Director da tese

USC
UNIVERSIDADE
DE SANTIAGO
DE COMPOSTELA

Aos meus pais, á miña irmá
e a Ronald.

USC
UNIVERSIDADE
DE SANTIAGO
DE COMPOSTELA

Acknowledgments

Almost at the end of this stage, I would like to thank some people and institutions for their support and help. Without them this PhD thesis would have not been possible.

First, I acknowledge Professor Félix Vidal for the supervision of this thesis and his guidance in both the specific and the general research issues leading to this work. His scientific knowledge and his experience have been crucial at any time to take decisions. Second, but no less important, I would like to acknowledge Dr. Manuel V. Ramallo who has also supervised this PhD thesis. His inestimable help and orientation have been pivotal, because thanks to him I have learnt almost all I know about superconductivity.

I would also like to acknowledge the rest of the LBTS group for their support, especially to Jesús Mosqueira, for his help with the SQUID measurements and with the susceptibility analyses. The other Drs. of the group, Carolina, Carlos, Antonio and Jesús were also kind with me when I needed their help. I do not want to forget both Juanjo, for his help with the PPMS measurements, and Turnes, the technician of our lab. orientation have been crucial, because thanks to him I have learnt almost all I know about superconductivity.

A very important part of this work took place at the CRISMAT Laboratory in Caen (France) in 2010 and 2011. I would like to express my gratitude to Professor Bernard Mercey for his advice during the fabrication of the samples and to Dr. Conor McLoughlin because his help was fundamental during my two internships there. I do not want to forget my colleagues there (Pierre, Vengadesh, Alice, Claudy and Anne) and also the rest of people from CRISMAT who helped me because, in some way or another, they made that my stay there was a nice experience. orientation have been crucial, because thanks to him I have learnt almost all I know about superconductivity.

The works leading to this PhD thesis and all the related published papers were supported by the Ministerio de Ciencia e Innovación under projects FIS2007-63709 (MEC-FEDER), FIS2010-19807 (MICINN-FEDER), and by the Xunta de Galicia under projects

2010/XA043 and 10TMT206012PR. I also acknowledge the financial support of MICINN during four years trough a FPI grant. Additional funds for conferences and meetings were supplied by European Union under the ENERMAT project.

Durante estes case seis anos tamén houbo tempo para divertirse e niso foron cruciais os meus compañeiros no LBTS, os que xa se marcharon: Manuel, Zalo, Diego e Javier; e os que quedan: Ramón, Juan e Alberto. Sen eles, sen dúbida esta experiencia non tería sido a mesma. Por outra parte, este traballo nunca existiría se non fora polos ánimos dos meus compañeiros e amigos da carreira Bea, Xabi e Álex, que me animaron a comezar neste mundo da investigación. Tamén me acompañaron nesta aventura de doutorarse os meus amigos do DEC (agora Citius) e que coñecín gracias a Bea. Eles tamén me escoitaron e apoiaron cando fixo falta.

Por suposto, os meus amigos de sempre non poden deixar de ser mencionados, xa que aínda que non comprendan moi ben que é o que fixen durante este tempo, nin exactamente como funciona este mundo da investigación, sempre se preocuparon por como me ía e escoitaban as miñas historias con atención e curiosidade. Estas persoas son Bea e Irene, Raquel, Ana, Paula, Amaro e Fernando, así como un amplo sector da miña familia, básicamente os meus primos e tíos que non nomeo porque sería unha lista bastante longa.

Deixo para o final dos agradecementos ás persoas máis importantes na miña vida, pois sen eles, si que de verdade esta tese non sería unha realidade. Aos meus pais e á miña irmá Belén, agradézolles o seu continuo apoio e a súa comprensión ante as moitas dúbidas que lles surxían a causa deste traballo. E a Ronald, a persoa que sempre está aí cando a necesito, e que é un piar fundamental na miña vida. Doulle as gracias por escoitarme e aconsellarme cando lle contaba as miñas dificultades, pois as súas palabras e o seus feitos facían que automáticamente me sentira mellor.

"Science is the belief in the ignorance of the experts"

Richard Feynman.

"To measure is to know"

Lord Kelvin.

"The education of young people in science is at least as important, maybe more so, than the research itself"

Glenn Theodore Seaborg.

USC
UNIVERSIDADE
DE SANTIAGO
DE COMPOSTELA

Contents

USC
UNIVERSIDADE
DE SANTIAGO
DE COMPOSTELA

Chapter 1

Background, context and aims of this study

1.1 Introduction

The understanding of the critical phenomena around the superconducting transition of high-temperature superconductors (HTS) is a crucial first step to describe the mechanisms leading to the superconducting pairing in these materials. [1–11] Up to some years ago, research in both thematics advanced rather independently from each other, in correspondence with the fact that most of the predictions of the theories for critical fluctuations, such as the Gaussian-Ginzburg-Landau or the renormalization group approaches, are mostly universal and independent of the microscopic interactions responsible of pairing.[1]

Recently, both topics have increasingly become most closely interrelated with each other, mainly because of the emergence of interest in unambiguously locating the transition temperatures for phase coherence and condensation of the superconducting wave function (T_{phase} and T_{cond} respectively) and their distance to the temperature T_{c} at which the macroscopic superconducting phenomenology appears. [1–3, 20–36] This yet open question has become of pivotal importance due to the proposals (and their large popularity) by various groups, [3, 20–28] according to which in HTS the transition to macroscopic superconductivity could be driven by strong fluctuations of the phase of the order parameter. In that so-called "strong phase fluctuations" scenario, and contrarily to what happens in conventional low-temperature superconductors,[2] the wave function

[1] Nonetheless, some precedents do exist in which the study of the superconducting fluctuations and of the superconducting gap in HTS shared specific problems of research: for instance, the role of CuO_2 laminarity, [9, 12–16] the *d*-wave symmetry of the pairing, [9, 15–18] or the relaxation time of the superconducting wave function. [19]

[2] In the low-temperature superconductors, as it is well known [37–47] in regular bulk samples T_{cond}, T_{phase} and T_{c} are experimentally indistinguishable from each other. In some thin films, the difference

condensation would happen at temperatures $T_{\rm cond}$ much larger than both $T_{\rm phase}$ and $T_{\rm c}$, being in particular $T_{\rm phase} \simeq T_{\rm c}$, and $T_{\rm cond} - T_{\rm c}$ of the order of tens or even hundreds of Kelvin (depending on the author and specific HTS composition). [3, 20–28] Importantly, if $T_{\rm cond} \gg T_{\rm phase}$ the search for the mechanism behind *macroscopic* superconductivity (and also the quest of increasing $T_{\rm c}$) should focus in the correlations between pre-formed vortices, rather than of between single-particle normal-state carriers. Naturally, also the critical phenomena associated to the transition should be very different from the one in conventional low-temperature superconductors. [3,9–11,20,43] On the contrary, moderate values of $T_{\rm cond} - T_{\rm phase}$ (of $\sim$ 5K or less) would favour an scenario of "conventional fluctuations", and then a pairing at $T_{\rm c}$ dominated by the interactions between single-particle normal-state carriers. [5, 30, 48–58]

Up to now, most experimentalists addressing the issue of testing the strong phase fluctuations scenario have searched for traces of precursive vortex-like features well above the macroscopic superconducting transition, that would confirm a $T_{\rm cond} \gg T_{\rm phase}$. [23–29] However, the so-resulting possible positive confirmations have been challenged by plausible alternative explanations in terms, *e.g.*, of chemical disorder and its resulting inhomogeneities of critical temperatures, [34–36] or also in terms of the magnetic-field dependence of different forms of normal-state, non-superconducting orders [30, 50–53, 55, 58].

The main aim of this PhD thesis is to explore this problem by means of simultaneous measurements of two exclusive features expected to occur in the voltage-current ($V - I$) characteristics near $T_{\rm phase}$ and $T_{\rm cond}$: The jump from ohmic behaviour up to $V \propto I^3$ (the so-called Nelson jump) at $T_{\rm phase}$, and for $T_{\rm cond}$ the critical rounding of the ohmic resistivity due to critical superconducting fluctuations. In order to obtain unambiguous results, it is important to perform these measurements in a sample set with a range of doping levels covering the underdoped, optimally-doped and overdoped regions. It is also crucial to characterize as comprehensively as possible the effects of critical temperature inhomogeneities, both by growing particularly homogeneous samples and by carefully characterizing the effects of the unavoidable remaining inhomogeneities on the measured $V-I$ curves. These aspects allow us to improve on earlier measurements by other authors in the cuprates $Tl_2Ba_2CaCu_2O_8$ [59], $YBa_2Cu_3O_7$ [60] and $Bi_2Sr_2CaCu_2O_8$ [61–63] who measured the Nelson jump and the resistivity rounding, but did not measure them as a function of doping nor have taken into account the effects of the critical temperature inhomogeneities. Our work also extends earlier results of our group in $La_{2-x}Sr_xCuO_4$ thin films that were centered only on the resistivity rounding. [64]

With those objectives, we present in this work the following developments:

i) In chapter 2, we report the implementation of a new method to grow $La_{2-x}Sr_xCuO_4$ films (of thickness $\sim$ 200 nm and over $SrTiO_3$ substrates) with arbitrary dopings $0.09 \lesssim x \lesssim 0.22$ based on simultaneous pulsed laser deposition from two targets as parent ox-

$T_{\rm cond} - T_{\rm phase}$ may increase, but only up to $\sim$ 3K. [37–42] It is also interesting to note that, in fact, the first and main experimental check of these values of $T_{\rm cond}$ and $T_{\rm phase}$ were obtained on the grounds of voltage-current measurements [37–42] similar to the ones that the present PhD thesis aims to perform in HTS.

ides.[3] This chapter also describes basic characterization measurements (XRD, AFM, SEM, EDX) of these films, that indicate a good structural quality. We also measure the homogeneity of the macroscopic superconducting critical temperature T_c by means of high-resolution SQUID magnetometry, that allows to determine not only the average value $\overline{T}_c$ but also the dispersion due to inhomogeneities, ΔT_c, in each sample. These measurements show that the superconducting homogeneity of these films is among the best reported up to now in $La_{2-x}Sr_xCuO_4$ samples, including bulks [34, 35, 65, 66] and single crystals [67]. In fact, it is also shown that their ΔT_c dispersions are in most cases at a level comparable to the minimum, unavoidable disorder due to intrinsic randomness in the Sr-ion locations (the so-called intrinsic chemical disorder). [34, 35, 65]

ii) In chapter 3, with the aim of identifying measurable features able to unambiguously locate T_{cond} and T_{phase} we calculate, to our knowledge for the first time and by using both numerical finite-element simulations and effective-medium approaches, the influence of a random distribution of critical temperatures in the electrical transport response of a planar superconductor near the superconducting transition, including also temperatures close to T_{cond} and T_{phase}. We particularly focus on the exponent α of the $(V - I)$ curves $V \propto I^{\alpha}$ and on the ohmic resistance V/I when $\alpha = 1$. In a homogeneous 2D superconductor, α displays a sharp jump at T_{phase} from the ohmic behaviour $\alpha = 1$ up to $\alpha = 3$ (the so-called Nelson jump), this being a particularly exclusive signature of a phase coherence transition. [43] Our studies reveal that the presence of random superconducting inhomogeneities does not appreciably shift the temperature location of the condition $\alpha = 3$, that determines then with excellent accuracy the average $\overline{T}_{phase}$. We also derive an effective-medium expression for the critical rounding of the ohmic resistivity due the fluctuating vortices and superconducting carriers above $\overline{T}_{phase}$ in presence of inhomogeneities.

iii) In chapter 4, we present the measurement in our films of the experimental features suggested in chapter 3, and discuss the results. In particular, we measure the $V - I$ characteristics as a function of temperature, obtaining the exponent α in $V \propto I^{\alpha}$ and also the ohmic resistance V/I when $\alpha = 1$. Direct exploration of the condition $\alpha = 3$ in these measurements allows us to plot a phase diagram for T_{phase} as a function of doping x. The phase diagram for $T_{cond}(x)$ is also obtained, by means of comparing the measured ohmic resistivity near the transition with our effective-medium calculations for the critical rounding of the resistivity. Both the $T_{cond}(x)$ and $T_{phase}(x)$ lines result to be parabolas (with a slight depression near $x = 1/8$) that for all dopings are not further away than $\sim$ 4K from the $T_c(x)$ line in which the macroscopic superconducting phenomenology (*e.g.*, the full Meissner effect) appears. These small differences between T_{cond}, T_{phase} and T_c for the underdoped, optimally-doped and overdoped samples suggest theoretical scenarios different from the strong phase-fluctuation pairing models, [3,20–22] in which T_c is primarily determined by the vortex-antivortex binding instead of the pairing between

[3]The synthesis of these films was performed during a stay at the Laboratoire CRISMAT, ENSICAEN, Université de Caen Basse-Normandie (France), under the direct supervision of Prof. B. Mercey of that Laboratory. Some preliminary analyses of these samples (including structural characterization measurements such as profilometry, XRD, SEM and EDX measurements) were done also during that stay in order to confirm the good obtainment of the films. The rest of the work described in this thesis was performed at the LBTS Laboratory of the Universidade de Santiago de Compostela (Spain).

single-particle normal carriers (*i.e.*, $T_{\mathrm{cond}} \gg T_{\mathrm{phase}}$ and $T_{\mathrm{phase}} \simeq T_{\mathrm{c}}$). Our results are coherent instead with pairing models in which both $T_{\mathrm{cond}} - T_{\mathrm{phase}}$ and $T_{\mathrm{cond}} - T_{\mathrm{c}}$ are small ($\lesssim 5\mathrm{K}$) for all dopings. [5, 30, 48, 49, 51–58]

We devote the remaining of this introductory chapter to provide in section 1.2 a more detailed definition of the characteristic temperatures T_{phase} and T_{cond}, and in section 1.3 a summary of the main existing proposals for their location in the phase diagram of the HTS cuprates.

1.2 Overview of the characteristic temperatures for the fluctuations in a 2D superconductor: T_{phase}, T_{cond}, T_{LG} and T^{C}

To further and more precisely introduce and contextualize our research subject, let us present here a descriptive discussion of the main characteristic temperatures related to the superconducting transition and the superconducting fluctuations in a type-II two-dimensional (2D) homogeneous superconductor without any applied magnetic field.

Let us emphasize that this description is general for both the "strong phase fluctuations" scenario and the "conventional fluctuations" scenario. The differences between both of them will lie in the specific values of these characteristic temperatures, specially the distance between T_{phase} and T_{cond} (see section 1.3).

1.2.1 The transition without fluctuation effects

We begin by briefly considering the simple preliminary case in which fluctuation effects are negligible. Then, naturally the superconducting wave function Ψ is simply null above a certain critical temperature, which for convenience we note as T_{cond} (superconducting wave function condensation temperature). Below T_{cond}, Ψ takes a temperature-dependent value of positive modulus and arbitrary phase. In other words, this case just corresponds to the usual textbook solution [10] that results from minimizing the Ginzburg-Landau (GL) superconducting free energy $\Delta F[\Psi]$. Note that any spatial variation of Ψ would contribute positively to $\Delta F[\Psi]$ (the associated term in the GL model being $\propto |\nabla\Psi|^2$) and therefore both the modulus and the phase of Ψ below T_{cond} are spatially uniform. [10] We illustrate this simple case in figure 1.1.

1.2.2 Splitting of the transition into T_{phase} and T_{cond}

In figure 1.2, we now include the fluctuation effects associated to the close proximity to the transition. We continue to define T_{cond} as the temperature at which the value of Ψ minimizing $\Delta F[\Psi]$ is first nonzero. In other words, it corresponds to the temperature at which it first becomes energetically favourable to form superconducting pairs. However,

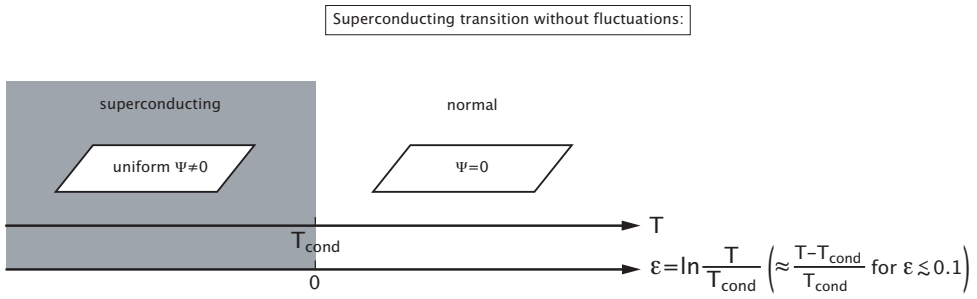

Figure 1.1: Scheme of the characteristic temperatures in the superconducting transition of a planar superconductor without fluctuations.

due to fluctuations, those pairs may already exist above $T_{\rm cond}$, corresponding to the configurations of Ψ not making $\Delta F[\Psi]$ minimum.[4] Sufficiently above $T_{\rm cond}$, the fluctuation effects will be describable as small (Gaussian) perturbations. [10, 68] This forms the basis of the so-called Gaussian-Ginzburg-Landau (GGL) approach. The GGL predictions are usually given in terms of the reduced-temperature $\varepsilon \equiv \ln(T/T_{\rm cond})$, which can be approximated as $\varepsilon \simeq (T - T_{\rm cond})/T_{\rm cond}$ for small values $\varepsilon \lesssim 0.1$. [10, 68] The region of validity of the GGL approach (GGL region) is located at reduced-temperatures above a certain value, $\varepsilon \gtrsim \varepsilon_{\rm LG}$, where we use the subindex LG in recognition of the pioneering works by Levanyuk [69] and Ginzburg [70] who first considered it. These authors also produced an estimation criterion for $\varepsilon_{\rm LG}$ by comparing the mean-field heat capacity jump and the fluctuation heat capacity; when applied to the layered HTS, this criterion produces $\varepsilon_{\rm LG} \sim 10^{-2}$ [71] (so that the GGL region corresponds to $T > T_{\rm LG} \sim 1.01 T_{\rm cond}$). In the GGL region, the configurations of Ψ can be seen as (evanescent, time-dynamical) superconducting droplets or islands of $\Psi \neq 0$ values surrounded by a $\Psi = 0$ sea (see figure 1.2), the typical size of these islands being the Ginzburg-Landau coherence length $\xi(\varepsilon) = \xi(0)\varepsilon^{-1/2}$ where $\xi(0)$ is the GL amplitude in the planar direction. [10, 68] The term "amplitude fluctuations" is often associated to the GGL region [1–3, 20–28] so to emphasize that these configurations are not describable as topological excitations, *i.e.*, in terms of vortices. However, this name is also somewhat misleading, because both the amplitude and phase of Ψ fluctuate in the GGL region above the transition.[5]

When moving closer to the transition, for $\varepsilon < \varepsilon_{\rm LG}$, fluctuation effects become stronger

[4] Note that the statistically-averaged wave function is always a mean over all possible Ψ, each weighted by the Boltzmann factor $\omega[\Psi] \propto \exp(-\Delta F[\Psi]/k_{\rm B}T)$, where $k_{\rm B}$ is the Boltzmann's constant. [10, 68] Naturally, the statistical weight $\omega[\Psi]$ is maximum at the Ψ value that minimizes $\Delta F[\Psi]$, but when the $\omega[\Psi]$ peak broadens (*e.g.*, due to the proximity of $T_{\rm c}$) also Ψ configurations not minimizing $\Delta F[\Psi]$ contribute to the statistical averages. [10, 68]

[5] In fact, for $\varepsilon > \varepsilon_{\rm LG}$ both degrees of freedom contribute with equal weight to the fluctuating superfluid density. [72, 73]

and must be treated using full-critical approaches, such as the renormalization group method. [72] In the 2D case, as shown simultaneously by Berezinskii [44] and by Kosterlitz and Thouless [45] (BKT) in superfluids, and later by various workers in type-II superconductors (see, *e.g.*, [43, 46, 47]), the relevant excitations are topological and composed by vortices, even in absence of externally applied magnetic fields. Moreover, a crucial change on those vortex configurations occurs at a temperature usually known as "BKT temperature" or "phase coherence temperature", T_{phase}: [1–3, 20–29, 44, 45] At $T > T_{\mathrm{phase}}$ the vortices are essentially independent of each other, while at $T < T_{\mathrm{phase}}$ some vortices of opposite circulation bind together into pairs (vortex-antivortex pairs).[6] As first noted by BKT, [44, 45] T_{phase} is located below T_{cond} and it is at T_{phase} where the superconducting order parameter first gains long-range coherence.[7] This long-range coherence is a necessary requirement to fully display the usual macroscopic features of superconductivity, such as, *e.g.*, a complete Meissner effect. [1–3, 20–22, 43, 46, 47]

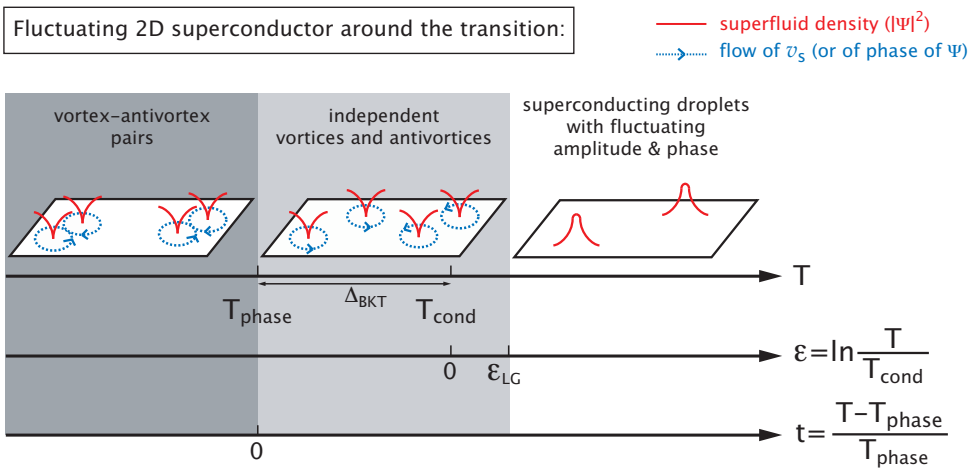

Figure 1.2: Schematic representation of the transition of a 2D superconductor with fluctuations around the two characteristic temperatures T_{phase} and T_{cond}. Sufficiently above T_{cond} the effects of fluctuations are weak and may be described in terms of the GGL theory. Below $\varepsilon_{\mathrm{LG}}$ the fluctuations are strong and may be explained in terms of vortices, that are essentially independent of each other above T_{phase}, and begin to bind into pairs of opposite circulation (vortex-antivortex pairs) below T_{phase}.

It has been argued that also for layered and three-dimensional (3D) superconductors the renormalization group leads to vortices as the relevant excitations of the supercon-

[6] It is probably noteworthy to note that the vortex-antivortex pairing happens in real space, contrarily to the conventional BCS pairing that occurs in momentum space.

[7] Or quasi-long-range order, in correspondence with Mermin and Wagner's theorem that states that in a 2D system with continuous symmetry there is no long-range order at finite temperature [74].

ducting wave function even without an external magnetic field. [75–80] These superconductors would then also experience a splitting of the transition into $T_{\rm cond}$ and $T_{\rm phase}$, although in this case the vortex pairings may be more complicated. For instance, in the 3D case the vortex-antivortex pairing is substituted by the interlacing of vortex loops, with a larger orientational freedom. [75–80] Moreover, while a solid estimate for the difference $T_{\rm cond}-T_{\rm phase}$ seems to be difficult in any dimensionality, it seems clear (*e.g.*, from experiments in low-$T_{\rm c}$ superconductors [37–42]) that the more 3D-like the superconductor is, the closer the temperatures $T_{\rm cond}$ and $T_{\rm phase}$ are to each other. [75–80]

1.2.3 The high-temperature limit $T^{\sf C}$ of the region of superconducting fluctuations

As earlier discussed by Gollub and coworkers in his pioneering work [81] (see also Refs. [9, 10]), the usual mean-field GGL approaches are formally valid only in the ε-region $\varepsilon_{\rm LG} \lesssim \varepsilon \ll 1$. Since then, different attempts have been proposed to extend to high-ε these mean field descriptions, including the introduction of different versions of the conventional momentum cutoff, [82] or an ad-hoc penalization (not a cutoff) of the short wavelength fluctuation modes which already takes into account the quantum localization. [83, 84] However, none of these early proposals lead to the vanishing of all fluctuation modes above a well-defined temperature, $T^{\sf C}$. Such a $T^{\sf C}$ was proposed in Ref. [85] by just taking into account the limits imposed by the Heisenberg uncertainty principle to the shrinkage, when the temperature increases above $T_{\rm cond}$, of the superconducting coherence length, $\xi(T)$, which cannot be smaller than $\xi_{T=0{\rm K}}$, the actual (or Pippard [86]) coherence length at $T = 0$K, *i.e.*,

$$\xi(T) \gtrsim \xi_{T=0{\rm K}}. \tag{1.1}$$

This condition directly leads to a well-defined $T^{\sf C}$ given by $\xi(T^{\sf C}) = \xi_{T=0{\rm K}}$, above which all the fluctuation modes are null. The corresponding cutoff reduced-temperature is then just $\varepsilon^{\sf C} \equiv \ln(T^{\sf C}/T_{\rm cond})$. Note also that the above condition is indeed compatible with the superconductivity in samples with sizes smaller than $\xi_{T=0{\rm K}}$, because, as earlier commented elsewhere [87] in such small superconductors the Pippard coherence length losses its conventional meaning (from a crude point of view, in these small superconductors the coherence length amplitude is also reduced with respect to the bulk value).

As also stressed in Ref. [85], the above condition is general, and must apply to any theoretical description of the superconducting transition. Only the value of $\varepsilon^{\sf C}$ will depend, through the temperature dependence of $\xi(T)$ and the relationship between $\xi(T)$ and $\xi_{T=0{\rm K}}$, on each particular approach. A relevant example will correspond to the combination of the mean-field temperature dependence of the coherence length, $\xi(T) = \xi(0)\varepsilon^{-1/2}$ (and then $\varepsilon^{\sf C} = (\xi(0)/\xi_{T=0{\rm K}})^2$), with the relationship between $\xi(T)$ and $\xi_{T=0{\rm K}}$ proposed by the mean-field BCS theory, which in the clean limit is $\xi(0) = 0.74\xi_{T=0{\rm K}}$. [88] This leads then to $\varepsilon^{\sf C} \approx 0.55$, *i.e.*, $T^{\sf C} \approx 1.7T_{\rm cond}$. [85, 89] A similar estimate using the dirty limit relationships, gives $\varepsilon^{\sf C} \simeq 0.6$. [11, 90] A useful way to introduce these ideas in the GGL approach is by means of a total-energy cutoff in the statistical averages as done in,

e.g., Refs. [64,89]: In units of $\hbar^2/(2m^*)$ (being $\hbar$ the reduced Plack constant and m^* the effective mass of the superconducting pairs),

$$k^2 + \xi^{-2}(\varepsilon) < \varepsilon^{c}\ \xi^{-2}(0), \tag{1.2}$$

where k^2 corresponds to the conventional momentum cutoff contribution, whereas $\xi^{-2}(\varepsilon)$ may be seen as a Heisenberg localization energy.

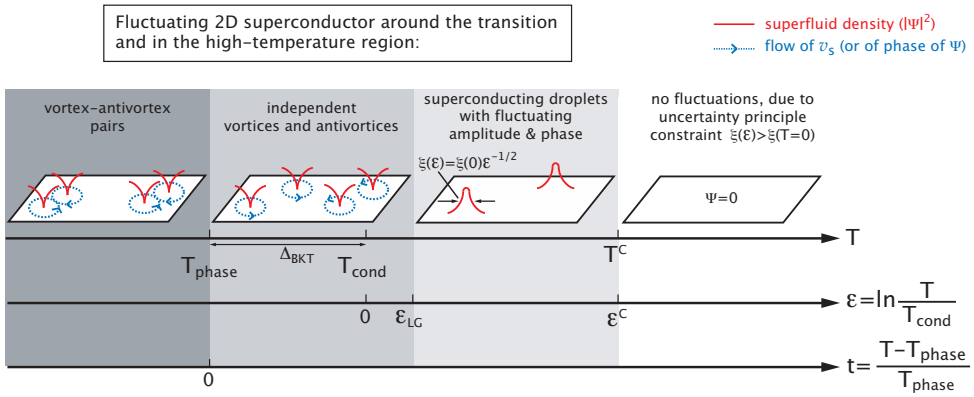

Figure 1.3: Main characteristic temperatures for the fluctuations in a 2D superconductor, including now also the high-temperature limit of the fluctuation region, T^{c}. Above T^{c} the fluctuations no longer exist because of the limit imposed by the uncertainty principle to the smallness of the coherence length (see main text for details).

1.3 Two possible scenarios for the phase diagram of $T_{\rm phase}$ and $T_{\rm cond}$ in the HTS

1.3.1 The "strong phase fluctuations" scenario

As already mentioned in section 1.1, the investigation of the mechanism of pairing in HTS has led various authors to propose the possibility of a $T_{\rm cond}$ larger than $T_{\rm phase}$ by various tens of Kelvin. In fact, these proposals are also linked to the related quest for understanding the normal state against which the pairing occurs and, in particular, the so-called "pseudogap" temperature $T_{\rm pgap}$ that appears in the phase diagram of cuprates. This temperature corresponds to the appearance of various experimental features indicating a depression of the density of states of normal carriers near the Fermi surface (DOS), *i.e.*, around $T_{\rm pgap}$ the normal-state carriers are removed from the states able of single-particle excitations (as shown, notably, by photoemission ARPES, Knight shift,

Hall effect and resistivity measurements, among other [91]). This DOS reduction seems to explain, at least qualitatively, a significative portion of the main anomalous features of the normal state of cuprates. [2, 91]

The proposal that $T_{\rm cond}$ could be in the HTS much larger than $T_{\rm phase}$ originated from exploring the idea that the new state into which normal carriers move when $T \simeq T_{\rm pgap}$ could be some form of pre-condensed, superconducting-like pairs, as expressed mainly by Emery and Kivelson [3] and then by other workers. [3, 20–29] The reason why these pairs would at first not lead to a macroscopic superconducting phenomenology is that the superconducting wave function formed by them would undergo strong fluctuations of its phase. [3] The macroscopic phenomenology would appear only once phase coherence establishes. Therefore, these proposals can be summarized by saying that $T_{\rm cond}$ would be essentially equal to $T_{\rm pgap}$, and $T_{\rm phase}$ would be essentially equal to the macroscopic superconducting critical temperature $T_{\rm c}$. [3, 20–29] We summarize that scenario in the main panel (a) of our figure 1.4. In that figure, and in the rest of this work, x stands for the doping level.[8] Note that the value of $T_{\rm pgap}$ varies strongly with doping x, and in particular in underdoped cuprates ($x < 0.16$) it is well larger than $T_{\rm c}$.[9] It is as yet unclear what is the $T_{\rm pgap}(x)$ line for optimally-doped ($x = 0.16$) and overdoped ($x > 0.16$) HTS compositions. In the main panel (a) of figure 1.4 we choose the option that for $x \geq 0.16$ it is $T_{\rm pgap} > T_{\rm c}$ as proposed in, *e.g.*, [91, 94], on the grounds of various experimental probes as, *e.g.*, Hall resistivity and Knight shift.

Other authors, such as [95–97], propose instead that for $x \geq 0.16$ it is $T_{\rm pgap} \leq T_{\rm c}$, based mainly on resistivity and heat-capacity measurements. In that case $T_{\rm cond}$ would be well larger than $T_{\rm phase}$ only for the underdoped compositions. We plot the phase diagram of this variation of the "strong phase fluctuation" scenario in panel (b) of figure 1.4.

Yet a third variation has been more recently proposed, [23–29] that we plot in panel (c) of figure 1.4. Now $T_{\rm cond}$ is not so directly identified with $T_{\rm pgap}$, but is given instead by the temperature at which some samples exhibit a relatively sharp change for the temperature and magnetic-field dependence of the Nernst coefficient, [25,26] the dc magnetization, [23, 24, 27, 28] or the derivatives of the dc resistivity [29]. The authors of these measurements attribute those effects to an onset of superconductivity due to the entrance into the $T < T_{\rm cond}$ region. Within this third scenario, it is unclear what would be the reason for the discrepancy between $T_{\rm cond}$ and $T_{\rm pgap}$, although two obvious possibilities would be that either *i)* the measurements are not sensitive enough as to detect a true smaller onset of the precursive superconductivity, so that the $T_{\rm phase}(x)$ line in panel (c) of figure 1.4 would actually correspond to a lower limit for that temperature, or *ii)* $T_{\rm phase}$ and $T_{\rm pgap}$ would not be related at all.

[8] More precisely, x is the density of holes per in-plane unit cell. For $La_{2-x}Sr_xCuO_4$, it coincides with the stoichiometric index for Sr (always at saturated oxygen contents). In general, the correspondence between x and the indexes of the stoichiometric formulae is specific to each HTS compound.

[9] Regarding the $T_{\rm c}(x)$ dependence, it is well known that it takes the form of a parabolic peak, centered around $x = 0.16$ and with a certain depression around $x = 1/8$ (often called "magical number doping"). [66, 92, 93] The values $x = 0.16$ and $1/8$ are universal for all the hole-doped HTS, while the deepness of the $x = 1/8$ depression depends on the particular compound.

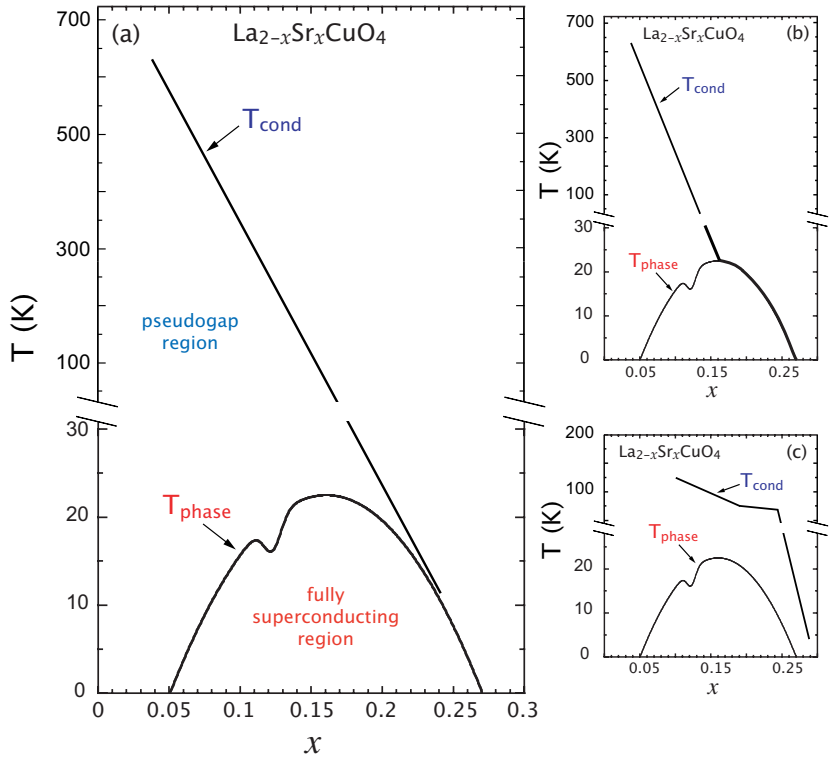

Figure 1.4: Three variations of the *"strong phase fluctuations"* scenario for the HTS. In the main panel (a) $T_{\rm cond}$ is essentially $T_{\rm pgap}$ and can be well larger than $T_{\rm phase}$, which is essentially $T_{\rm c}$. In this panel (a), $T_{\rm cond}$ and $T_{\rm pgap}$ are always above $T_{\rm phase}$ for all the superconducting dome. In panel (b) $T_{\rm pgap}$ can be below the superconducting dome for $x \gtrsim 0.13$, and then $T_{\rm cond}$ is the maximum of $T_{\rm pgap}$ and $T_{\rm c}$. In panel (c) $T_{\rm cond}$ is not so directly related to $T_{\rm pgap}$, but it is identified with an onset well above $T_{\rm c}$ of the temperature and magnetic field-dependence of several observables such as the Nernst effect (see main text for details).

1.3.2 The "conventional superconducting fluctuations" scenario

In the scenario of "conventional superconducting fluctuations", $T_{\rm cond}$ and $T_{\rm phase}$ are in HTS relatively close to each other for all the dopings (just like it would happen in a conventional low-temperature superconductor of similar dimensionality). In this case, both the $T_{\rm cond}(x)$ and $T_{\rm phase}(x)$ lines of the phase diagram should display parabolas roughly similar to the one of the appearance of macroscopic superconducting phenomenology $T_{\rm c}(x)$. These parabolas may be expected to be essentially parallel to each other with a distance $\Delta_{\rm BKT}$ below about 5K. This scenario is plotted in figure 1.5. In fact, the main

purpose of the present PhD thesis could be re-stated as "To try to determine what is the true scenario for the HTS, the one in figure 1.4, or the one in figure 1.5".

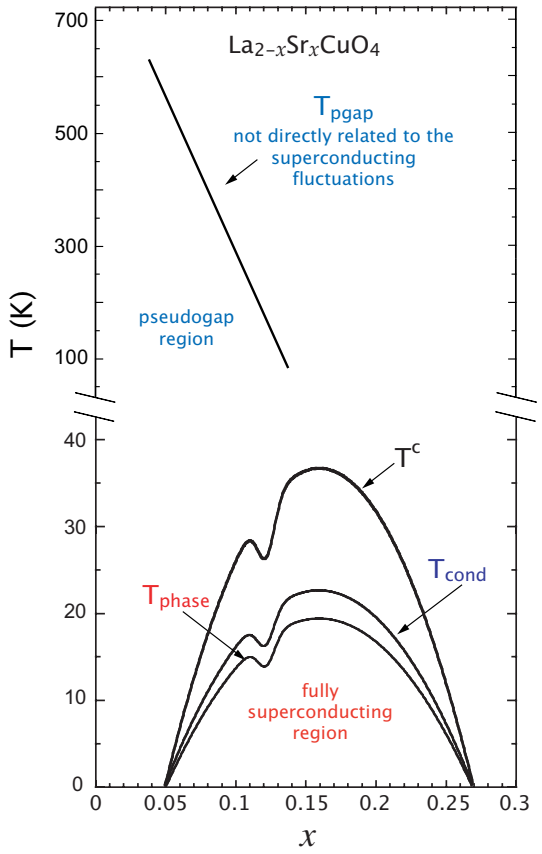

Figure 1.5: Scheme of the *"conventional superconducting fluctuations"* scenario for the phase diagram of HTS. In this situation, $T_{\rm cond}$ and $T_{\rm phase}$ are close to each other for all the dopings.

Within the scenario of "conventional superconducting fluctuations", it is natural to ask what could be the explanation for the experimental features observed well above $T_{\rm c}$ that led to propose the alternative strong phase fluctuations picture. In particular, whether it exists some alternative explanations other than $T_{\rm cond} \gg T_{\rm c}$ able to explain the $T_{\rm pgap}(x)$ lines in figures 1.4(a) and 1.4(b), and the line in figure 1.4(c) for the enhancement of the temperature and magnetic field-responses of the material. In fact, various alternative explanations have been proposed by different workers:

First of all, explanations for the line in figure 1.4(c) for the enhancement of the temperature and magnetic field-responses have been given in terms of trivial chemical disorder inducing inhomogeneities of the critical temperatures. For instance, it was shown in [34–36, 98] that even minute, and unavoidable, amounts of inhomogeneities may mimic the signals of precursive superconductivity observed by the authors of [23–29] and interpreted by them as evidences of $T_{\rm cond} \gg T_{\rm c}$. Notably, the explanation in terms of inhomogeneities would also account for the relevant observation that for HTS powders the onset features in the dc magnetization appreciably diminish when the samples are re-growth by repeating various grinding-heating cycles (that should maintain the global doping and improve the homogeneity). [34, 35]

Secondly, various theory proposals for the physics of pairing in HTS claim the appearance well above $T_{\rm c}$ of distinct forms of order, different to the superconducting one, and in principle able to produce a DOS reduction at the observed $T_{\rm pgap}$.[10] Prominent examples are the proposals of the formation of charge and spin density waves with d-wave symmetry by Chakravarty, Laughlin and coworkers, [49, 50] of circular orbital charge currents by Varma and coworkers, [51–53] of oscillating charge stripes by, *e.g.*, Kivelson and coworkers [54] (see also [30, 55]), or of localized Bose-condensed pairs screened out by normal carriers as proposed by Geshkenbein and coworkers [56] (these would *not* be *superconducting pairs* because of the screening; see also the related works [57, 58]). Also, various recent experimental works pointed out the possibility of a Fermi surface reconstruction as a function of temperature, mainly for the underdoped compositions. [30, 55] This reconstruction may also produce an effective DOS reduction.

1.4 The importance of the critical temperature superconducting inhomogeneities

It is well stablished that the measurements around any superconducting transition may be deeply affected by the presence of critical temperature inhomogeneities with long characteristic lengths (in particular, larger than the superconducting coherence length amplitude). [34, 35, 99] Usually the effects due to inhomogeneities are larger when closer to the average transition temperature, and thus they could potentially mask, or even mimic, the effects of superconducting critical fluctuations. In fact, and as already briefly commented in the previous subsection, the uncertainties associated to inhomogeneities have acquired a specially central role in different works analyzing previous experiments aiming to determine the $T_{\rm phase}(x)$ and $T_{\rm cond}(x)$ phase diagram of HTS. [23–29, 34–36, 98] This is particularly evident in the case of extensive properties, such as the magnetization, in which the small experimental signals that are associated by some authors to precursive superconductivity have been alternatively explained by other groups by assuming the existence of small (and to be expected) portions of the sample actually being below the transition. [34–36, 98]

For the transport properties, also a detailed analysis of the inhomogeneities is manda-

[10] In fact, those orders may also enhance the temperature and magnetic field responses.

tory. Much of the present thesis report will be devoted to that analysis, including both theoretical aspects and ad-hoc measurements. In fact, our choice of measuring the exponent α in the voltage-current characteristics $V \propto I^{\alpha}$ (that will be our main experimental probe to locate T_{phase}) was motivated by our theoretical findings that the superconducting inhomogeneities almost do not affect the temperature location of the condition $\alpha = 3$, which corresponds to the average $\overline{T}_{\mathrm{phase}}$ in spite of the inhomogeneities. These findings have been obtained by means of finite-element calculations (and also percolation-theory arguments) and we summarize them in chapter 3. The computations presented in chapter 3 also show that the inhomogeneities may be taken into account in the ohmic resistivity above $\overline{T}_{\mathrm{phase}}$ (our main experimental probe to locate $\overline{T}_{\mathrm{cond}}$) by means of relatively simple effective-medium formulae. To apply the latter with as few uncertainty as possible, it is necessary to measure with the best precision the dispersion ΔT_{c} of critical temperatures actually existing in the samples. We obtain this information by performing ad-hoc measurements (high-precision SQUID magnetometry of the Meissner transition, see chapter 2).

USC
UNIVERSIDADE
DE SANTIAGO
DE COMPOSTELA

Chapter 2

Synthesis from separate oxide targets of $La_{2-x}Sr_xCuO_4$ thin films and analysis of their superconducting homogeneity*

* A significant part of the work described in this chapter was performed during two stays at the Laboratoire CRISMAT, ENSICAEN, Université de Caen Basse-Normandie (France), under the direct supervision of Prof. B. Mercey of that Laboratory. This includes both the PLD developments and synthesis procedures, and also preliminary analyses of the samples serving for a first chemical and structural characterization such as some of the profilometry, XRD, SEM and EDX measurements. The rest of the work described in this PhD thesis report was performed at LBTS, Universidade de Santiago de Compostela, Spain.

Summary of the chapter:

We grow a series of superconducting $La_{2-x}Sr_xCuO_4$ thin films with $0.09 \lesssim x \lesssim 0.22$ over (100)$SrTiO_3$ substrates by means of a novel pulsed laser deposition method devised to increase the homogeneity and control of doping. We employ two separate parent oxide targets that receive ablation shots at arbitrary computer-controlled relative rates, instead of the conventional procedure that uses a single target which doping determines the one of the film. We characterize the films both through conventional techniques (XRD, SEM, AFM and EDX) and by measuring their superconducting transition with a high-sensitivity SQUID magnetometer. The latter allows us to determine not only their average macroscopic critical temperatures $\overline{T}_c(x)$ (*i.e.*, the temperature at which macroscopic superconductivity appears) but also their dispersions due to inhomogeneities, $\Delta T_c(x)$. For $\overline{T}_c(x)$ we obtain the conventional parabolic law centered at $x = 0.16$, plus a Gaussian depression near $x = 1/8$ with a $\overline{T}_c$-height of about 5K and x-width about 0.03. For $\Delta T_c(x)$ we obtain, for all the dopings, values among the lowest reported up to now for $La_{2-x}Sr_xCuO_4$. The $\Delta T_c(x)$ dependence can be explained in terms of the unavoidable randomness of the positioning of the Sr ions (the so-called intrinsic chemical inhomogeneity) and a separate residual T_c-inhomogeneity contribution of the order of 0.5 K, this last associated with the samples' structural inhomogeneities and films' substrate.

2.1 Introduction

In order to perform our measurements of the superconducting phase coherence and condensation temperature in HTS, the first necessary step is to obtain samples suitable for the task. As it can be deduced from our introduction in chapter 1 (and as it will become more evident in our analyses of chapter 4) it is crucial that this sample set covers a sufficiently wide range of doping levels, and that each sample present as much homogeneity as possible.

In fact, the obtainment of thin films of perovskite-cuprate HTS with arbitrary amounts of carriers per CuO_2 unit cell (doping level), and with the best possible homogeneity of the superconducting properties, has increasingly attracted the interest of both fundamental and applied research groups.[1] Carrier concentration crucially affects the superconducting characteristics of HTS, including the critical temperature T_c itself, and, consequently, doping inhomogeneity directly induces a dispersion ΔT_c of critical temperatures. [99–105] The study of ΔT_c, and its doping dependence, has received much less attention than T_c by previous researchers. [34, 35, 65, 99–105] Nonetheless, ΔT_c plays a central role for instance when studying the nature of the superconducting fluctuations around the transition. [34, 35, 65, 100, 106, 107]

Among the HTS cuprates, $La_{2-x}Sr_xCuO_4$ (LS_xCO) is regarded as one of the best candidates to attain good control and homogeneity of doping. [64, 66, 67, 91, 108–114] It offers the possibility to change over a wide range the Sr-content index x, that in this compound equals the doping level (always for O-contents saturated at the CuO_4 stoichiometry). [64, 66, 67, 91, 108–114] Importantly, it is chemically quite stable, also with respect to oxygen loss. Regarding the attainable superconducting homogeneity, recent analyses showed that, for LS_xCO in powder form, the homogeneity of the superconducting properties saturate after a number of successive grinding-heating cycles (usually about 10 re-growth repetitions). [34] Together with the analyses of Refs. [34,35,65] these results suggest that the inhomogeneities related to doping have been reduced up to near a minimum, the so-called "intrinsic chemical inhomogeneity" level. [34,35,65] This limit would correspond to a sample synthesized under ideal conditions and perfectly homogeneous precursor oxides, and corresponds to only the unavoidable statistical randomness in the positioning of dopant ions as they grow the non-stoichiometric lattice (for quantitative estimates of the intrinsic superconducting inhomogeneity, see Refs. [34,35,65,115] and also below in section 2.4.3 of this chapter). Lastly, LS_xCO can be grown as a thin film over diverse substrates and with thicknesses ranging from just one unit cell up to hundreds of nanometers. [64, 108–114]

In the remaining of this chapter, we report the growth of LS_xCO thin films over $(100)SrTiO_3$ substrates, by developing a method aimed at increasing the control and homogeneity of doping. We have used pulsed laser deposition (PLD) from two separate parent targets of La and Sr-based oxides that receive laser ablation pulses at arbitrary

[1] For a summary of the influence of T_c-inhomogeneities on the superconducting transition measurements in the HTS see, *e.g.*, Refs. [99–102]. For a view of some of the main implications of obtaining homogeneous HTS from the point o view of applications see, *e.g.*, Refs. [103–105].

and electronically controlled relative rates (instead of using a single LS_xCO target which doping would determine the one of the film). This method was inspired by previous works [116–122] using PLD over separate targets to grow perovskite oxides, and to our knowledge this is the first time that it is applied not only to LS_xCO but also to systematically vary doping in a single-material HTS. Using two parent oxide targets eases the obtainment of arbitrary dopings (no need to synthesize specific HTS powders for each doping) and good final homogeneities (with a single HTS target, the parent inhomogeneities compromise the film too). We obtained superconducting films with dopings $0.09 \lesssim x \lesssim 0.22$, *i.e.*, covering most of the superconducting range and including in particular the underdoped, optimally-doped and overdoped compositions. [64,66,67,91,108–114]

We have characterized our films both by using standard techniques (XRD, SEM, AFM and EDX) and by using high-resolution SQUID magnetometry. The improved sensibility of the latter technique (resolving up to $10^{-11}\mathrm{Am}^2$) allowed us to measure the dispersion ΔT_c, to our knowledge for the first time in any HTS film. The results indicate a superconducting homogeneity similar to the best values attained up to now in LS_xCO bulk samples (either powdered [34, 35, 65, 66] or single-crystals [67]).

The ΔT_c values obtained for each doping are discussed in terms of the intrinsic chemical inhomogeneity estimates. We also include in these calculations an additional x-independent residual T_c-inhomogeneity contribution (due, *e.g.*, to structural factors such as thickness variations, etc.) that becomes relevant only for x-values near the optimal doping, in which $T_c(x)$ is near a maximum and thus the effects of intrinsic chemical inhomogeneities are estimated to become negligible. We show that the $\Delta T_c(x)$ dependence of our films can be satisfactorily explained in terms of the intrinsic chemical disorder and a separate residual T_c-inhomogeneity contribution of ~ 0.5 K. We also show that this result can be extended to the bulk samples of Refs. [33–35, 65–67]

Our sample set also includes films in the vicinity of the $x = 1/8$ singularity. Near it, as expected [66, 92, 93] we find a depression of the $T_c(x)$ values and we propose that this drop could be empirically described as an inverted Gaussian peak spread over about 0.03 units of x.

2.2 Films growth

2.2.1 Targets and substrates

Our PLD technique consists in laser-ablate at custom rates two separate targets, of compositions $La_{1.1}Cu_{0.9}O_{2.4}$ and $SrCuO_2$. These parent oxides were chosen because they are stable and dense enough to allow reproducible deposition rates. The alternate possibilities La_2O_3 and $SrCuO_2$ were discarded because their combination would lack the Cu amount necessary for the $La_{2-x}Sr_xCuO_4$ stoichiometry. In contrast, the combination of the chosen parent oxides produces excess CuO. As our results will evidence, this surplus does not affect the growth of the $La_{2-x}Sr_xCuO_4$ structure. It creates instead separate precipitates, as shown by our SEM studies (see figure 2.7 and section 2.3.2). Also, as

evidenced by our magnetic measurements (see section 2.4), theses precipitates do not affect the superconducting critical temperature $T_c(x)$ of the films neither their transition width $\Delta T_c(x)$, the two central parameters for our present work.

The targets were prepared by solid-state reaction as follows: To synthesize the $La_{1.1}Cu_{0.9}O_{2.4}$ target, carefully weighted amounts of CuO (99.99% purity) and La_2O_3 (99.99% purity) powders were mixed together and ground using a Fritsch-6 ball mill, with 4 cycles of alternate rotations, 4 min each, at 400 rpm. Then, they were heated at a 150 °C/h rate up to 800 °C, maintained at that temperature during 4 h and then cooled, again at 150 °C/h. After this they were manually ground, mixed with an organic binder (rhodoviol) and pressed into a 25 mm diameter disk. Finally, the disk was sintered up to 900 °C during 24 h, with the same heating and cooling rates as before. The result was a disk with diameter decreased by 14% and thickness 5 mm. For the $SrCuO_2$ target, we mixed appropriate quantities of $SrCO_3$ (99.5% purity) and CuO (99.99% purity) and followed with those powders the same procedures as before, except that they were maintained at 800 °C during 24 h and that the disk diameter was 30 mm initially but after sintering it was 9% smaller and again 5 mm thick. All the powders and targets were always kept in a dry atmosphere to minimize humidity absorption. In figures 2.1(a) and 2.1(b) wee show two pictures of the targets.

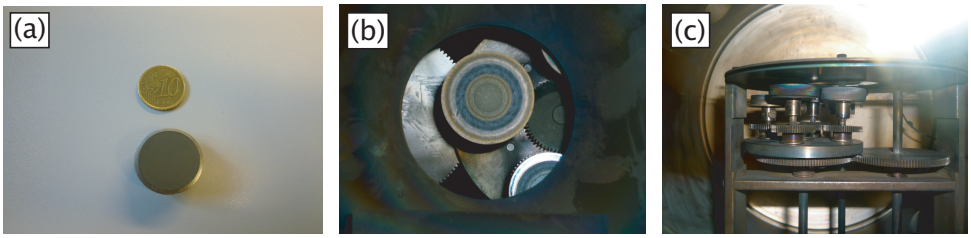

Figure 2.1: Pictures of the targets employed in the synthesis of the $La_{2-x}Sr_xCuO_4$ thin films. (a) $La_{1.1}Cu_{0.9}O_{2.4}$ target just after its sintering. (b) Aspect of the $SrCuO_2$ target after various films were deposited. (c) Upper view of the targets holder.

We used commercial (100)$SrTiO_3$ substrates, due to the compatibility of the lattice parameters with LS_xCO. Before deposition, they were ultrasonically cleaned first with acetone and then with ethanol, in both cases for 5 min. In figure 2.2 are shown two substrates before and after $La_{2-x}Sr_xCuO_4$ deposition.

2.2.2 Deposition setup and parameters

Our PLD chamber setup uses specialized, custom elements for the multi-target holder (see picture (c) in figure 2.1) and the substrate heater. The first is rotatory and motorized so to allow changing what target is in the line-of-sight of the laser and also to continuously

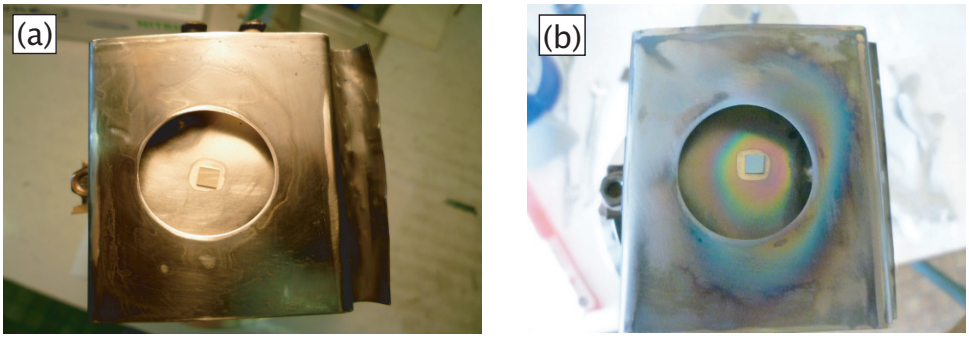

Figure 2.2: The $SrTiO_3$ substrate (a) before and (b) after $La_{2-x}Sr_xCuO_4$ deposition respectively.

spin each target over itself during the laser pulses (to present a fresh surface point to each shot). The substrate heater was developed by Thimont and coworkers [122] and consists on two 150-watt halogen lamps of length 78 mm, placed in parallel to each other inside an aluminum-oxide cavity and covered by an Inconel plate. Directly over this plate are stuck, with silver paste, the substrate and a conventional thermocouple linked to an Eurotherm temperature controller. This heater setup has the advantages of very low cost with respect to the commonly used filament coils, and excellent thermal control and stability. [122]

For the heater temperature and for the oxygen atmosphere pressure in the deposition chamber, we found that the following ramp values are optimal for film growth: Temperature is first raised at 15 °C/min up to 400 °C, then hold steady for 10 min, and raised again at 15 °C/min up to the deposition temperature, which is 700 °C. This temperature is maintained for 100 min during which the film will be grown. Afterwards, the chamber is cooled down to room temperature, at 10 °C/min until 450 °C and at 20 °C/min below that. The pressure ramp is as follows: A 10^{-4} Pa vacuum is first made in the chamber, before heating. When temperature begins to raise, O_2 gas is introduced at 10 Pa. This flow is maintained up to the cooling process, during which the pressure is further increased up to 2.5×10^4 Pa so to anneal the film. In figure 2.3 we show a picture of the PLD chamber used to grown the $La_{2-x}Sr_xCuO_4$ films. Figure 2.4 shows the Electronics that controls the PLD system and the Optics trespassed by the laser beam.

The laser setup and operation parameters are as follows: We used a KrF 248 nm excimer laser (LPX200 Lambda Physik) with a pulse energy of 200 mJ and selectable pulse repetition rate. With the aim of improving the homogeneity of the targets surface, when the heater temperature reaches 700 °C each target is shot during 500 pulses at a frequency of 5 Hz. During this cleaning process a plate protects the substrate from any unwanted deposition. Then the plate is removed, the laser is changed to 3 Hz repetition

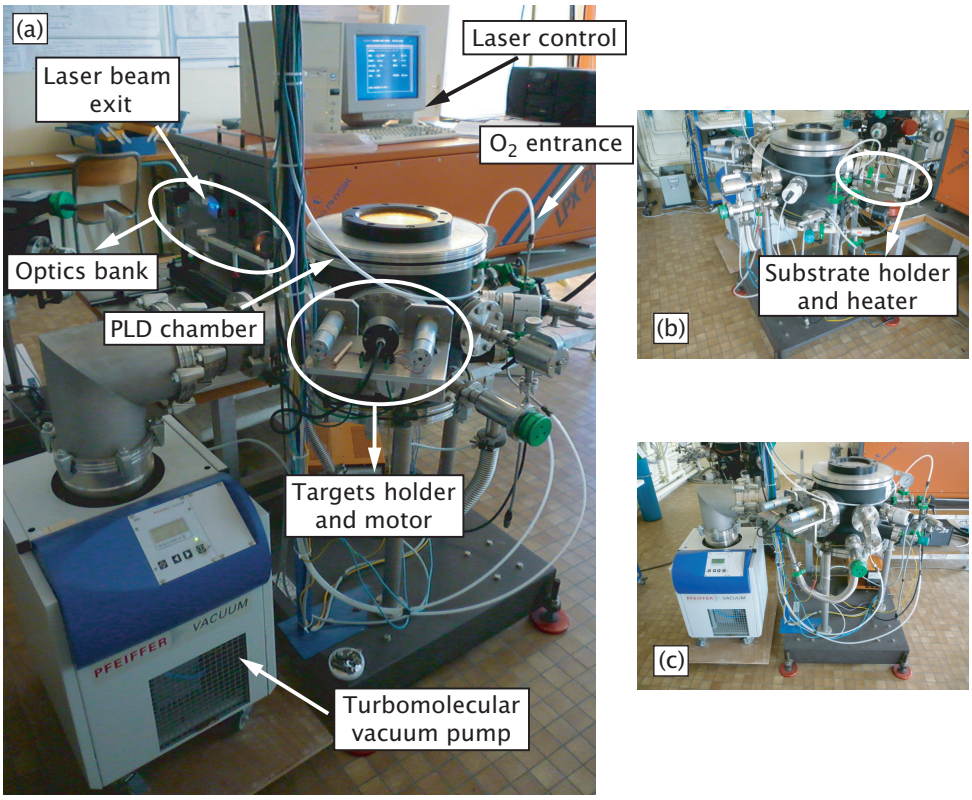

Figure 2.3: Pictures of the PLD chamber and laser setup employed in the fabrication of the $La_{2-x}Sr_xCuO_4$ thin films. (a) Main elements of the PLD deposition system. (b) and (c) show different views of the equipment presented in (a).

frequency, and the deposition laser shot cycles begin. These consist on sending a number N_{LCO} of shots over the $La_{1.1}Cu_{0.9}O_{2.4}$ target, and then a single shot over the $SrCuO_2$ one. The plasmas produced by the laser have short lifetimes and they disappear before the next shot. These cycles are repeated during 100 min. By using a different value of N_{LCO} for each film, the doping x is expected to vary accordingly, as we discuss in detail in the next subsection. In figure 2.5 we show two pictures of the two main steps of the deposition process inside the chamber, *i.e.*, the heating of the substrate and the plasma produced by the laser.

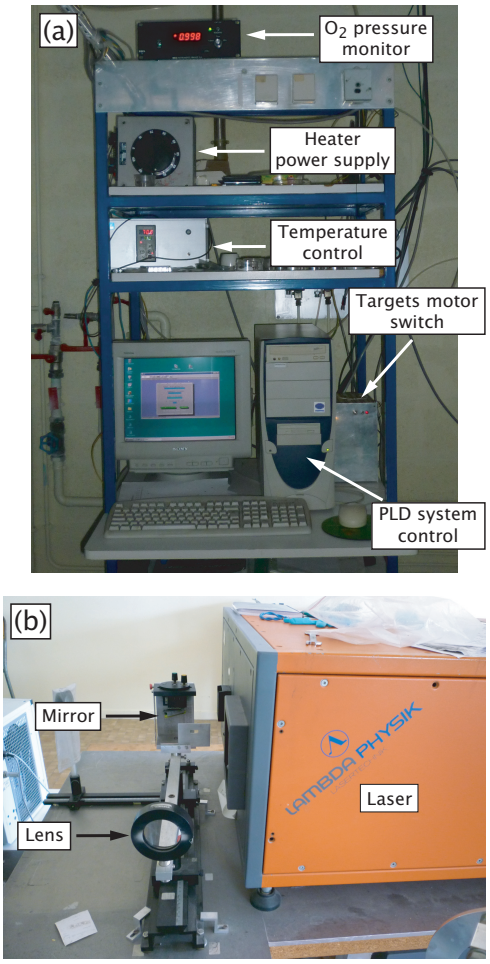

Figure 2.4: (a) and (b) pictures show the PLD system control setup and the Optics respectively.

2.2.3 Nominal doping

We have grown different films, each of them with its own distinct value of N_{LCO} as summarized in table 2.1. In order to associate a nominal doping level x with each of those films, we note first that naturally N_{LCO} shall be proportional to the quotient between the number of La and Sr atoms reaching the substrate. Therefore, we expect the La/Sr atomic ratio finally in the film, $(2-x)/x$, to be also proportional to N_{LCO}. To obtain the proportionality constant, we need to assign a given doping level to one of our samples.

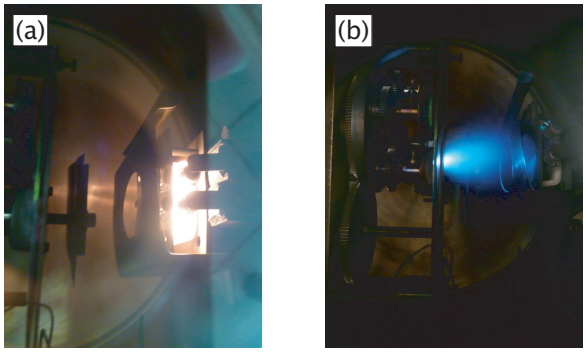

Figure 2.5: Pictures showing the details in the chamber during deposition while (a) the substrate is being heated and (b) while the target is being shot by the laser.

We choose as that reference our film with $N_{\mathrm{LCO}} = 18$, for which we take $x = 0.16$. This value is in agreement with the observation that the superconducting critical temperature of this film is maximal (see section 2.4.2 and figure 2.12), as known to happen in HTS at $x = 0.16$ (the so-called optimal doping). [66, 123, 124] The resulting nominal x values, for all our films, are listed in table 2.1. Importantly, for all the samples these nominal values are in excellent agreement with the determination of x performed in section 2.3.4 using independent EDX techniques to measure the atomic ratios (see table 2.1). The nominal dopings are also consequent with the complete $\overline{T}_{\mathrm{c}}(x)$ phenomenology (the one considering all our samples) presented and discussed in section 2.4.2, including as well the existence of a depression of $\overline{T}_{\mathrm{c}}(x)$ near nominal $x = 1/8$. [66, 92, 93] All of this confirms then the basic adequateness of the nominal dopings listed in table 2.1, through the entire doping range explored in this work.

2.3 Compositional and structural characterization

2.3.1 XRD characterization

In order to check the epitaxy of our films (and in particular that they have grown with the crystallographic c-axis perpendicular to the substrate, *i.e.*, with the superconducting CuO_2 planes parallel to the latter) we have performed X-ray diffraction (XRD) over them. For all our samples, we obtained diffractograms in which the only visible peaks of the perovskite structure are the (00ℓ) ones. This confirms then that the film growth is epitaxial with c-direction orientation. Figure 2.6 shows some representative examples of these diffractograms. The employed equipment was a PANalytical's Empyrean diffractometer, equipped with a 5-axes goniometer and an area detector PIXcel$^{3\mathrm{D}}$. We

sample	N_{LCO}	x (nominal)	x (EDX, ±0.01)	thickness (nm, ±10%)	$\overline{T}_c$ (K)	ΔT_c (K)
$LS_{0.09}CO$	35	0.09	0.09	325	9.9	1.4
$LS_{0.10}CO$	30	0.10	0.10	200	15.0	1.2
$LS_{0.11}CO$	27	0.11	0.11	175	17.0	1.1
$LS_{0.12}CO$	25	0.12	0.12	275	15.4	1.4
$LS_{0.13}CO$	22	0.13	0.13	300	17.7	2.3
$LS_{0.15}CO$	20	0.15	0.14	150	20.8	1.3
$LS_{0.16}CO$	18	0.16	0.16	275	22.0	1.3
$LS_{0.19}CO$	15	0.19	0.20	250	20.0	0.7
$LS_{0.22}CO$	13	0.22	0.22	200	17.6	1.6

Table 2.1: Main parameters of the LS_xCO films studied in this work. As detailed in section 2.2.3, the nominal value of the doping x was calculated by considering the La/Sr atomic ratio to be proportional to N_{LCO} (the number of PLD shots over $La_{1.1}Cu_{0.9}O_{2.4}$ per each shot over $SrCuO_2$) and assigning to the sample here called $LS_{0.16}CO$ a nominal doping of $x = 0.16$. The value of x derived from EDX measurements was extracted from the La/Cu atomic ratio (so to avoid the influence of the Sr in the substrate, see section 2.3.4). The thickness was measured using AFM scans that included photolithographed areas (see section 2.3.2). The average critical temperature $\overline{T}_c$ and its FWHM dispersion ΔT_c were measured using SQUID magnetometry (see figure 2.11 and section 2.4.1).

used radiation with wavelength $\lambda(K_{\alpha 1}) = 1.5406$ Å obtained from a sealed Cu tube and a hybrid 2-bounce Ge(220) monochromator. Measurements were made in the angular region $10^o < 2\theta < 80^o$ with step rate 0.02^o/s.

2.3.2 SEM and AFM characterization of the surface morphology and film thickness

We imaged the surface of our films by using scanning electron microscopy (SEM) and mapped their thickness profile using atomic force microscopy (AFM). Some examples of the results are shown in figures 2.7 and 2.8. Because AFM actually measures height differences, to obtain the absolute thickness we first photolithographed a small microbridge in the film, and we included in the AFM scan paths also the exposed substrate surface.[2] We have tested that further annealing our films has no effect on the film thickness or

[2]We note that our photolithography methods (see section 2.3.3) are expected to etch the $SrTiO_3$ substrate less than about 2 nm in depth, therefore not significantly influencing our measurements of the

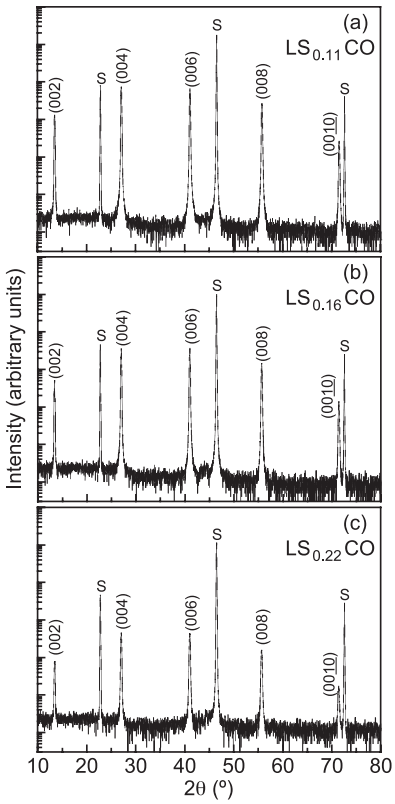

Figure 2.6: XRD patterns for the LS_xCO films with nominal dopings (a) $x = 0.11$, (b) $x = 0.16$ and (c) $x = 0.22$. Peaks marked with S belong to the structure of (100)$SrTiO_3$ substrate.

roughness resulting from these measurements (nor in the rest of the structural or superconducting properties measured in this work). For the SEM images we used a Carl Zeiss' EVO LS microscope tuned to 50 nm resolution. For the AFM profile, we used a Digital Instruments' NanoScope E microscope with the LFM-3/269 measuring module, in contact mode. Our photolithography methods are described in detail in section 2.3.3.

LS_xCO layer thickness, based on comparing by means of AFM the photolithographed areas to the non-photolithographed ones. The 2 nm estimate is based on previous studies about the etching capability of the nitric acid over $SrTiO_3$ substrates [125] which indicate that, even when using solutions of nitric acid with 4.6% concentration, our exposition times (< 4 s) would etch less than 10 nm of the substrate. If we take into account that the nitric acid concentration used by us is about 5 times smaller, the expected $SrTiO_3$ etching depth for our lithographic procedures falls to only about 2 nm. When compared with our results for the LS_xCO film thickness (from 150 up to 325 nm with $\lesssim 10\%$ variations inside each microbridge), substrate etching can be expected to affect quite negligibly our thickness measurements.

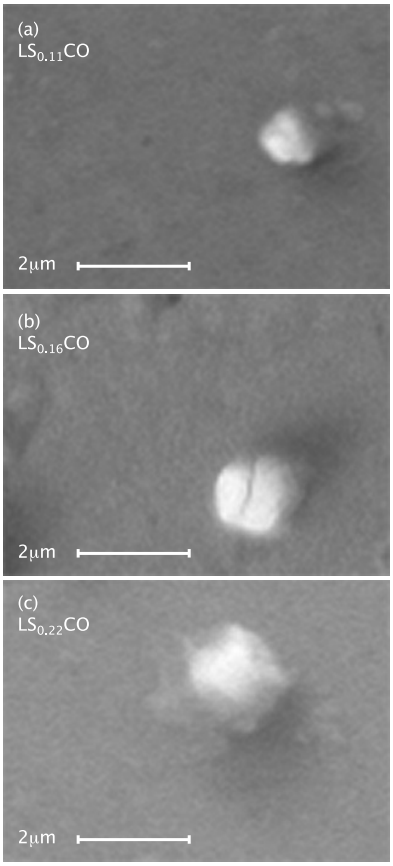

Figure 2.7: Some examples of SEM images for the surfaces of the films with nominal dopings (a) $x = 0.11$, (b) $x = 0.16$ and (c) $x = 0.22$. We have chosen regions showing also some of the isolated precipitates of radius $\lesssim 500$ nm that appear in the films. As discussed in the main text, the precipitates seem to have much enhanced Cu content and they do not significantly affect the superconducting properties measured in this work.

The thicknesses obtained through the AFM measurements, for each of our films, are summarized in table 2.1. They range between about 150 and 325 nm. The thickness variation inside each film is smaller, as it remains always below 10% along different points in the same microbridge.[3] These AFM scans were done along paths that avoid any of the scattered incrustations that the SEM images also reveal in our films (see figure 2.7). These

[3]Note that the $\pm 10\%$ in the figure does not correspond to a standard deviation of the distribution of thickness (that would be significantly smaller). It corresponds instead to a somewhat crude estimate to the peak-to-peak differences.

outgrowths are spheroids with radius below about 500 nm and average separations from each other well larger than those sizes, and they seem similar to the precipitates found by other authors in the SEM images of their LS_xCO films (see, *e.g.*, figure 3 of [108]). Our EDX measurements performed on these particles show that they comprise a much increased concentration of Cu (an example EDX spectrum of the precipitates is provided in the see next section together with our EDX instrumental details). Let us already mention here that according to the magnetic characterizations (see section 2.4) these incrustations do not seem to affect the value nor the homogeneity of the superconducting critical temperature. This is coherent with the fact that their size is well larger than both the in-plane superconducting coherence length amplitude ($\xi_{ab}(0)$, of the order of 3 nm in LS_xCO [35, 112, 113]) and the T_c-domain size of our films (of the order of 30 nm, see section 2.4.3). Note also that these incrustations could improve the superconducting critical current of the films, by serving as vortex pinning centers, because their size competes with the in-plane superconducting magnetic penetration depth amplitude of LS_xCO ($\lambda_{ab}(0)$, of the order of 200 nm [65]). This possibility has not been researched in the present work.

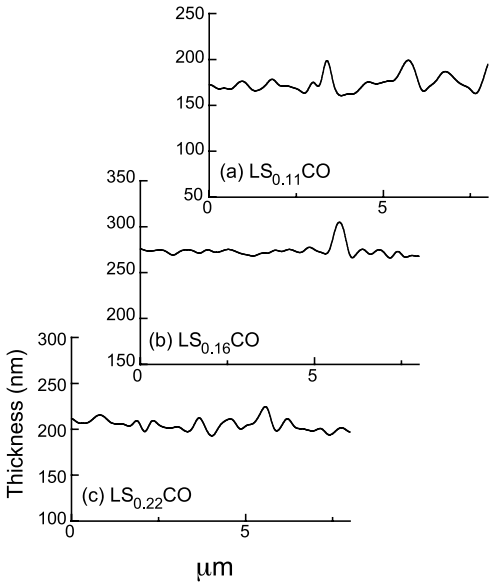

Figure 2.8: Some representative AFM profiles of the LS_xCO films with nominal dopings (a) $x = 0.11$, (b) $x = 0.16$ and (c) $x = 0.22$. Because AFM only measures height differences, to obtain the absolute value of the thickness we extended the AFM scans up to areas where the superconducting film was removed using lithography so to expose the substrate. The portions of the scans shown in the figures correspond to areas well separated from the lithographed edges.

2.3.3 Photolithography procedures

For the photolithography we have followed these steps:

1) Clean the sample with acetone.
2) Pipette about 1.5 ml of photoresist Ar-P3540T (one drop) on top of the film, covering it.
3) Place the film on a spinner and make it rotate at 5890 rpm during 40 s.
4) If the photoresist is homogeneously distributed over the film's surface (*i.e.*, has not lumps), warm it at 95 °C for 60 s. Otherwise, thoroughly clean it with acetone, dry it with compressed air, and go back to step 1.
5) Illuminate the film with ultraviolet light during 30 s, with an acetate mask printed with the desired microbridge geometry placed covering the film so that the light excites only the area to be eroded from the film.
6) Develop the film by stirring it softly during 30-45 s. We use developer AR300-44.
7) Right after the developing process is complete, with no delay introduce the sample on deionized water to fully stop the developer action.
8) Dry the sample again with compressed air, at slow flow, and check with an optical microscope if the desired pattern is well defined. Otherwise, clean the sample again with acetone, and return to step 1.
9) Immerse during less than 4 s the sample in nitric acid, HNO_3, at 1% vol, to wash out the superconductor from the areas attacked by the developer.
10) With no delay after the previous step, introduce the sample on deionized water to stop the acid's action.
11) Finally, after checking at the microscope that the pattern was perfectly photolithographed, eliminate the rest of photoresist in an acetone bath and dry the sample with compressed air.

2.3.4 EDX characterization of the doping level

We applied energy-dispersive X-ray spectroscopy (EDX) to quantify the relative amounts of the different types of atoms in our films, and then obtain a direct measurement of their doping level x. We used the same SEM equipment as before, complemented with an Oxford INCAx-act detector. Some examples of the obtained spectrograms are shown in figure 2.9. In principle, one could be tempted to obtain x by comparing the sizes of the peaks in those spectrograms corresponding to the La and Sr atomic orbital transitions. However, attention must be paid to the fact that our substrate also contains Sr and therefore may affect any doping measurement based on the La/Sr ratio. Therefore, we use instead the La/Cu ratio. In table 2.1 we indicate the corresponding doping level x obtained from that procedure, for each of our films. The experimental uncertainty in this determination of x is of ± 0.01, mainly due to an almost $\pm 1\%$ uncertainty in the

Cu-content determination. As evident in table 2.1, within such uncertainty there is an excellent agreement between these EDX doping results and the nominal dopings that we assigned to each sample in section 2.2.3 using the two-target laser shot ratios.

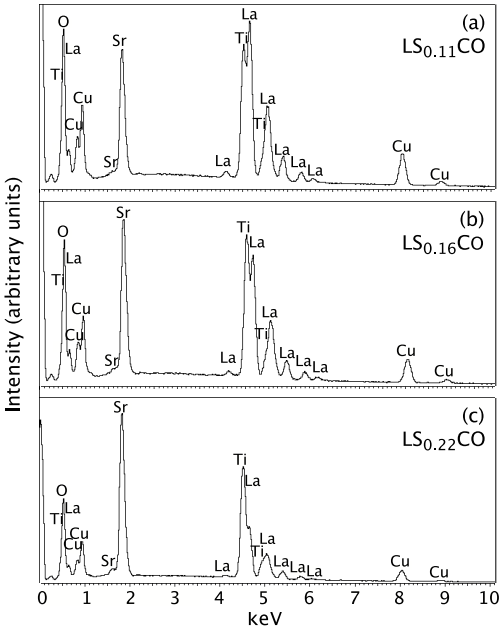

Figure 2.9: EDX spectra for the LS_xCO films with nominal dopings (a) $x = 0.11$, (b) $x = 0.16$ and (c) $x = 0.22$. These results can be used to further check the adequateness of the nominal values, by obtaining x from the relative sizes of the La and Cu peaks (see table 2.1 for the numerical results and also section 2.3.4). The Sr peaks comprise contributions from both the film and the substrate, and hence they were not used to determine x.

As it was already mentioned in section 2.3.2, the SEM images of our films reveal the presence of scattered incrustations on their surfaces. In figure 2.10(a) we show an example of an EDX spectrogram obtained when focusing the X-ray beam on one of those incrustations (spot A in the figure). In figure 2.10(b), we show for comparison an EDX spectrogram obtained in the same film but on a incrustation-free spot (spot B in the figure). The different size of the Cu peaks of each spectrum is evident, being much larger in the incrustation. A quantitative analysis of the peaks indicates Cu concentrations of 4.6 at.% in spot B versus 22.3 at.% in spot A (*i.e.*, about 5 times more Cu in the incrustation). The typical areal number density of outgrows in our films is about 0.05 incrustations/μm^2, and then the average interdistance between neighbouring incrustations is $\sim 5\mu$m. Their typical radius is below about 500 nm.

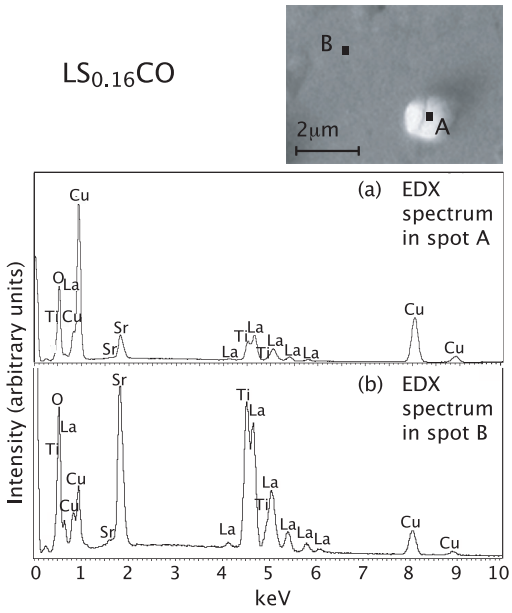

Figure 2.10: EDX spectra at different points of the $LS_{0.16}CO$ film. The spectrum (a) corresponds to focusing the X-ray beam on a spot in one of the film's incrustations (spot A) and the spectrum (b) to focusing it on a incrustation-free spot (spot B).

2.4 Superconducting critical temperature and its homogeneity

2.4.1 Determination of the critical temperature and of its dispersion through high-sensitivity SQUID magnetometry

A direct experimental study of the superconducting critical temperature T_c of a superconductor can be done through the magnetic susceptibility χ, measured with a dc magnetic field applied perpendicular to the in-plane direction and following a zero-field-cooled (ZFC) procedure. In the fully superconducting state such χ equals -1 (we use SI units), *i.e.*, has an amplitude orders of magnitude larger than in the normal state (in which $|\chi| < 10^{-4}$ in most HTS). [10] In addition, and if sufficient resolution is available, the form of the $\chi(T)$ jump in the transition also provides the statistical distribution of the local T_c-values in the sample: Specifically, due to the above difference in orders of magnitude, $-\chi(T)$ around the transition is, in excellent approximation, simply the unitary volume fraction of the sample having critical temperature above T. [10, 34, 35, 65] In other words, the plot of $d\chi/dT$ versus T can also be seen as a plot of the distribution

$\omega(T_c{}')$ of the critical temperatures of the sample, weighted by volume. The sensitivity of traditional SQUID magnetometers is, since many years ago, sufficient to extract by this method the T_c-distribution in polycrystals and even in large single-crystals. However, to the best of our knowledge in thin films this has never been done up to now, probably because their small magnetic moment (associated with their small volume) requires the use of last-generation magnetometers, able to sense magnetic moments as small as about $\sim 10^{-11}\mathrm{Am}^2$. We have applied such method to our films by employing a Quantum Design's MPMS-XL magnetometer, able of said sensitivity using an applied magnetic field of only 0.8 Oe. We subtracted from our measurements the contribution of the substrates, which is measured apart. It is important to note also that the demagnetizing-factor correction, [10] always significant in the superconducting state, in our case appreciably changes the $\mathrm{d}\chi/\mathrm{d}T$ shape around the transition: To further clarify this point, let us write the corrected χ, for fields applied perpendicularly to the surface of the film, as [10, 126]

$$\chi = \frac{\chi_{\mathrm{raw}}}{1 - D_\perp\, \chi_{\mathrm{raw}}}, \tag{2.1}$$

where $\chi_{\mathrm{raw}} = m_{\mathrm{raw}}/(VH)$, m_{raw} is the measured magnetic moment, V the superconductor volume, H the applied magnetic field, and $D_\perp$ the demagnetizing factor for perpendicular fields. For thin films, $D_\perp \simeq -1$. [10] As expected, the effect of correction (2.1) markedly increases as $|\chi_{\mathrm{raw}}|$ grows through the transition: In the normal state it is negligible, when $\chi = -0.5$ it already accounts for a 50% correction, and when $\chi = -0.75$ for a 75% correction. Consequently, all of the experimental χ reported in this chapter correspond to measurements from which both substrate contributions and demagnetizing effects have already been corrected.[4]

The insets in figure 2.11 show our experimental results for the $\chi(T)$ near the superconducting transition in all our films. The main panels of this figure show the corresponding experimental $\mathrm{d}\chi(T)/\mathrm{d}T$ versus T curves. They also show fits to $\mathrm{d}\chi(T)/\mathrm{d}T$ using a Gaussian-peak functionality, the one that may be expected for a random spatial distribution of T_c-values (see [34, 35, 65, 99, 127], or also section 2.4.3):

$$\frac{\mathrm{d}\chi}{\mathrm{d}T} = \omega(T_c{}') = \frac{2\sqrt{\ln 2}}{\sqrt{\pi}\Delta T_c}\, \exp\left[-\left(\frac{T_c{}' - \overline{T}_c}{\Delta T_c/(2\sqrt{\ln 2})}\right)^2\right]. \tag{2.2}$$

Here $\overline{T}_c$ is the average critical temperature and ΔT_c is the full-width at half-maximum (FWHM) of the distribution. The fits using equation (2.2) presented in figure 2.11 take $\overline{T}_c$ and ΔT_c as free parameters for each doping. The fitting region is always $\mathrm{d}\chi/\mathrm{d}T > 0.1$

[4] We do our magnetic measurements with the surface of the film perpendicular to the applied magnetic field. Measuring and analyzing the response to external fields applied parallel to the surface (parallel response) would be problematic due to the fact that, even for very small angles θ between the surface and the applied field, the response to the small perpendicular field component would easily outweigh the parallel response. This oversensitivity to θ is also due to demagnetizing effects: In the parallel orientation and for such thin samples, [10,126] the internal parallel magnetic field would be $H\cos\theta/(1-D_\parallel)$, with a demagnetizing factor $D_\parallel \ll 1$, while the internal perpendicular magnetic field would be $H\sin\theta/(1-D_\perp)$, with $D_\perp \simeq 1$. [10, 126] Therefore, the perpendicular component of the magnetization could be larger than the parallel one even for very small θ values. For this reason, we have chosen to measure and analyze the perpendicular magnetic response.

(comprehending about 80% of the T_c-distribution).[5] As visible in these plots, the quality of the fit is very good for all the films. The values resulting for $\overline{T}_c(x)$ and $\Delta T_c(x)$ are given in these plots (they are also summarized in figures 2.12 and 2.13 and in table 2.1). We checked that variations of the fitting region of the peak would produce changes in the ΔT_c values of up to about $\lesssim 0.2$ K, which then may be taken as a crude estimate of the uncertainty of our ΔT_c results.

Our $\overline{T}_c$ values are similar to those that may be obtained by using a comparable T_c definition (*i.e.*, locating T_c near the midpoint of the transition) from the resistivity measurements made by other authors in LS_xCO films with similar substrate, thickness and average dopings. [108, 110] For an account of the thickness dependence of T_c determined using such a type of criterion see, *e.g.*, figure 4 of Ref. [110].

2.4.2 Dependence on doping of the average macroscopic critical temperature, $\overline{T}_c(x)$

In figure 2.12 we show the values of $\overline{T}_c$ obtained in the previous subsection, represented as a function of the nominal doping x. The vertical dispersion bars in the data points correspond to $\pm\Delta T_c$. The dashed line in this figure is the popular empirical relation $\overline{T}_c = T_c^{opt}[1 - ((x - 0.16)/0.11)^2]$ that is well known to generally apply to any HTS compound. [123, 124] In this formula, T_c^{opt} is the critical temperature for the optimal doping $x = 0.16$. To plot the dashed line of figure 2.12, for T_c^{opt} we have used just the value of $\overline{T}_c$ measured for sample $LS_{0.16}CO$ (22.0K). Therefore, no free parameters were used. As evident in the figure, excellent agreement is obtained except for the data near $x = 1/8 = 0.125$. This composition, often called "magical-number doping", [92, 93] is known to correspond in HTS to a doping level in which the T_c values are depressed with respect to the parabolic trend. [66, 92, 93] The deepness of the depression, and its range of influence over nearby dopings, seem to be nonuniversal across different HTS compounds. [66, 92, 93] For our films, we propose that the following empirical formula could be used to reproduce our $\overline{T}_c(x)$ data set:

$$\overline{T}_c(x) = T_c^{opt}\left[1 - \left(\frac{x - 0.16}{0.11}\right)^2\right] - \delta T_{c1/8}\,\exp\left[-\left(\frac{x - 1/8}{\delta x_{1/8}}\right)^2\right]. \qquad (2.3)$$

[5] It could be asked whether, in addition to T_c-inhomogeneities, also superconducting fluctuations could contribute to the rounding of the transition of the magnetic susceptibility. [9, 34, 35, 65, 99, 128, 129] However, this will only happen at the measurable level in the upper temperatures of the smeared transition, where the superconducting fluctuation contributions to the magnetic susceptibility, χ_{fl}, can still compete with the total magnetic susceptibility, χ. [9, 34, 71, 99, 130, 131] Our analyses for $\overline{T}_c$ and ΔT_c focus instead in a region where $|\chi|$ is already orders of magnitude larger than $|\chi_{fl}|$: In particular, $|\chi_{fl}|$ above the transition is of the order of $\lesssim 10^{-4}$ (in SI units; see, *e.g.*, figure 6 of Ref. [128]) while we have used for our analysis the region $d\chi/dT > 0.1$, in which it is roughly $|\chi| \gtrsim 5 \times 10^{-2}$. Therefore, our present analyses for $\overline{T}_c$ and ΔT_c can be expected to hold independently of the study of the superconducting fluctuations further above $\overline{T}_c$. A more detailed take on these differences between fluctuation roundings and inhomogeneity roundings of the magnetic susceptibility has been given in Ref. [34]. For instance, figure 8 of that paper illustrates how in LS_xCO the inhomogeneity roundings of the magnetic susceptibility are in general well larger than the fluctuation roundings except for T well above $T_c + 2\Delta T_c$.

This corresponds to a Gaussian-peak influence of the $x = 1/8$ depression over nearby dopings, with $\delta T_{c1/8}$ corresponding to the T_c-drop at $x = 1/8$ and $\delta x_{1/8}$ determining the typical x-size of its influence range. The continuous line in figure 2.12 is the fit of this equation (2.3) to our $\overline{T}_c(x)$ data, using the same $T_c^{opt} = 22.0$K as before and with $\delta T_{c1/8}$ and $\delta x_{1/8}$ as free parameters. We get $\delta T_{c1/8} = 4.8$K and $\delta x_{1/8} = 0.01$. As visible in figure 2.12, the agreement is now excellent in the full doping-range explored. It is also visible that the inverted peak correction has a total x-size of about 0.03 doping units.

2.4.3 Dependence on doping of the dispersion of the critical temperature, $\Delta T_c(x)$

In figure 2.13 we show the transition widths ΔT_c obtained for each of our films, normalized by their respective average critical temperatures $\overline{T}_c$, as a function of the doping x. We also include data from previous works [34, 66, 67] reporting some of the narrowest transitions obtained in the LS_xCO family using a magnetic susceptibility analysis comparable to ours. They correspond to bulk samples, either polycrystalline [34, 66] or single-crystals [67], and therefore have well larger T_c-values than films (because of the substrate strain [108, 110]). As this figure evidences, even when normalized by $\overline{T}_c$ our samples have ΔT_c values among the lowest reported up to now for LS_xCO. The figure also shows that $\Delta T_c/\overline{T}_c$ roughly follows an upward concave parabolic dependence on x, except near the $x = 1/8$ anomaly. The remaining of this section will be devoted to show that these experimental results can be accounted for in terms of the intrinsic chemical inhomogeneity associated with the randomness of the positioning of the Sr ions, and a separate residual T_c-inhomogeneity contribution of the order of 0.5 K (associated, *e.g.*, with the samples structural inhomogeneities and films substrate).

As already mentioned in the Introduction of this chapter, LS_xCO is non-stoichiometric and therefore its doping level may vary over space. As emphasized in Refs. [34, 35, 65], even when the causes of inhomogeneity related to synthesis conditions are minimized, at least one will unavoidably remain: As unit cells grow, each (La,Sr)O pair will be formed with either a La or a Sr atom with random probabilities of, respectively, $1-\overline{x}/2$ and $\overline{x}/2$, where $\overline{x}$ is the average doping level. Therefore, at the atomic level Sr does not substitute La following a regular space pattern but a random one. Note that each Sr contributes to the closest superconducting CuO_2 plane with one excess carrier, delocalized over a region which in principle may be anisotropic and span over several CuO_2 unit cells. [115] This unavoidable (La,Sr) randomness induces a so-called "intrinsic chemical inhomogeneity" of the doping of the CuO_2 planes. [34, 35, 65, 115] Due to the $T_c(x)$ dependence, this translates into a T_c-dispersion that will naturally depend both on $\overline{x}$ and on the number of (La,Sr)O pairs over which the doping in a T_c-domain is effectively averaged. It is relatively easy to perform such coarse-grained averages to explicitly estimate this inhomogeneity level. In particular, the probability $\omega(x')$ that a given T_c-domain extending over a number N' of (La,Sr)O pairs presents doping x' (*i.e.*, has $x'N'/2$ atoms of Sr) is proportional to the number of compatible (La,Sr)O configurations in the domain, times

the number of compatible configurations in the remaining of the superconductor: [34]

$$\omega(x') \propto \binom{N'}{N'\,x'/2}\binom{N_{\rm tot}-N'}{N_{\rm tot}\,\overline{x}/2-N'\,x'/2}, \tag{2.4}$$

where $N_{\rm tot}$ is the total number of (La,Sr)O pairs in the sample. Let us take the proportionality constant in equation (2.4) as $N'/\left[2\binom{N_{\rm tot}}{N_{\rm tot}\overline{x}/2}\right]$, so to allow for continuous values of x' and to normalize the distribution as $\int_0^2 \omega(x')\mathrm{d}x' = 1$. Also, for films comprising a large number of in-plane unit cells ($N_{\rm tot} \gg N'$) it is possible to write

$$\lim_{N_{\rm tot}\to\infty} \frac{\binom{N_{\rm tot}-N'}{N_{\rm tot}\,\overline{x}/2-N'\,x'/2}}{\binom{N_{\rm tot}}{N_{\rm tot}\,\overline{x}/2}} = \left(1-\frac{\overline{x}}{2}\right)^{N'\left(1-\frac{x'}{2}\right)}\left(\frac{\overline{x}}{2}\right)^{N'\frac{x'}{2}}. \tag{2.5}$$

In this equation, we used that $\overline{x}$ and x' are bound between 0 and 2. Using equation (2.5), $\omega(x')$ just takes the form of a binomial distribution over the variable $x'N'/2$.[6] As is well known, the binomial distributions can be approximated as normal ones for sufficiently large power exponents, which in our case translates to the conditions $N'\overline{x}/2, N'(1-\overline{x}/2) > 5$, that are fully realistic for the relevant doping range $0.09 \lesssim \overline{x} \lesssim 0.22$.[7] We obtain then:

$$\omega(x') \simeq \frac{2\sqrt{\ln 2}}{\sqrt{\pi}\Delta x^{\rm intr}} \exp\left[-\left(\frac{x'-\overline{x}}{\Delta x^{\rm intr}/(2\sqrt{\ln 2})}\right)^2\right], \tag{2.6}$$

with a FWHM of the distribution, $\Delta x^{\rm intr}$, given by

$$\Delta x^{\rm intr} = \frac{2d_{\rm Cu}}{r'}\sqrt{\frac{2\ln 2}{\pi}\left(1-\frac{\overline{x}}{2}\right)\overline{x}}. \tag{2.7}$$

The $\omega(x')$ distribution given by equation (2.6) can be converted to the $\omega(T_{\rm c}')$ distribution of equation (2.2) by simply introducing the $T_{\rm c}(x')$-dependence, for which we use equation (2.3). Note that equation (2.6) was normalized as $\int_{-\infty}^{\infty}\omega(x')\mathrm{d}x' = 1$, and equation (2.2) as $\int_{-\infty}^{\infty}\omega(T_{\rm c}')\mathrm{d}T_{\rm c}' = 1$. Note also that in principle it is tempting to approximate the FWHM of the $T_{\rm c}$-distribution by $\Delta T_{\rm c}^{\rm intr} \simeq |\partial T_{\rm c}/\partial x|\,\Delta x^{\rm intr}$. However, with our equation (2.3) this would inappropriately result in $\Delta T_{\rm c}^{\rm intr} \simeq 0$ at both $\overline{x} = 0.16$ and $\overline{x} = 1/8$. We use therefore the somewhat more adequate

$$\Delta T_{\rm c}^{\rm intr} = 2\max\left|\overline{T}_{\rm c}(x') - \overline{T}_{\rm c}(\overline{x})\right| \;\text{ for } |x'-\overline{x}| \le \Delta x^{\rm intr}/2. \tag{2.8}$$

In equation (2.7), we have introduced an effective in-plane radius of the $T_{\rm c}$-domains defined by the relation $N' = 2\pi(r'/d_{\rm Cu})^2$ ($d_{\rm Cu}$ is the in-plane distance between first

[6] In fact, this corresponds, as it could be expected, to the probability of filling with Sr atoms $x'N'/2$ positions out of a total of N' ones, if each position has Sr-filling probability $\overline{x}/2$ independently of the rest.

[7] In particular, these inequalities hold, when $0.09 \lesssim \overline{x} \lesssim 0.22$, for any $N' \gtrsim 150$; the value of N' resulting from our comparisons with the data will be about 4×10^4, see main text.

neighbour Cu-atoms, for which we take $d_{\mathrm{Cu}} = 3.7$Å). This definition corresponds to T_c-domains that have been approximated as circular and involving a single CuO_2 layer (to which it corresponds two (La,Sr)O layers in LS_xCO). This r' is similar to the quantity L introduced in [34].[8]

Note also that for the $\overline{x}$-values at which $\partial\overline{T}_{\mathrm{c}}(\overline{x})/\partial\overline{x} \simeq 0$, like for optimal doping, the above equation (2.8) will lead to very small $\Delta T_{\mathrm{c}}^{\mathrm{intr}}$ values. In that case, any other remaining source of T_{c}-inhomogeneity may be expected to dominate over the intrinsic chemical one (for instance, structural inhomogeneities such as substrate strain variations, etc.). To take this effect into account in our calculations, we consider an additional residual source of T_{c}-inhomogeneity. We associate with it a second Gaussian distribution of FWHM $\Delta T_{\mathrm{c}}^{\mathrm{res}}$, that we approximate as x-independent. To calculate the global T_{c}-distribution that results when two sources of inhomogeneities coexist (each of them separately producing a normal distribution of T_{c}-values), the two normal distributions have to be accumulated, as (see figure 2.14 for a graphical construction):

$$\omega(T_c') = \frac{4\ln 2}{\pi \Delta T_{\mathrm{c}}^{\mathrm{intr}} \Delta T_{\mathrm{c}}^{\mathrm{res}}} \int \mathrm{d}T_{\mathrm{c}}'' \exp\left[-\left(\frac{T_{\mathrm{c}}'' - \overline{T}_{\mathrm{c}}}{\Delta T_{\mathrm{c}}^{\mathrm{intr}}/(2\sqrt{\ln 2})}\right)^2\right] \times \exp\left[-\left(\frac{T_{\mathrm{c}}' - T_{\mathrm{c}}''}{\Delta T_{\mathrm{c}}^{\mathrm{res}}/(2\sqrt{\ln 2})}\right)^2\right], \tag{2.9}$$

This equation is normalized as $\int \omega(T_{\mathrm{c}}')\mathrm{d}T_{\mathrm{c}}' = 1$ with the limits of both the T_{c}' and the T_{c}'' integrations being $\pm\infty$. After performing the T_{c}'' integration it is obtained:

$$\omega(T_{\mathrm{c}}') = \frac{2\sqrt{\ln 2}}{\sqrt{\pi}\sqrt{(\Delta T_{\mathrm{c}}^{\mathrm{intr}})^2 + (\Delta T_{\mathrm{c}}^{\mathrm{res}})^2}} \times \exp\left[-\left(\frac{2\sqrt{\ln 2}\ (T_{\mathrm{c}}' - \overline{T}_{\mathrm{c}})}{\sqrt{(\Delta T_{\mathrm{c}}^{\mathrm{intr}})^2 + (\Delta T_{\mathrm{c}}^{\mathrm{res}})^2}}\right)^2\right], \tag{2.10}$$

i.e., the global distribution is again Gaussian and the accumulated FWHM dispersion is:

$$\Delta T_{\mathrm{c}}^{\mathrm{intr+res}} = \sqrt{\left(\Delta T_{\mathrm{c}}^{\mathrm{intr}}\right)^2 + \left(\Delta T_{\mathrm{c}}^{\mathrm{res}}\right)^2}. \tag{2.11}$$

An important consequence is that the wider distribution dominates the global result, even more strongly that what would be expected from a linear sum of $\Delta T_{\mathrm{c}}^{\mathrm{intr}}$ and $\Delta T_{\mathrm{c}}^{\mathrm{res}}$: For instance, with $\Delta T_{\mathrm{c}}^{\mathrm{res}} = 0.5$K and $\Delta T_{\mathrm{c}}^{\mathrm{intr}} = 0.04, 0.8$ and 1.1K, we get respectively $\Delta T_{\mathrm{c}}^{\mathrm{intr+res}} = 0.5, 0.9$ and 1.2 (while $\Delta T_{\mathrm{c}}^{\mathrm{intr}} + \Delta T_{\mathrm{c}}^{\mathrm{res}} = 0.5, 1.3$ and 1.6K). In the context of this work, these $\Delta T_{\mathrm{c}}^{\mathrm{intr}}$ and $\Delta T_{\mathrm{c}}^{\mathrm{res}}$ values are the ones corresponding to our samples with respectively $x = 0.16, 0.19$ and 0.10. Note that, as expected, the residual contribution will mainly affect the dopings near the optimal value, being quite irrelevant far from it.

[8] Note however that equations (2.4), (2.7) and (2.8) actually do not assume any shape for the T_{c}-domains and this r' is introduced here only as a reexpression of N' useful to compare with other works. We could also express N' as an effective radius of spherical T_{c}-domains, as $r'_{\mathrm{spherical}} = [3N's d_{\mathrm{Cu}}^2/(8\pi)]^{1/3}$, where $s = 6.6$Å is the distance between adjacent CuO_2 layers. However, due to the large anisotropy of LS_xCO, the planar shape estimate for the radius of the T_{c}-inhomogeneities is probably more accurate than the perfectly spherical one.

As we show in figure 2.13, the application of the above equations for $\Delta T_c^{intr+res}$ reproduces fairly well the transition widths experimentally found in this work. This is achieved by using for all the samples $r'/d_{Cu} = 82$ (equivalent to $N' = 4.2 \times 10^4$) and $\Delta T_c^{res} = 0.5$ K. This r'/d_{Cu} is very close to the value 75 found in [34] for LS_xCO powders. It is also similar to the typical decay length of the charge density correlations as inferred in LS_xCO by Mihailovic [132] directly from optical property measurements ($r'/d_{Cu} \sim 50$ for $0.1 \lesssim x \lesssim 0.2$). The dispersions Δx^{intr} resulting from $r'/d_{Cu} = 82$ are comparable to the uncertainty found in our EDX determinations of the doping (of about ± 0.01). Although in principle considering a x-dependent ΔT_c^{res} could possibly improve the obtained agreement, the average difference between our simple $\Delta T_c^{intr+res}$ estimates and the measured ΔT_c in our films is already below 0.3 K. As can be seen in figure 2.13, the data from [34, 66, 67] in bulk samples are also in quite good agreement with the $\Delta T_c/\overline{T}_c$ calculated here.

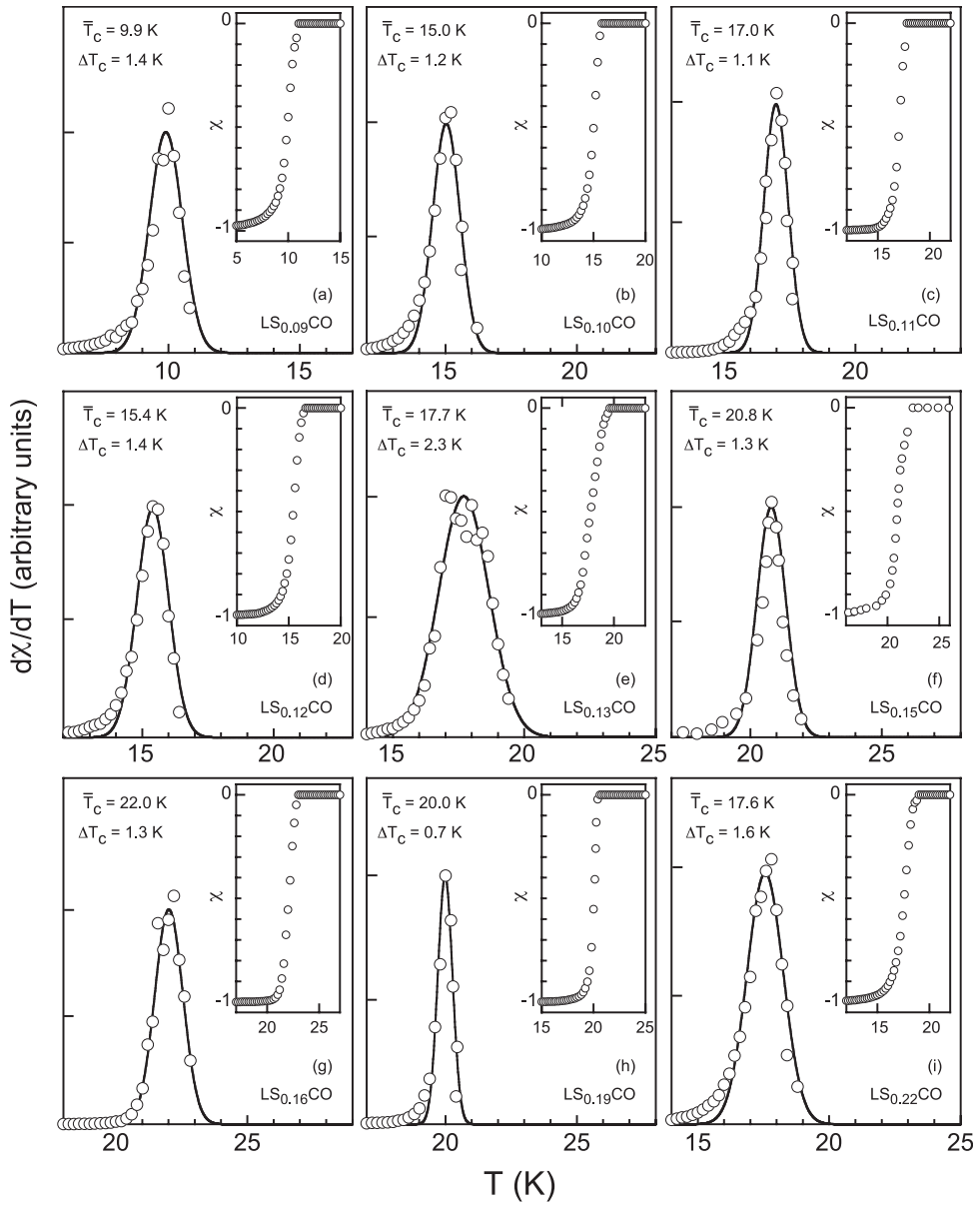

Figure 2.11: Zero-Field-Cooled (ZFC) susceptibility (in the insets) and their T-derivatives (main panels) measured around the superconducting transition using SQUID magnetometry. Figures (a) to (f) correspond to underdoped films, (g) corresponds to optimal doping, and (h) to (i) to overdoped films. We also show fits using equation (2.2), that represents a normal distribution of T_c values. The maximum of the corresponding $d\chi/dT$ peak corresponds to the average critical temperature $\overline{T}_c$, and ΔT_c is the FWHM of the distribution (see also table 2.1 and figure 2.12). The fitting region was $d\chi/dT > 0.1$ (covering about 80% of the distribution).

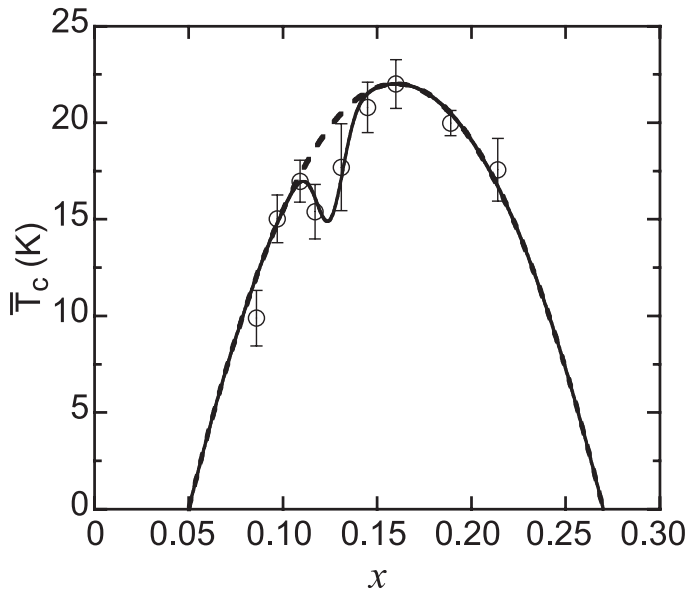

Figure 2.12: Average critical temperature $\overline{T}_c$ of our samples, represented versus the nominal doping x. The $\overline{T}_c$ values were extracted from the susceptibility data near the superconducting transition as shown in figure 2.11. The error bars correspond to $\pm\Delta T_c$. The dashed line is the parabolic law $\overline{T}_c = T_c^{x=0.16}[1-((x-0.16)/0.11)^2]$. The solid line is the fit using equation (2.3), able to also account for the $\overline{T}_c$ depression around $x = 1/8$.

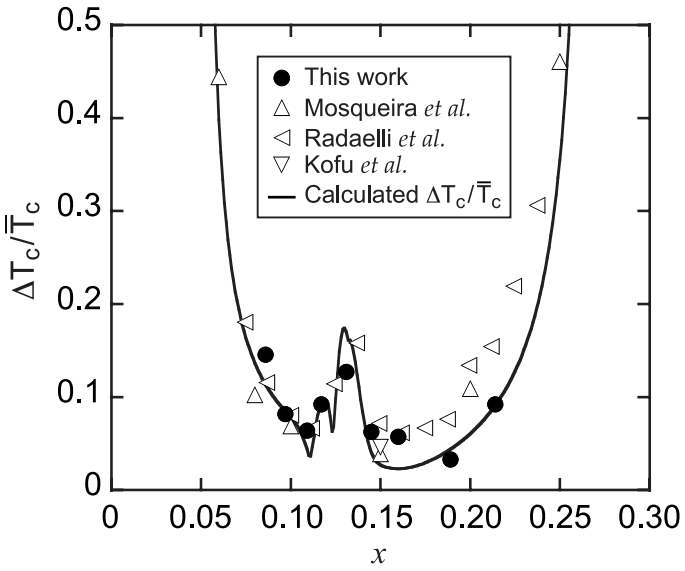

Figure 2.13: Critical temperature dispersion $\Delta T_{\rm c}$ normalized by the average critical temperature $\overline{T}_{\rm c}$, as a function of the doping x in LS_xCO. The closed circles correspond to the films studied in this work (using the nominal values for x). The open triangles correspond to samples from other works [34, 66, 67] (*i.e.*, they correspond to Mosqueira *et al.*, Radaelli *et al.* and Kofu *et al.* data respectively) reporting some of the narrowest transitions obtained in the LS_xCO family using a magnetic susceptibility analysis comparable to ours (they correspond to bulk samples, either polycrystalline [34, 66] or single-crystals [67]). The solid line corresponds to the result of applying equations (2.3) and (2.11) for $T_{\rm c}$ and $\Delta T_{\rm c}^{\rm intr+res}$ respectively (using $r'/d_{\rm Cu} = 82$, $\Delta T_{\rm c}^{\rm res}$=0.5K and also the relationships given by equations (2.8) and (2.7), see main text for details).

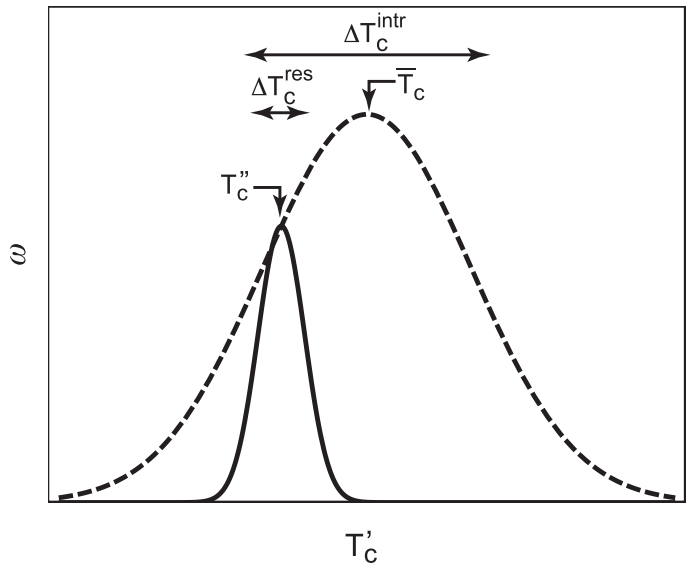

Figure 2.14: Graphical explanation for the construction of equation (2.9). The dashed line is a normal distribution of average $\overline{T}_c$ and FWHM $\Delta T_c^{\rm intr}$. To each critical temperature T_c'' (an example is plotted in the figure) it is associated a second normal distribution (continuous line) centered at T_c'', of width $\Delta T_c^{\rm res}$ and of height equal to the value of the first distribution at T_c''. Finally, the amount of the superconductor with a given critical temperature T_c' is obtained from the value of the second distribution in that T_c', integrated over all possible values of T_c''. Equation (2.9) expresses such integration, with a normalization prefactor so that $\int \omega(T_c')\mathrm{d}T_c' = 1$.

2.5 Conclusions

We have proposed a method to grow HTS films with different doping levels, consisting in PLD of two separate parent oxide targets that receive ablation shots at arbitrary computer-controlled relative rates, instead of the conventional procedure that uses a single target which doping determines the one of the film. We applied this method to grow a series of superconducting $La_{2-x}Sr_xCuO_4$ thin films, with $0.09 \lesssim x \lesssim 0.22$, over (100)$SrTiO_3$ substrates. The method is inspired in previous works [116–122] which used PLD with multiple targets to grow perovskite oxides and multilattices, and to our knowledge this is the first time that this type of procedure is applied not only to $La_{2-x}Sr_xCuO_4$ but also to systematically vary doping in any single-material HTS. We have also shown, by using high-precision SQUID magnetometry, that the method produces films with an homogeneity of the superconducting temperature similar to the best reported up to now in $La_{2-x}Sr_xCuO_4$ bulks. We have also shown that the obtained critical temperature dispersions, ΔT_c, and their x-dependence, can be explained in terms of the unavoidable randomness of the positioning of the Sr ions (the so-called intrinsic chemical inhomogeneity) and a separate residual T_c-inhomogeneity contribution of the order of 0.5 K, this last associated with the samples structural inhomogeneities and films substrate. This chemical disorder is compatible with T_c domains of effective in-plane radius ~ 80 CuO_2 unit cells.

USC
UNIVERSIDADE
DE SANTIAGO
DE COMPOSTELA

Chapter 3

Effects of critical temperature inhomogeneities on the voltage-current characteristics of a planar superconductor near the Berezinskii-Kosterlitz-Thouless transition

Summary of the chapter:

We analyze numerically how the voltage-current ($V-I$) characteristics near the so-called Berezinskii-Kosterlitz-Thouless (BKT) transition of type-II 2D superconductors are affected by a Gaussian distribution of critical temperature inhomogeneities, randomly located in space. We first apply finite-element mesh-circuit simulations that allow to quantify the broadening around the average BKT transition temperature $\overline{T}_{\rm phase}$ of both the exponent α in the relation $V \propto I^{\alpha}$ and of the resistance V/I. These calculations reveal that strong spatial redistributions of the local current will occur around the transition as either the intensity I or the temperature T are varied. They also permit to obtain the corresponding spatial maps of local voltages and currents. Our results reveal that, even in these inhomogeneous superconductors, the condition $\alpha = 3$ provides a good estimate for the location of the average BKT transition temperature $\overline{T}_{\rm phase}$. In addition, we also present a calculation using an effective-medium approach, aimed to obtain the resistance V/I without the need of computing any finite-element simulation. It leads to results in agreement with the finite-element approach except in the close vicinity of $\overline{T}_{\rm phase}$. For instance, for the upper part of the transition both theoretical approaches coincide in all the ohmic region of temperatures, the average mean-field critical temperature $\overline{T}_{\rm cond}$ included.

3.1 Introduction

As first suggested by Berezinskii [44] and by Kosterlitz and Thouless [45] (BKT) for superfluids, and later for superconductors by various authors (see, *e.g.*, [43, 46, 47]), and as already commented in our chapter 1, one of the main features to be expected in the normal-superconducting transition of a two-dimensional (2D) and homogeneous type-II superconductor is the appearance at zero applied magnetic field of two critical temperatures: Namely, the transition is split into *i)* the mean-field critical temperature, also known as superconducting wave function condensation temperature, $T_{\rm cond}$, where it first becomes favourable (in terms of free-energy optimization) to form Cooper pairs and vortices; and *ii)* the BKT critical temperature, or superconducting wave function phase coherence temperature, $T_{\rm phase} < T_{\rm cond}$, where it first becomes favourable that vortices of opposite fluxoid quantization bind into pairs (vortex-antivortex pairs). Among the experimental features revealing this splitting of the transition, probably the most significant is the appearance of a strongly non-ohmic behaviour in the voltage-current $V - I$ characteristics below $T_{\rm phase}$, with the exponent α in the relation $V \propto I^{\alpha}$ jumping at $T_{\rm phase}$ itself to the value $\alpha = 3$. [43] This feature has been, in fact, commonly used to experimentally demonstrate the existence of a BKT transition, both in low-$T_{\rm c}$ 2D structures (see, *e.g.*, [37–42]) and in high-$T_{\rm c}$ superconducting cuprates (HTS) (see, *e.g.*, [59–63, 133]). We note that in the case of the HTS materials even bulk samples are expected to undergo a BKT transition, due to the anisotropic 2D-like layered structure of these superconductors. In fact, in HTS with optimal doping the measurements suggest that the difference $T_{\rm cond} - T_{\rm phase}$, henceforth noted as $\Delta_{\rm BKT}$, may be rather large, of about 2K or more. [59–63, 133]

The $V - I$ measurements also indicate that in real samples the jump of $\alpha(T)$ around $T_{\rm phase}$ is not as abrupt as first predicted by Halperin and Nelson (HN) [43] and later by other authors (see, *e.g.*, [37, 38, 40–42, 59, 60, 63, 133]). This is an important aspect which origin is still debated at present because, in spite of the fact that most real samples are expected to have some degree of inhomogeneities of the values of $T_{\rm cond}$ (and of $T_{\rm phase}$), almost no calculations have been done on how a spatially-random distribution of $T_{\rm cond}$-values will affect the BKT non-ohmic characteristics. For instance, Kogan *et al.* [134] proposed substrate edge effects in films thinner than the effective penetration depth, whereas recently Benfatto and coworkers [135] proposed a renormalization group study for such situation, but their approach implies to estimate the global resistivity of the sample by just averaging the ones of the homogeneous domains. This assumption could be expected to be adequate only if the current itself is homogeneous in the sample (see also below).

In this chapter, we use mesh-circuit numerical analyses to study the BKT non-ohmic features that result from considering a type-II 2D superconductor having a Gaussian distribution of inhomogeneities of $T_{\rm cond}$ and $T_{\rm phase}$, randomly located in space and with long characteristic lengths (much larger, in particular, than the in-plane superconducting coherence length amplitude). Our analysis allows to obtain the evolution of α with temperature, and also shows that significant redistributions of the local currents (and, therefore, voltage drops) occur in the sample as T and I are varied. To get a first

glimpse of some of the main difficulties of the addressed problem, let us first consider two oversimplified cases of T_c-inhomogeneities: *i)* First, a film with domains corresponding to rectangular halves situated with respect to the current contacts in series configuration, and *ii)* the same situation but with domains in parallel with respect to the current contacts. In the first case, obviously the current passes through both zones without any spatial redistribution as T or I varies, and the total resistivity is simply the average of the resistivities of both zones. However, even in this uncomplicated case the exponent α of the whole sample will not be just the average of the α-values of both zones, as the larger contribution to the total V drop (and hence to the global $V \propto I^{\alpha}$ behaviour) happens in the zone with *larger* resistivity. Now we consider the situation *ii)* where the two T_c-zones are in parallel configuration. In this case, when either T or I are varied, and with them the quotient of the resistivities of the two zones, there will be spatial redistributions of the currents. In fact, at some T-I combinations, these redistributions will be extreme enough as to become percolating-like. Correspondingly, the contribution to α from both zones will be now very different to the one in case *i)*. For instance, the global resistivity will greatly differ from the average of both zones and the main contribution to α will be given now by the zone with *lower* resistivity. Obviously, a realistic model of a randomly inhomogeneous sample will include many domains both in series and in parallel. It will be then nontrivial to know if α will be dominated by the zones with higher or lower T_c values. Also, a sizeable part of the (T, I) phase diagram will be affected by percolating-like effects. This makes it difficult to successfully formulate in a comprehensive T, I range an analytic estimate for α in terms of simple averages. These difficulties lead us to use finite-element numerical simulations and effective-medium approaches to analyze the problem.

3.2 Summary of the theoretical approaches for homogeneous systems

3.2.1 Superconducting contributions to the conductivity near the BKT transition at zero applied magnetic field

To study the $V - I$ characteristics of a type-II 2D superconductor with a spatially-random Gaussian distribution of $T_{\rm phase}$ and $T_{\rm cond}$, we need first the $V - I$ expressions for homogeneous superconductors around the transition, including also the vicinities of $T_{\rm phase}$ and $T_{\rm cond}$. We will adopt in this chapter the corresponding $V - I$ expressions proposed by HN in [43], that consider different T-regimes depending on whether $T > T_{\rm phase}$ or not, and can be summarized as follows:

i) Temperatures $T > T_{\rm phase}$. In this T-range the superconducting contribution to the electrical conductivity corresponds to the existence of thermal fluctuations of the order parameter without vortex-antivortex binding effects. Although this T-region could be further subdivided regarding their different regimes of superconducting fluctuations, HN propose [43] an useful interpolation formula that covers the results, with accuracy well

sufficient for the purposes of the present chapter:[1]

$$\Delta\sigma = \frac{0.37\sigma_n}{b_0}\sinh^2\sqrt{\frac{b_0\,\Delta_{\mathrm{BKT}}}{T-T_{\mathrm{phase}}}} \quad (\text{for } T > T_{\mathrm{phase}}), \tag{3.1}$$

where $\Delta\sigma$ and σ_n are, respectively, the superconducting and normal contributions to the in-plane electrical conductivity, and b_0 is a dimensionless parameter for which HN do not propose any definite value, stating only that it may be expected to be of the order of unity. However, let us already mention here that the value of b_0 will be further constrained when considering the expressions for $T < T_{\mathrm{phase}}$ (see point *ii* below). Note also that equation (3.1) corresponds to an ohmic $\Delta\sigma$ (if considering an ohmic σ_n, as will be done in all this work).

ii) Temperatures $T < T_{\mathrm{phase}}$. In this T-range, the relevant degrees of freedom for the superconducting fluctuations are given by the vortex-antivortex binding processes. This region may be subdivided into two: In the range of temperatures closer to T_{phase} than Δ_{BKT} the fluctuations are full-critical, while for lower temperatures the superconductor follows a conventional Ginzburg-Landau behaviour. Following again the ideas of HN we summarize into one common expression the $\Delta\sigma$ results for both T-regions at a fixed current density j: [37, 40]

$$\Delta\sigma = \frac{\sigma_n}{2(\alpha-3)}\left(\frac{j}{j_0}\right)^{1-\alpha} \quad (\text{for } T < T_{\mathrm{phase}}), \tag{3.2}$$

where $j_0 = ek_{\mathrm{B}}T_{\mathrm{phase}}/(\hbar d\xi_{\mathrm{abBKT}})$ is the Ginzburg-Landau critical current density at T_{phase}, e the electron charge, k_{B} the Boltzmann constant, $\hbar$ the reduced Planck constant, d the sample thickness, $\xi_{\mathrm{abBKT}} = \xi_{\mathrm{ab}}(0)(T_{\mathrm{cond}}/\Delta_{\mathrm{BKT}})^{1/2}$ and $\xi_{\mathrm{ab}}(0)$ the Ginzburg-Landau in-plane coherence length extrapolated to respectively T_{phase} and $T = 0$K,

[1] Actually, as also discussed in section 1.2.3, the $T > T_{\mathrm{phase}}$ region has to be further divided in the following three T-ranges: (a) $T_{\mathrm{phase}} < T < T_{\mathrm{LG}}$ [equivalent to $T > T_{\mathrm{phase}}$ and $\varepsilon < \varepsilon_{\mathrm{LG}}$, note that $T_{\mathrm{LG}} = T_{\mathrm{cond}}\exp(\varepsilon_{\mathrm{LG}}) \simeq T_{\mathrm{cond}}(1+\varepsilon_{\mathrm{LG}})$], where the fluctuations are full-critical and dominated by vortices; (b) $T_{\mathrm{LG}} < T < T^{\mathsf{C}}$, where the fluctuations are Gaussian and dominated by non-topological variations of phase and amplitude of the order parameter, and given by the GGL approaches extended to also cover the short-wavelength high-ε effects; and (c) $T > T^{\mathsf{C}}$, where the superconducting fluctuations are null due to the constraints of the uncertainty principle on the superconducting coherence length. The expression 3.1 was proposed by HN as an useful interpolation formula reproducing the essential features of all the regions above T_{phase}. A more precise account of $\Delta\sigma$ in each region is given in our discussion of actual experimental data in chapter 4, in particular by equation 4.1 for (a), equation 4.2 for (b) and $\Delta\sigma = 0$ for (c). We have checked that using this more complex formulae set instead of equation 3.1 does not significantly change the conclusions presented in the present chapter, that will be focused mainly in the low-ε regions. But they do significantly increase the computing time of our calculations, and also add complexity to the presentation of the results.

$\alpha = \max(\alpha_T, \alpha_J)$, $\alpha_J = 3 - 1/\ln(j/j_0)^2$, and α_T is:[2]

$$\alpha_T = \begin{cases} 3 + \pi\sqrt{\frac{T_{\text{phase}} - T}{b_0\,\Delta_{\text{BKT}}}} & (\text{for } T_{\text{phase}} - \Delta_{\text{BKT}} < T < T_{\text{phase}}), \\ 1 + 2b_1\frac{T_{\text{cond}} - T}{\Delta_{\text{BKT}}} & (\text{for } T < T_{\text{phase}} - \Delta_{\text{BKT}}). \end{cases} \tag{3.3}$$

Note that $\alpha_T \to 3$ when $T \to T_{\text{phase}}$ from below, and then at T_{phase} it is $\Delta\sigma \propto j^{-2}$, *i.e.*, $V \propto I^3$ (neglecting the small effect of α_J and of any other contributions to the conductivity). The parameter b_1 in equation (3.3) takes into account the variations of the value of Δ_{BKT} with respect to the purely 2D non-fluctuation GL value.[3] In the theoretical simulations done in this work, for simplicity we will neglect such differences and take $b_1 = 1$ (except for the comparison with some experimental data of previous authors shown in figure 3.8, where b_1 has been fine-tuned to the value $b_1 = 2$). Note also that to ensure continuity at $T = T_{\text{phase}} - \Delta_{\text{BKT}}$ of equation (3.3) (and thus of equation (3.2)) it is needed that the parameter b_0 takes the value $b_0 = \pi^2/(4b_1 - 2)^2$, rather than being a somewhat free choice as suggested by HN. [43]

3.2.2 Other contributions to the conductivity near the BKT transition

To obtain the total conductivity σ of the superconductor we must add to the above formulae for $\Delta\sigma$ the contributions from the rest of electrical transport channels in the system, mainly the conductivity σ_n due to the normal-state carriers:

$$\sigma = \Delta\sigma + \sigma_n \tag{3.4}$$

Indeed σ_n will be negligible against $\Delta\sigma$ for $T \lesssim T_{\text{phase}}$, but for larger temperatures it won't be so. Note also that σ_n may be T-dependent. For instance in the optimally-doped HTS it may be well approximated as inversely proportional to T (as will in fact be used in our simulations, see below).

Other contributions to the total conductivity will be neglected, but we note here that in certain specific experimental circumstances they could become appreciable: For instance, for $T \lesssim T_{\text{phase}}$ we neglect the ohmic conductivity that may appear at very low intensities when the vortex-antivortex pairs breaking processes involve distances larger than the inhomogeneity size (see, *e.g.*, [43]). We also neglect the non-ohmic contributions

[2] For $T < T_{\text{phase}} - \Delta_{\text{BKT}}$, α_T may be also affected by vortex-antivortex pinning [43,136], that in turn may depend on the detailed structural properties of each sample (defects, boundary conditions, etc.). Equation 3.3 implicitly assumes, for $T < T_{\text{phase}}$, negligible pinning effects. Note that almost all of the results of this chapter (and also of this thesis as a whole) concern the $T > T_{\text{phase}} - \Delta_{\text{BKT}}$ region.

[3] As shown, *e.g.*, in [76], in layered superconductors weak interlayer interactions displace T_{phase} (and hence change $\Delta_{\text{BKT}} = T_{\text{cond}} - T_{\text{phase}}$) from the purely 2D prediction $k_{\text{B}}T_{\text{phase}} = \phi_0^2 d/[32\pi^2\mu_0\lambda_L^2(T_{\text{phase}})]$, where d is the interlayer distance, $\lambda_L(T_{\text{phase}})$ the in-plane penetration depth at T_{phase}, ϕ_0 the flux quantum and μ_0 the vacuum permeability. Such interlayer interactions will also change the size of the full-critical region. [16, 71]

to $\Delta\sigma$ that may appear above T_{phase} due to the superconducting fluctuations not related to the vortex-antivortex correlations. The latter contributions have been thoroughly explored previously (see, *e.g.*, [137–140]) and today are well known to be significative only at electrical fields much larger than those considered in our study (see, *e.g.*, figure (1) of [141]). Finally, we also mention that we neglect the indirect contributions to the paraconductivity above the transition, such as the so-called Maki-Thomson and density-of-states contributions. [9] It is today quite well accepted that such contributions are negligible in the case of HTS [9, 15, 89, 129, 142] although the situation is not as clear in the case of low-T_{c} superconducting thin films. [143] We have checked however that including any of such contributions in our simulations does not qualitatively affect the main results presented in this chapter.

3.3 Procedure for the numerical simulation of the $V - I$ characteristics near the BKT transition of an inhomogeneous superconductor

Our aim is to obtain the $V - I$ characteristics of a 2D superconductor composed by randomly-located domains, each domain having its own single T_{cond} and T_{phase} resulting from a Gaussian probability distribution, and each domain following the $V - I$ characteristics described in the previous section. For this purpose, in the spirit of the finite-element methods we model the inhomogeneous superconductor as a $N \times N$ square mesh of resistors (see figures 3.1 to 3.4). We randomly assign to each node of the mesh a different T_{cond}, taken from a Gaussian distribution with mean-value $\overline{T}_{\text{cond}}$ and FWHM ΔT_{c}, and we assign to each resistor the T_{cond} of its corresponding left-lower node. The difference $T_{\text{cond}} - T_{\text{phase}}$ is held constant for all resistors, so that the distribution of T_{phase} follows the one of T_{cond} and is Gaussian with mean-value $\overline{T}_{\text{phase}}$ and FWHM again ΔT_{c}. We also include in our model an external circuit composed by a current source connected with zero-resistance contacts to opposite borders of the sample (*i.e.*, to all the nodes of the corresponding border). When referring to the results of our simulations, by I we mean this external bias current and by V the voltage drop between those opposite contacts. The sample is considered to have width and length w and thickness d.

Because the resistivity of each resistor depends on the local current passing through it (see previous section), the mesh equations that result from that modeling are nonlinear and in general do not admit analytic solution. They have to be solved using numerical methods, of which we use Newton-type iterations. For those iterations to succeed, it is crucial to start them from initial values not too far from the solution. Thus, to calculate each $V - I$ curve at a fixed temperature, we applied the following algorithm, that proved itself to be well adapted to the non-ohmic features of the BKT transition (as it solves the instability problems that we found trying other simulation strategies): Our analysis starts by considering first a high temperature $T_{start} \gg \overline{T}_{\text{cond}}$ (where the system is ohmic and easy to solve) and a high bias intensity $I_{start} = (wd/10)j_0$. The analysis then evolves keeping the bias intensity constant but lowering the temperature, evaluating at

each T-step the mesh equations by means of Newton iterations with starting point the final result of the previous step. The T-decrement separating each step is adaptively updated during the simulation, so that voltages are not allowed to vary beyond 0.1% between steps. Once reached the target temperature at which the $V-I$ curve is to be calculated, the temperature is fixed and then the bias intensity I is varied, again adaptively, iteratively solving the mesh equations at each step and storing the results. Each I-step uses as starting values for the Newton iterations the results obtained in the previous calculated step. As an additional measure to avoid instabilities in the convergence of the Newton iterations, when needed our program smoothes over 0.05K the $V(T)$ behaviour of the individual resistors at their local $T_{\rm phase}$ temperature, making its $V(T)$ evolution continuous (but still very rapidly varying). This T-widening of the BKT transition is negligible in any case against the one due to the inhomogeneities considered in our simulations and we have checked that doubling or halving it does not change our final results in any appreciable way.

All of the results presented in this chapter correspond to 10×10 cell meshes. Computation time for a single $V-I$ curve at fixed T is of about three days for a 10×10 mesh in current desktop computers.

3.4 Current paths and voltage maps

Let us now comment on the results obtained when applying the method described in the previous section to compute the $V-I$ curves around the BKT transition, using parameter values typical of HTS film samples. In particular, we have used $\overline{T}_{\rm cond} = 100$K, $\Delta_{\rm BKT} = 2$K (therefore, $\overline{T}_{\rm phase} = 98$K), $\sigma_n = 10^8 T^{-1}$K/Ωm, $\xi_{\rm ab}(0) = 1\,$nm, $d = 100\,$nm and $w = 10^{-3}$m, and we have constructed simulated samples with $\Delta T_{\rm c} = 2$K and 4K.

In figures 3.1 and 3.2 we show some examples of the current distributions within the mesh circuit, obtained for representative values of T and I. The most important feature observed in these results is that significant spatial redistributions of the currents may occur when either T or I are varied. This is a consequence of the fact that the resistance of each mesh element relative to the resistance of the other elements will be dependent on T and I, and therefore the current paths will be also dependent on both of these variables. Due to these redistributions, changes of T and I will also change what are the portions of the sample which dominate the global voltage drop, and its ohmic or non-ohmic character.

We may also note that, as in fact it was already commented in the Introduction, the behaviour of the system in general will be intermediate between the simplest cases of considering all resistors in series (in which case the global resistivity is given by the average of the resistivity of all the elements) or in parallel (in which case the minimum resistance will dominate the transport properties), being the proximity to each situation dependent on I and T. Interestingly, for temperatures above $\overline{T}_{\rm cond}$ the current distribution becomes especially simple: As it can be seen in figures 3.1 and 3.2, at $T \gg \overline{T}_{\rm cond}$ almost all of the current flows longitudinal and uniformly. So, at those temperatures

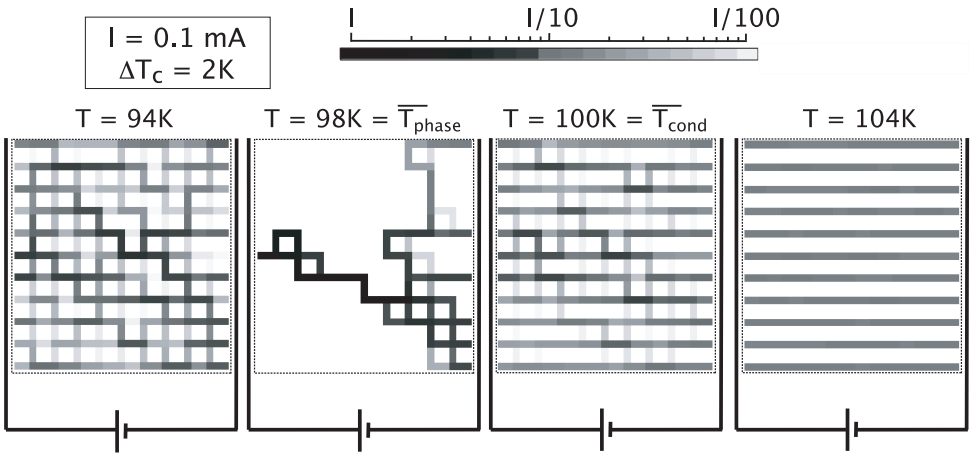

Figure 3.1: Some examples of the evolution of the current distributions obtained in our simulations when the temperature T is varied and the bias intensity I is kept constant. The simulation sample is composed by a 10×10 cell mesh of resistors corresponding to a spatially-random Gaussian distribution of mean-field critical temperatures with average $\overline{T}_{\rm cond}$ and FWHM $\Delta T_{\rm c}$, with the value of $\Delta_{\rm BKT} = T_{\rm cond} - T_{\rm phase}$ being the same for all resistors. In the pictured example, $\overline{T}_{\rm cond} = 100$K, $\Delta_{\rm BKT} = 2$K (so that $\overline{T}_{\rm phase} = 98$K), $\Delta T_{\rm c} = 2$K, the sample width and length is $w = 10^{-3}$m and its thickness is $d = 100$nm. We also used (see main text) $b_1 = 1$, $\sigma_{\rm n} = 10^8 T^{-1}$K/$\Omega$m and $\xi_{ab}(0) = 1$nm. The bias current I is the one provided by the external current source, which is connected to opposite borders of the superconductor with zero-resistance contacts. Note the strong spatial redistribution of currents inside the superconductor as T is varied through the transition, indicating that at each temperature different regions of the superconductor determine the global resistivity, and its ohmic or non-ohmic character. These redistributions are specially intense near the average BKT transition temperature where the current flows through only a few less resistive paths. It may be also observed that for $T \gg \overline{T}_{\rm cond}$ almost all of the current flows longitudinal and uniformly, while for $T < \overline{T}_{\rm phase}$ transversal current paths are significant.

the global resistance may be approximated by the one of a row, which in turn corresponds to the average resistance of the resistors on it. As the temperature is lowered we see however that the current path geometry is no longer that simple, nor constant with T or I. In fact, it is observed that one of the interesting features introduced by inhomogeneities near the BKT transition is the significant spatial redistributions in the map of local currents. Even for $T < \overline{T}_{\rm phase}$ the current does not flow longitudinally, and transversal current paths remain significant.

In figures 3.3 and 3.4 we show some examples of the voltage distribution, as a function of T in figure 3.3 and as a function of I in figure 3.4. We observe that the isovoltage fronts are in first approximation essentially perpendicular to the current paths. This also holds when the current configurations are percolating-like (as it happens for instance for

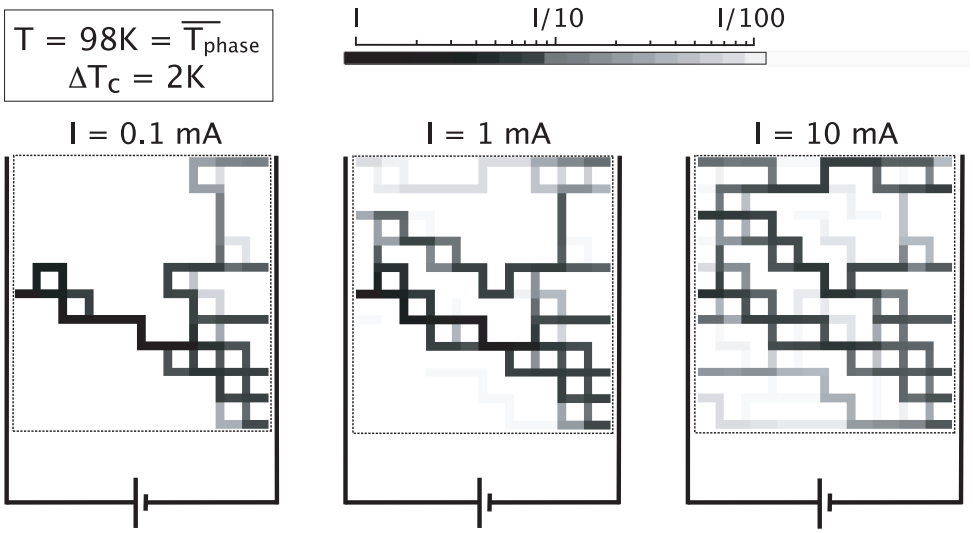

Figure 3.2: Some examples of the current redistributions obtained in our simulations, when the bias intensity I is varied and the temperature T is constant. The simulation sample is the same as in figure 3.1. The fact that different regions of the inhomogeneous sample contribute to the electric transport as I changes indicates that the log-log slope of $V(I)$ may vary as I is varied, in spite of the power-law-like $V \propto I^{\alpha}$ behaviour of the homogeneous case. This change in slope is appreciable in the figures 3.5(a) and 3.5(b).

small currents at the average BKT temperature, $\overline{T}_{\rm phase} = \overline{T}_{\rm cond} - \Delta_{\rm BKT}$). Let us already note here that this result tells in advance about the applicability of the effective-medium approaches, as that approach assumes voltage maps similar at the perturbative level to the one of a homogeneous sample. Therefore, figures 3.3 and 3.4 provide a first indication that an effective-medium approach could be appropriate for temperatures sufficiently above or below $\overline{T}_{\rm phase}$, while it could be less accurate in the close proximity of $\overline{T}_{\rm phase}$ where percolation and complex isovoltage fronts occur.

Note also that the appearance of percolation paths at $\overline{T}_{\rm phase}$ is coherent with the predictions of the general theories of flow through inhomogeneous conductors, [144] according to which the percolation paths in 2D systems tend to first appear when 50% of the medium is in a low resistance state. Combined now with the fact that the drops of voltage follow at $\overline{T}_{\rm phase}$ such paths, this leads us to present here an explanation for the fact that the global $V - I$ exponent of the sample becomes $V \precsim I^3$ precisely at $\overline{T}_{\rm phase}$, as follows: Note first that each percolation path can be seen as formed by resistors associated among them in series. Note secondly that the maximum $T_{\rm phase}$ value among those resistors is $\overline{T}_{\rm phase}$ due to the 50% condition. Finally, note that along such a combination in series of resistors the global voltage drop will be dominated by the one with

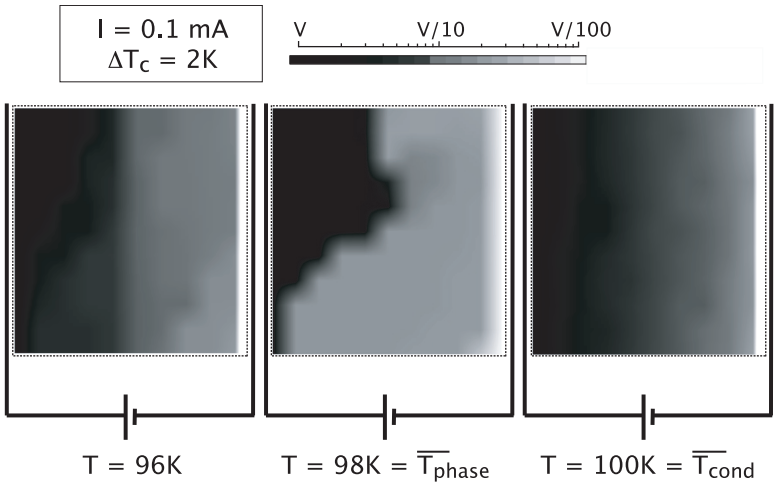

Figure 3.3: Example of the evolution of the local voltages obtained in our finite-element calculations when the temperature T is varied and the external current I is constant. The voltage map is made continuous by 2nd-order polynomial interpolation. We have used the same simulation sample and parameters as in figures 3.1 and 3.2.

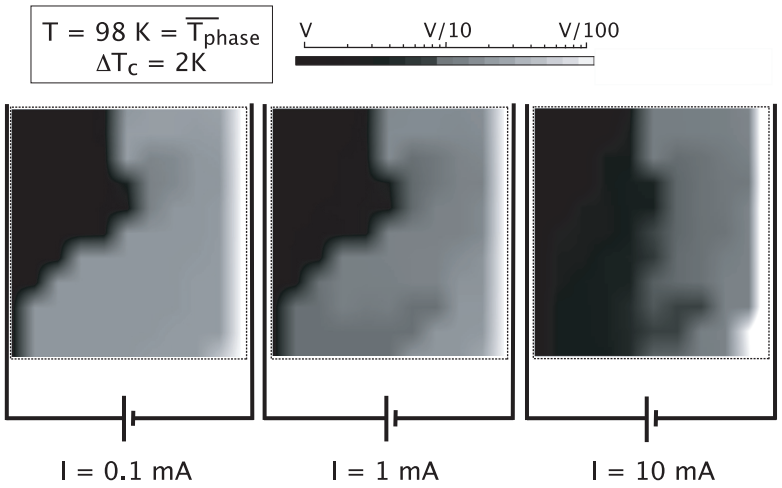

Figure 3.4: Example of the evolution of the local voltages obtained in our finite-element calculations when the external current I is varied and the temperature T is constant, using the same simulation sample and parameter values as in figures 3.1 to 3.3.

largest resistance (in our case, by the maximum BKT temperature along the percolation path, *i.e.*, $\overline{T}_{\rm phase}$). As a result of all of the above, when $T \simeq \overline{T}_{\rm phase}$ the voltage drop is dominated by resistors with $T_{\rm phase} = \overline{T}_{\rm phase}$, for which $V \propto I^3$.

3.5 $V - I$ characteristics and α exponent

In figures 3.5(a) and 3.5(b) we show the $V - I$ curves that result from our simulations. As mentioned previously, here V and I correspond to the global values, *i.e.*, those in the external bias circuit. The log-log slope of these curves corresponds to the exponent α in the $V \propto I^{\alpha}$ dependence. It is evident in figures 3.5(a) and 3.5(b) that α depends on temperature. As it could be expected, ohmic behaviour (*i.e.*, slope unity) is obtained for temperatures well above $\overline{T}_{\rm phase}$, while much larger log-log slope is obtained well below that temperature. For temperatures close to $\overline{T}_{\rm phase}$ the change in behaviour is not discontinuous, being instead somewhat broadened by inhomogeneities, although the T-range where that broadening occurs is significantly smaller than $\Delta T_{\rm c}$. This change in the log-log slope may be seen more accurately in figure 3.6, where $\alpha(T)$ is plotted for all of the simulated samples, together with the theoretical $\alpha(T)$ corresponding to the homogeneous case. To obtain this figure 3.6, α was calculated trough a power-law fit to our $V - I$ results at voltages around 10^{-5} volt (in particular at $3 \times 10^{-6}\text{volt} \leq V \leq 3 \times 10^{-5}\text{volt}$). The reason why it is necessary to specify a voltage range for the obtainment of α is that, as may be noticed in figures 3.5(a) and 3.5(b), in the inhomogeneous samples for temperatures close to $\overline{T}_{\rm phase}$ the $V - I$ dependence is not perfectly power-like, but rather the log-log slope depends also on the applied current. The cause behind this fact is the existence of local current redistributions, shown in figures 3.1 and 3.2 (*i.e.*, changes in I vary the region of the sample where the voltage drops, and thus its global ohmic or non-ohmic character).

In figures 3.5 to 3.8 it is easily visible that our simulation results meander (*i.e.*, randomly and smoothly oscillate around their central tendency) when represented against either the current or the temperature. This meandering corresponds to the uncertainty of our numerical approach. In fact, for each set of parameter values (*e.g.*, the same ΔT_c in figures 3.5 to 3.7) we have run our simulations in various different random inhomogeneity distributions (from 5 to 10 different samples) and we have checked that the results are within the range of oscillation of the curves in figures 3.5 to 3.8. The meandering may indeed be reduced if averaging the results of the various simulated samples, but then it would no longer correspond to our uncertainty range. Therefore, each of the simulation curves represented in the figures of this chapter corresponds to one, non-averaged, simulation run. Also, to facilitate the comparisons, in figures 3.5 to 3.7 for each ΔT_c we have always used the same simulated samples.

Other important feature to be observed in figure 3.6 is that the criterion $\alpha(T = T_{\rm phase}) = 3$ to determine $T_{\rm phase}$ remains essentially valid in spite of the inhomogeneities, if we apply it to determine now its average value $\overline{T}_{\rm phase}$: For all the $\Delta T_{\rm c}$ values studied, the condition $\alpha = 3$ provides a good estimate for $\overline{T}_{\rm phase}$, underestimating it only slightly (see figure 3.6; in particular the deviation from the exact value is well smaller than $\Delta T_{\rm c}$).

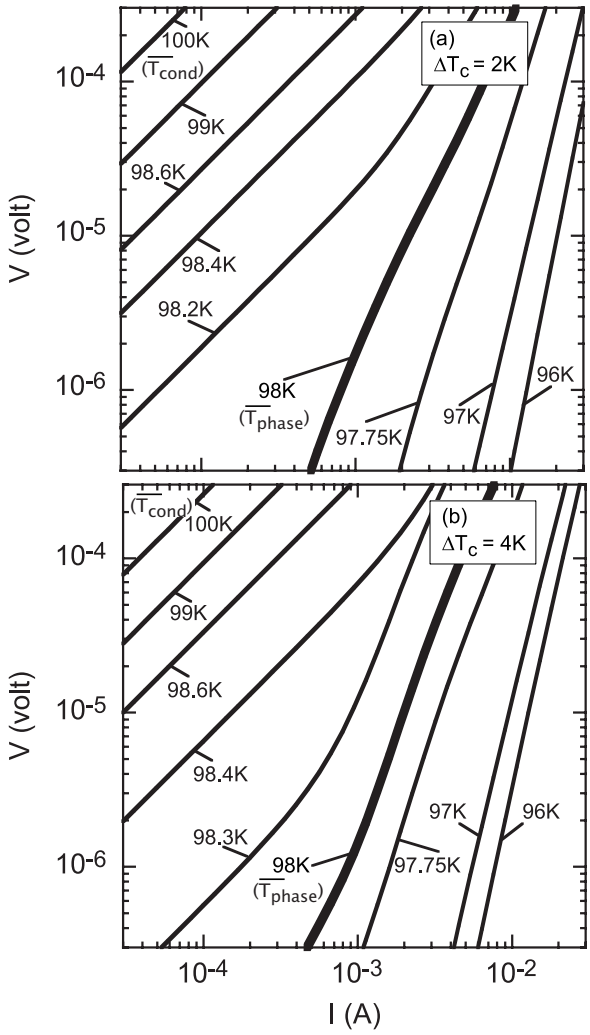

Figure 3.5: $V - I$ results at various constant temperatures around the BKT transition as obtained in our simulations in two planar superconductors with (a) $\Delta T_{\rm c} = 2$K and (b) $\Delta T_{\rm c} = 4$K. In both cases we have used the same parameters as in figures 3.1 to 3.4. We have also used $b_1 = 1$ (see main text). The log-log slope of these $V - I$ results corresponds to the exponent α (see also figure 3.6). The $T = \overline{T}_{\rm phase}$ isotherm (thickest line) presents $\alpha = 3$, while the $T = \overline{T}_{\rm cond}$ isotherm (upper line) is ohmic ($\alpha = 1$). Note that non-ohmic behaviour appears in these inhomogeneous superconductors already above $\overline{T}_{\rm phase}$. Note also that the log-log slope may vary with I or V. In this work the results reported for $\alpha(T)$ correspond to the V-range 3×10^{-6} to 3×10^{-5}volt.

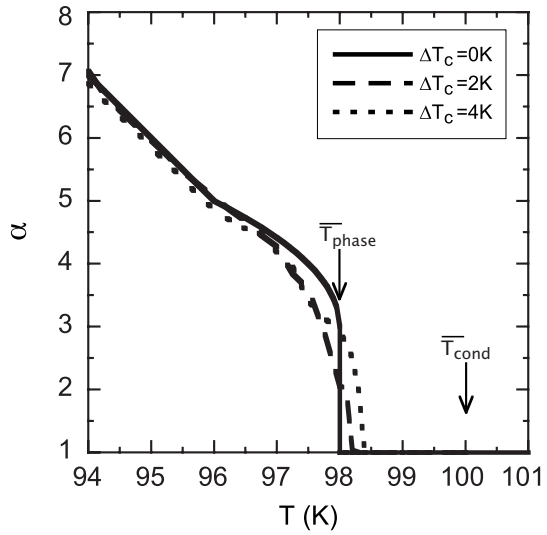

Figure 3.6: The exponent α in $V \propto I^{\alpha}$ extracted as the log-log slope of the simulation results shown in figures 3.5(a) and 3.5(b), in the range 3×10^{-6} to 3×10^{-5}volt. The homogeneous case, $\Delta T_{\rm c} = 0$K, is also shown for comparison (see section 3.2). Note that the condition $\alpha = 3$ provides a good estimate for $\overline{T}_{\rm phase}$.

The effects of the inhomogeneities in the dc electrical transport properties become more apparent in the $R(T)$ curves obtained at different fixed external currents I. Here we define R as simply V/I. In figures 3.7(a) and 3.7(b) we show the $R(T)$ results obtained from our simulations at different fixed I values, for samples with different $\Delta T_{\rm c}$ values and using a logarithm axis for the resistance. It may be seen in these figures that the application of a finite current broadens the $\log[R(T)]$ tail in the lower part of the superconducting transition, and that this happens to a larger extent as $\Delta T_{\rm c}$ is increased. It is also easily noticeable that the non-ohmic behaviour sets in at temperatures above $\overline{T}_{\rm phase}$. We conclude that the inhomogeneities are detectable over a larger T-range on the amplitude of the resistance than on the α exponent.

Let us now discuss how the results obtained with our simulation procedure compare with some of the experimental data obtained by earlier authors measuring the $V - I$ characteristics near the BKT transition. Specifically, we will use for these comparisons the $\alpha(T)$ measurements of Refs. [59] and [60], as in these works $\alpha(T)$ was extracted using a voltage criterion similar to the one used in our simulations. These measurements were performed in Ref. [59] in $Tl_2Ba_2CaCu_2O_8$ 700nm-thick films (see in particular figure 3(a) of that work) and in Ref. [60] in $YBa_2Cu_3O_{7-\delta}$ 120nm-thick films (see figure 2 of that work). We show in our figure 3.8 a comparison between these experimental $\alpha(T)$ and our simulation results. To be able to gather together in a single representation the two

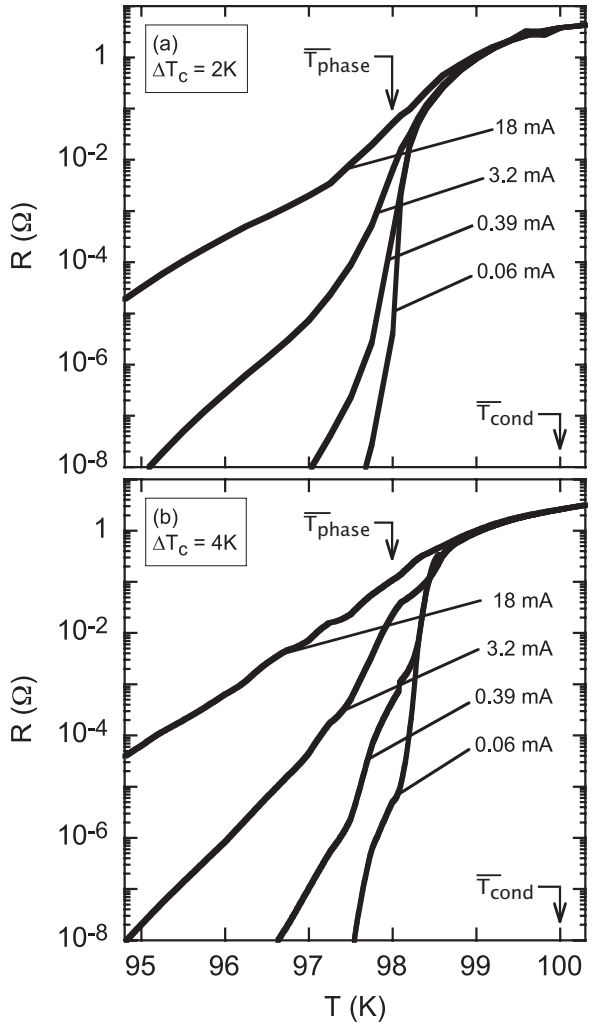

Figure 3.7: Resistance versus temperature at various constant bias currents as resulting from the quotient V/I in the same simulation runs as in figures 3.5(a) and 3.5(b) for superconductors with (a) $\Delta T_{\rm c} = 2$K and (b) $\Delta T_{\rm c} = 4$K. The logarithmic scale allows to better appreciate that the tail of the resistive transition is broadened when the current is increased and that the effect is larger for the samples with a larger $\Delta T_{\rm c}$. Note also that non-ohmic behaviour sets in already above $\overline{T}_{\rm phase}$.

samples in spite of their different critical temperatures, we have chosen for the horizontal axis the normalized quantity $(T-\overline{T}_{\rm phase})/\Delta_{\rm BKT}$. We employed for each sample the $\overline{T}_{\rm phase}$ that results from applying the condition $\alpha(\overline{T}_{\rm phase}) = 3$, and the $\overline{T}_{\rm cond}$ that results from

extrapolating to $\alpha \to 1$ the low-temperature $\alpha(T)$ data. We obtained $\overline{T}_{\rm phase} = 99.0$K and $\overline{T}_{\rm cond} = 100.2$K for Ref. [59] and $\overline{T}_{\rm phase} = 83.45$K and $\overline{T}_{\rm cond} = 85.95$K for Ref. [60]. In our simulations we have used the same parameter values as for the simulations shown in figures 3.1 to 3.7, except for $\Delta T_{\rm c} = 4$K and $b_1 = 2$. These latter values were found to be the ones producing a better agreement between those data and our simulations (note that in the case of b_1 its value is governed mainly by the data for $T < \overline{T}_{\rm phase} - \Delta_{\rm BKT}$, outside of the region significantly affected by inhomogeneities). As may be seen in the figure 3.8, the agreement between experiments and simulation is rather satisfactory, despite the necessary crudeness of some of our approximations (perfectly Gaussian distribution of the $T_{\rm c}$-inhomogeneities, uniform $\Delta_{\rm BKT}$ value, inexactness of any finite-element method, etc.).

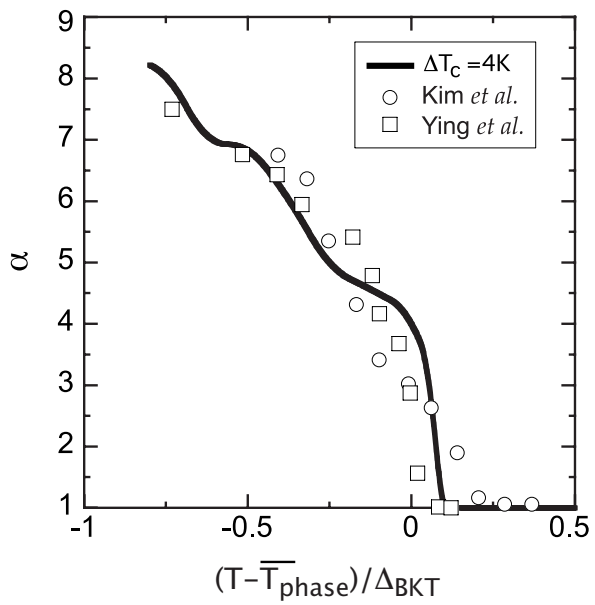

Figure 3.8: Comparison between the exponent α obtained experimentally in HTS in Ref. [59], by Kim *et al.*, and in Ref. [60], by Ying *et al.*, (circles and squares respectively) and our simulations (solid line). The experimental data were obtained by means of $V-I$ measurements in $Tl_2Ba_2CaCu_2O_8$ 700nm-thick films [59] and in $YBa_2Cu_3O_{7-\delta}$ 120nm-thick films [60]. In this comparison we employed for $\overline{T}_{\rm phase}$ the values that result from the condition $\alpha = 3$, and for $\overline{T}_{\rm cond}$ the values that result from extrapolating to $\alpha \to 1$ the low-temperature $\alpha(T)$ data. We obtained $\overline{T}_{\rm phase} = 99.0$K and $\overline{T}_{\rm cond} = 100.2$K for Ref. [59] and $\overline{T}_{\rm phase} = 83.45$K and $\overline{T}_{\rm cond} = 85.95$K for Ref. [60]. We also used the values $\Delta T_{\rm c} = 4$K and $b_1 = 2$, which produce the best agreement with these $\alpha(T)$ data.

3.6 Effective-medium calculations of the global resistance

Although the finite-element analyses presented in the previous sections seem to clarify the influence of random T_c inhomogeneities in the transition around $\overline{T}_{\rm phase}$, and importantly seem to support the condition $\alpha(T = T_{\rm phase}) = 3$, it will prove greatly useful in our chapter 4 to have also available a more analytically direct way to compute such effects. For that reason, we explore here an affective-medium approach, that can be considered as an intermediate approach between these numerical simulations and straight-volume-averages of the conductivity (which as already discussed in section 3.1 can be expected to be a too simplified approach). Crucial aspects to be studied here are not only writing down such effective-medium approximation, but also determining its range of validity, for which the discoveries of the existence of local current redistributions around $\overline{T}_{\rm phase}$ made in our previous sections will be very important (the effective-medium approximation will not be valid when these redistributions appear, *i.e.*, too close to $\overline{T}_{\rm phase}$).

A general description of the effective-medium approaches can be found, *e.g.*, in Ref. [127,145] (for the case of the superconducting transition well above $T_{\rm cond}$ and without considering the BKT effects) or in Ref. [144] (for the case of flow in general inhomogeneous materials having low and high resistance phases). The key starting premise of these theories is to approximate the behaviour of each of the resistive elements composing the sample by the one that it would have when subjected to a voltage similar at the perturbative level to the value in a purely homogeneous sample (the effective-medium approximation). They result then in a non-explicit equation for the global conductivity of the sample, σ, to be solved numerically:

$$\int_0^\infty \frac{\sigma_{T_c'} - \sigma}{\sigma_{T_c'} + 2\sigma} \exp\left[-\left(\frac{T_c' - \overline{T}_{\rm cond}}{\frac{\Delta T_c}{2\sqrt{\ln 2}}} \right)^2 \right] \frac{{\rm d}T_c'}{\Delta T_c} = 0, \tag{3.5}$$

where $\sigma_{T_c'}$ is the conductivity of a homogeneous sample with a single mean-field critical temperature $T_{\rm cond}$ (and a single BKT temperature $T_{\rm cond} - \Delta_{\rm BKT}$) and we have already used for the distribution of critical temperatures a Gaussian distribution (via the exponential factor in the integrand). As $\sigma_{T_c'}$ is dependent on the current density in the non-ohmic range $T \leq T_{\rm phase}$ (see Ref. [43] and above in this chapter), for those temperatures and in the spirit of the effective-medium approximation we evaluate it by considering a uniform current density.

In figure 3.9 we show, as a function of T and for various values of I, the resistance V/I resulting from the σ obtained by numerically solving equation (3.5). This figure also compares such results with the ones obtained from the finite-element mesh analysis method. As it is evident in figure 3.9, except in the close vicinity of $\overline{T}_{\rm phase}$ the effective-medium approach provides a valid approximation for the rounding of the resistance of the superconductors with Gaussian inhomogeneities of the critical temperature. For the upper part of the transition, the temperature range in which good agreement is obtained includes also the vicinity of $\overline{T}_{\rm cond}$ and it can be roughly identified with the region at which

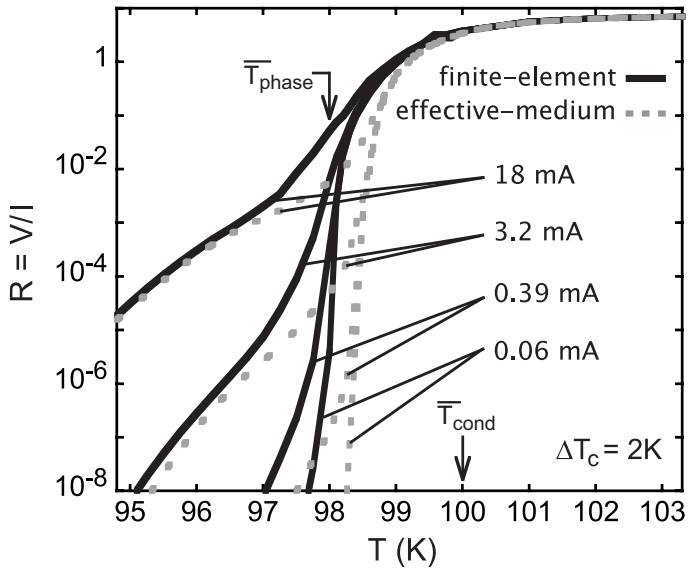

Figure 3.9: Resistance V/I resulting from our calculations using the finite-element computations (solid lines) and the effective-medium approximation (dashed lines), using the same simulation sample and parameter values as in figures 3.1 to 3.4. Note that the effective-medium method provides a good approximation for temperatures above ~ 99K (which includes in particular also $\overline{T}_{\rm cond}$) and below ~ 97K, while for intermediate temperatures it just provides a crude approximation.

the predictions are still ohmic. For the lower part of the transition, the effective-medium approach provides a fair agreement with the finite-element calculations when the spatial distributions of local currents and voltages are no longer percolating-like. In contrast, the agreement is worse in the vicinity of $\overline{T}_{\rm phase}$ where strong spatial redistributions of current and voltages occur (for those intermediate temperatures the effective-medium approach provides only an interpolation that, nonetheless and taking into account that the vertical axis in figure 3.9 is logarithmic, could serve as a first crude approximation to the finite-element results).

3.7 Conclusions

We have analyzed numerically the effects of a spatially-random Gaussian distribution of critical temperature inhomogeneities with long characteristic lengths on the voltage-current $V - I$ characteristics of a type-II planar superconductor near the Berezinskii-Kosterlitz-Thouless (BKT) transition. The simulations allow to quantify the broadening around the average BKT transition temperature $\overline{T}_{\rm phase}$ of both the exponent α in $V \propto I^{\alpha}$ and of the resistance V/I. These calculations reveal that strong spatial redistributions of the local current and voltage drops will occur around the transition as either I or T are varied. Our results also support that the condition $\alpha = 3$ provides a good estimate for the location of the average BKT transition temperature $\overline{T}_{\rm phase}$. These results are in good agreement with some experimental measurements of the exponent $\alpha(T)$ obtained by earlier authors on HTS films. [59,60] In addition, we have implemented effective-medium calculations instead of finite-element computations on the same samples. Then, we have obtained that the effective-medium results agree well with the finite-element ones except for the region close to $\overline{T}_{\rm phase}$, where the percolating strong current redistributions appear, making necessary a more detailed computation instead of an interpolating one.

USC
UNIVERSIDADE
DE SANTIAGO
DE COMPOSTELA

Chapter 4

Measurement of T_{phase} and T_{cond} as a function of doping in $\mathbf{La}_{2-x}\mathbf{Sr}_{x}\mathbf{CuO}_{4}$ superconductors.

Summary of the chapter:

In this chapter, we report on the measurements of two of the main characteristic features expected in the transport properties near $T_{\rm phase}$ and $T_{\rm cond}$: For $T_{\rm phase}$, the so-called Halperin-Nelson jump in the current-voltage exponent $V \propto I^{\alpha}$ from the ohmic behaviour $\alpha = 1$ up to $\alpha = 3$. [43] This is a sharp feature particularly exclusive of a phase coherence transition and is almost unaffected by possible inhomogeneities (see chapter 3 and Refs. [135, 146] For $T_{\rm cond}$, the specific critical rounding of the resistance V/I due the fluctuating vortices and superconducting carriers above $T_{\rm phase}$. [9, 43] The obtained $T_{\rm cond}(x)$ and $T_{\rm phase}(x)$ phase diagram lines result to be parabolas (with a slight depression near $x = 1/8$) that for all dopings are not further away than $\sim$ 4K from the $T_{\rm c}(x)$ line in which the macroscopic superconducting phenomenology appears. These small differences between $T_{\rm cond}$, $T_{\rm phase}$ and $T_{\rm c}$ for the underdoped, optimally-doped and overdoped samples suggest theoretical scenarios different from the strong phase-fluctuation pairing models, [3, 20–22] in which $T_{\rm c}$ is primarily determined by the vortex-antivortex binding instead of the pairing between single-particle normal carriers (*i.e.*, $T_{\rm cond} \gg T_{\rm phase}$ and $T_{\rm phase} \simeq T_{\rm c}$). Our results are coherent instead with pairing models in which both $T_{\rm cond} - T_{\rm phase}$ and $T_{\rm cond} - T_{\rm c}$ are small ($\lesssim$ 5K) for all dopings. [5, 30, 48, 49, 51–58].

4.1 Introduction

As already commented on in our introductory chapter 1, a central issue for cuprate superconductors (HTS) is to experimentally establish the location of the transition temperatures for superconducting phase coherence, $T_{\rm phase}$ and wave function condensation, $T_{\rm cond}$ as a function of doping and in samples as homogeneous as possible. [1–3,20] Unambiguously measuring both temperatures would provide pivoting information on whether the search for the mechanism behind macroscopic superconductivity (and possibly the quest of increasing the critical temperatures) must focus on the correlations between preformed vortices [3,20–22] or between normal-state quasiparticles [5,48,49,51–55,58]. Up to now, most experimentalists have addressed the issue by searching for traces of precursive vortex-like features well above the macroscopic superconducting transition. [23–29] However, the so-resulting possible positive confirmations have been challenged by plausible alternative explanations in terms, *e.g.*, of chemical disorder and its resulting inhomogeneities of critical temperatures, [34–36] or also in terms of the magnetic-field dependence of different forms of normal-state, non-superconducting orders [30,50–53,55,58].

To shed further light on this issue, in this chapter we report the measurement of $T_{\rm phase}$ as a function of doping by employing one of the most specific features expected to occur when the superconducting phase becomes coherent: We measure the dc $V-I$ characteristics and locate the temperature at which a sharp departure from ohmic behaviour occurs. As we have already said in chapter 3, this change was first researched by Halperin and Nelson (HN) in 1979, [43] who predicted that in 2D superconductors the occurrence of phase coherence and the associated leap of the superfluid density at $T_{\rm phase}$ (Nelson jump) will also produce a jump in the density of the free vortices causing dissipation, inducing for the exponent α of $E \propto J^{\alpha}$ a sudden change at $T = T_{\rm phase}$ from the ohmic value $\alpha = 1$ to the nonlinear one $\alpha = 3$ (being E the electric field and J the current density). [43] When T decreases further below $T_{\rm phase}$, α would increase to even larger values that may depend on the vortex pinning details. [43,136]

The α jump feature provides at least the following experimental advantages to locate $T_{\rm phase}$: First of all, non-ohmic effects in the normal state of HTS are very small and then a sharp α jump feature may be considered a very unambiguous experimental signature for the location of $T_{\rm phase}$. Secondly, as we have shown in chapter 3, the presence of critical temperature inhomogeneities in the material will not significantly shift the $\alpha = 3$ point from the average $T_{\rm phase}$ of the sample

In spite of these advantages, up to now in HTS the α jump feature has been measured only in a few works [59–63,133] that do not explore its evolution with doping (and also did not obtain $T_{\rm cond}$ taking into account the inhomogeneities nor high-reduced-temperature region, see below).

In this chapter we also determine $T_{\rm cond}$ as a function of doping by means of the specific critical rounding of the resistivity produced by fluctuating superconducting carriers. Our present analyses of the fluctuation conductivity present the following advancements: First of all, having access to $T_{\rm phase}$ allows to extend the range of study to temperatures below $T_{\rm cond}$. Secondly, we probe also the high temperature range, by exploiting

the $d\rho/dT$ analysis techniques recently proposed by Rourke and coworkers [29] to find the onset temperature of superconducting fluctuations T^{C}, and by using the high temperature extensions of the fluctuation theories presented in [85, 89]. Very importantly, these extensions (also the one to high temperatures) need a detailed account of the critical temperature inhomogeneities of the samples. We achieve such objective thanks to our independent high-precision magnetometry measurements of the critical temperature dispersion ΔT_c in the same films (see chapter 2) and by applying an effective-medium integration (see chapter 3) to extend the available theory for $T < T_{\rm phase}$ in homogeneous materials to superconductors with critical temperature inhomogeneities.

4.2 Experimental procedure

We perform our measurements in our LS_xCO thin films with dopings $0.11 \leq x \leq 0.22$.[1] To fully take into account in our subsequent studies, at the quantitative level, any uncertainties caused by the superconducting inhomogeneities, and as it was described in chapter 2, we have first directly measured by means of high-precision SQUID magnetometry the full-width at half-maximum dispersion ΔT_c of the critical temperature distribution. It is convenient to remind here that the resulting ΔT_c are among the lowest reported up to now for any HTS family and that, as also shown in chapter 2, for most of the samples ΔT_c competes with merely the minimum, unavoidable intrinsic inhomogeneity expected for a fully random distribution of dopant ions. After performing SQUID measurements in our films, we have patterned over them microbridges of width 50μm and total length 4mm (details of the microbridge appearance can be seen in figure 4.1). In table 4.1 are summarized the dimensions of the microbridges for each of our samples.

Once the films were patterned by photolithography, we have deposited a ~ 300nm thick layer of silver over the contacts in order to better sold the wires that will be connected to the electrical contacts introduced in the cryostat. In order to measure the $V-I$ characteristics, the film was pasted to an intermediate Cu sample-holder with Apiezon N grease. This intermediate Cu sample-holder was connected to the electronics setup through Cu wires along the cryostat-holder (in figure 4.2 we show two photographs of these two sample holders). The in-plane resistivity was measured using the conventional four-probe technique in a Quantum Design's Physical Property Measurement System (PPMS). Resistivity measurements were carried out with a dc current of 100μA from 5K up to 250K taking data every 0.2K and without any applied magnetic field. The $V-I$ measurements involving larger currents were done in a Oxford Instruments cryostat and data were transmitted and recorded using an electronic setup composed by a Keithley-2425 pulse current source, a HP-34420A nanovoltmeter and a ITC-503 cryostat temperature controller, being this equipment controlled by a LabView program. We have also used the standard four probe method and applied to the films current pulses of ~ 1ms. This pulse duration warrants the absence of spurious self-heating effects. [147, 148] To get the $E-J$ values from our $V-I$ measurements, we simply made the corresponding

[1] Samples with $x = 0.09$ and $x = 0.10$ were damaged during our attempts of measurement, and so they are not treated in our analyses.

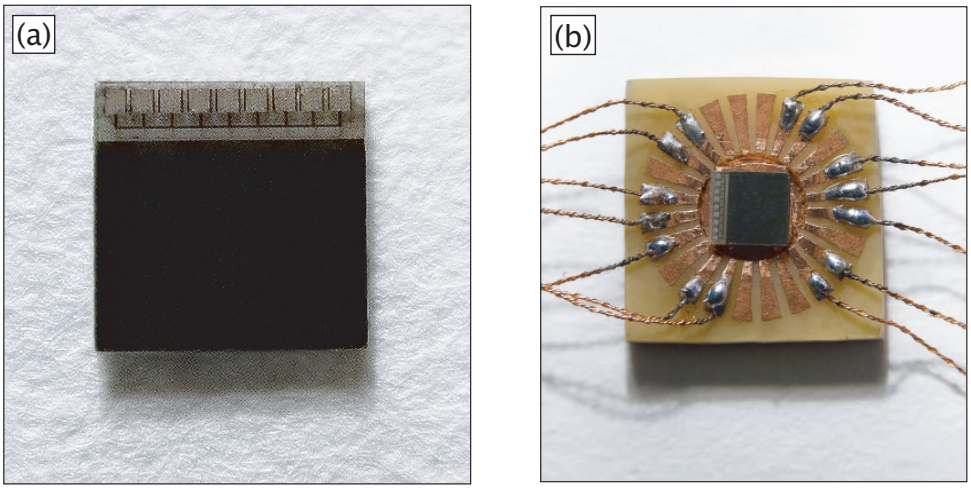

Figure 4.1: Picture (a) shows a $La_{2-x}Sr_xCuO_4$ film with the silver contacts attached. Picture (b) shows a $La_{2-x}Sr_xCuO_4$ film ready to sold to an intermediate holder to be measured at the cryostat.

sample	length (mm)	thickness (nm)	width (μm)
$LS_{0.11}CO$	3	175	50
$LS_{0.12}CO$	3	275	50
$LS_{0.13}CO$	0.5	300	50
$LS_{0.15}CO$	0.5	150	50
$LS_{0.16}CO$	0.5	275	50
$LS_{0.19}CO$	0.5	250	50
$LS_{0.22}CO$	0.5	200	50

Table 4.1: Dimensions of the microbridges under study. The length corresponds to the distance between voltage probes.

geometrical transformations $E = V/\text{length}$ and $J = I/(\text{thickness} \cdot \text{width})$.

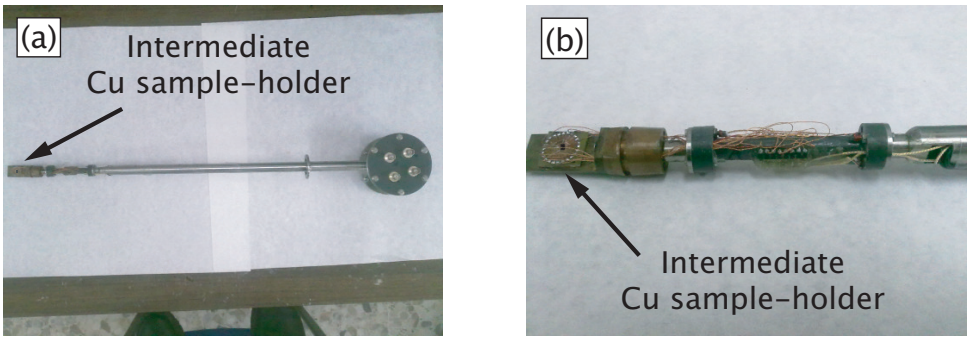

Figure 4.2: Picture (a) shows the cryostat-holder with the intermediate Cu sample-holder at the left. Picture (b) shows a zoom of the intermediate Cu sample-holder together with the Cu wires used to connect electrically the microbridge on the film and the electronics setup.

4.3 Results of our measurements

In figures 4.3 to 4.6 we show the $E-J$ characteristics and resistivity versus temperature curves, $\rho(T)$, measured in our underdoped samples ($x = 0.11$, 0.12, 0.13 and 0.15). In figure 4.7 we represent the same results for the optimally-doped sample ($x = 0.16$) and in figures 4.8 to 4.9 for the overdoped samples with $x = 0.19$ and $x = 0.22$. In all these figures, panels (a) correspond to the $E-J$ characteristics, while panels (b) correspond to the $\rho(T)$ curves.

4.3.1 Analyses to obtain $\overline{T}_{\text{phase}}$

Note that the $E-J$ characteristics are plotted in log-log scale, and therefore the slope in those plots corresponds to the exponent α in the relation $E \propto J^{\alpha}$. The insets of panels (a) of figures 4.3 to 4.9 show the evolution with temperature of α, calculated in particular by a fit to the data always in the E range between 10^{-3} and 0.1V/cm. This slope is ohmic ($\alpha = 1$) for the higher temperatures, but it abruptly departs to well larger values below the transition, the appearance of the non-ohmic feature happening in a quite narrow temperature interval. From these curves we obtain $\overline{T}_{\text{phase}}$ simply as the temperature at which $\alpha = 3$. This is a particularly unambiguous $\overline{T}_{\text{phase}}$ extraction, almost without uncertainties associated with background subtractions or inhomogeneity effects. The insets of panels (a) of figures 4.3 to 4.9 also show that when T decreases below $\overline{T}_{\text{phase}}$ the exponent α continues to increase. This is also in agreement with the predictions of HN, the precise increase rate being expected to depend on the details of the vortex pinning. [43, 136] Figure 4.10 and table 4.2 summarizes our results for $\overline{T}_{\text{phase}}$ for all of our samples.

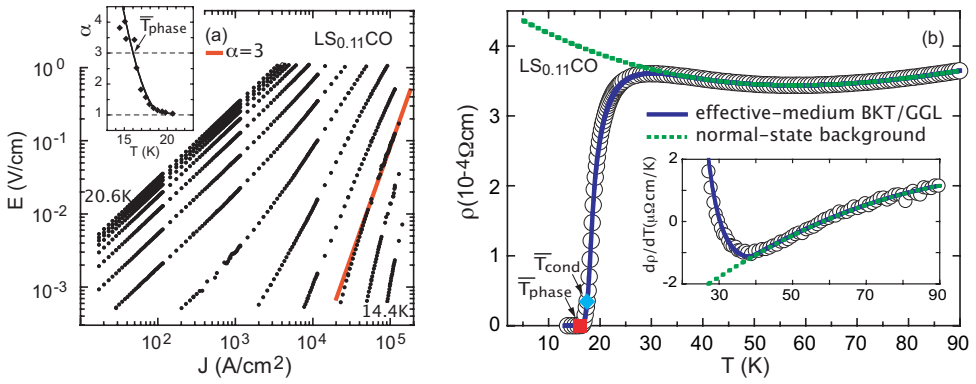

Figure 4.3: Results for the $LS_{0.11}CO$ underdoped sample. In panel (a) are represented the $E-J$ characteristics. The inset shows the corresponding α exponent obtained as the log-log slope of the $E-J$ curves in the range $10^{-3} < E < 0.1$ V/cm. Panel (b) shows the experimental $\rho(T)$ curves (open circles) together with their corresponding background (green dashed line) and BKT/GGL effective-medium theory (blue solid line). Red squares and cyan diamonds represent $\overline{T}_{\rm phase}$ and $\overline{T}_{\rm cond}$ temperatures respectively.

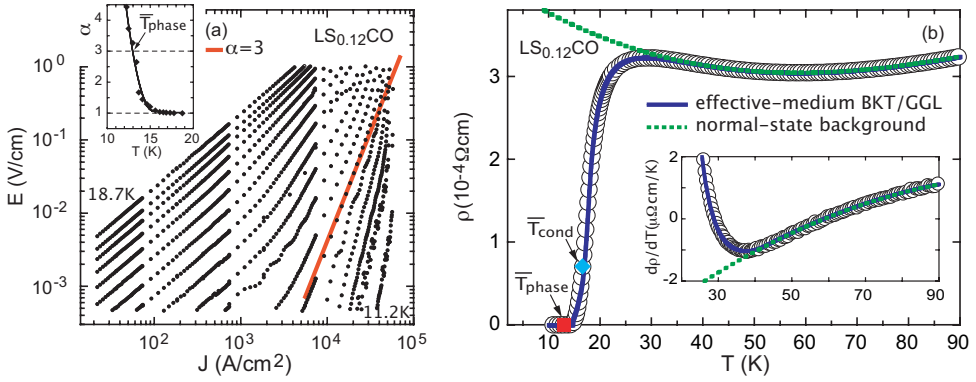

Figure 4.4: Results for the $LS_{0.12}CO$ underdoped sample. In panel (a) are represented the $E-J$ characteristics. The inset shows the corresponding α exponent obtained as the log-log slope of the $E-J$ curves in the range $10^{-3} < E < 0.1$ V/cm. Panel (b) shows the experimental $\rho(T)$ curves (open circles) together with their corresponding background (green dashed line) and BKT/GGL effective-medium theory (blue solid line). Red squares and cyan diamonds represent $\overline{T}_{\rm phase}$ and $\overline{T}_{\rm cond}$ temperatures respectively.

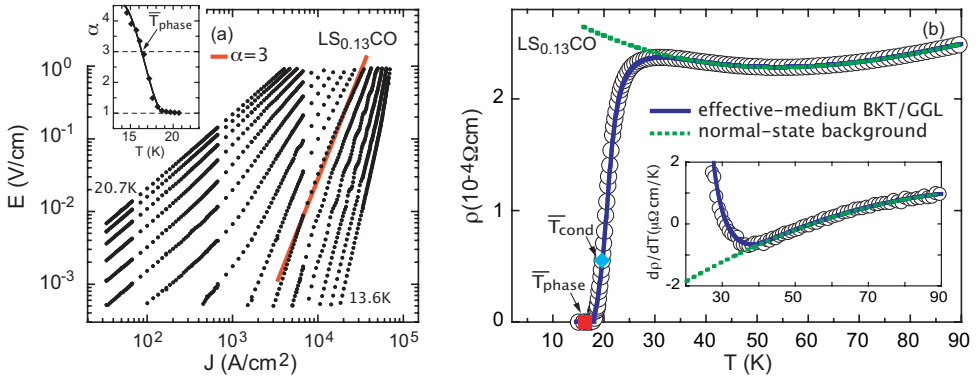

Figure 4.5: Results for the $LS_{0.13}CO$ underdoped sample. In panel (a) are represented the $E-J$ characteristics. The inset shows the corresponding α exponent obtained as the log-log slope of the $E-J$ curves in the range $10^{-3} < E < 0.1$ V/cm. Panel (b) shows the experimental $\rho(T)$ curves (open circles) together with their corresponding background (green dashed line) and BKT/GGL effective-medium theory (blue solid line). Red squares and cyan diamonds represent $\overline{T}_{\rm phase}$ and $\overline{T}_{\rm cond}$ temperatures respectively.

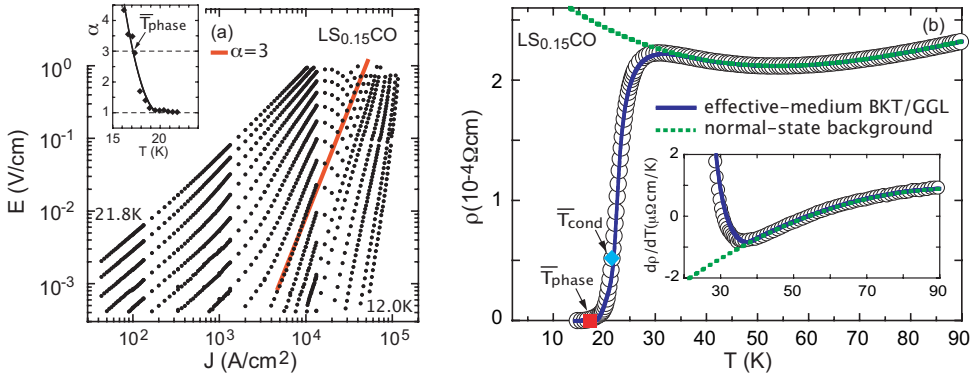

Figure 4.6: Results for the $LS_{0.15}CO$ underdoped sample. In panel (a) are represented the $E-J$ characteristics. The inset shows the corresponding α exponent obtained as the log-log slope of the $E-J$ curves in the range $10^{-3} < E < 0.1$ V/cm. Panel (b) shows the experimental $\rho(T)$ curves (open circles) together with their corresponding background (green dashed line) and BKT/GGL effective-medium theory (blue solid line). Red squares and cyan diamonds represent $\overline{T}_{\rm phase}$ and $\overline{T}_{\rm cond}$ temperatures respectively.

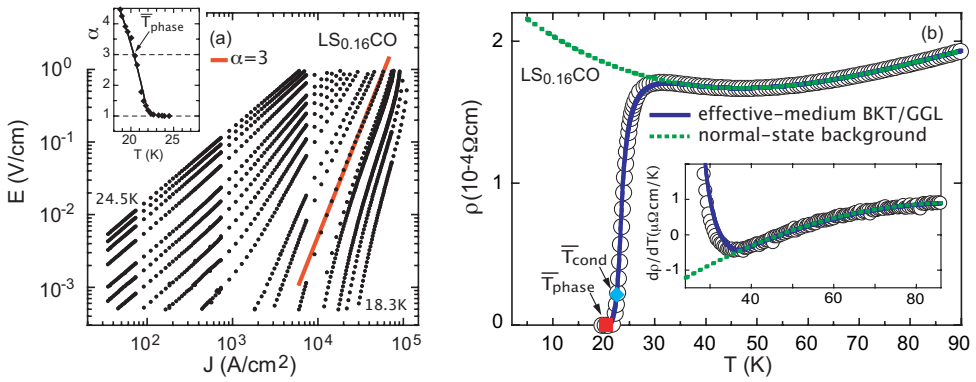

Figure 4.7: Results for the optimally-doped $LS_{0.16}CO$. Panel (a) represents the $E-J$ characteristics. The inset shows the corresponding α exponent obtained as the log-log slope of the $E-J$ curves in the range $10^{-3} < E < 0.1$ V/cm. Panel (b) shows the experimental $\rho(T)$ curve (open circles) together with its corresponding background (green dashed line) and BKT/GGL effective-medium theory (blue solid line). Red square and cyan diamond represent $\overline{T}_{\rm phase}$ and $\overline{T}_{\rm cond}$ temperatures respectively.

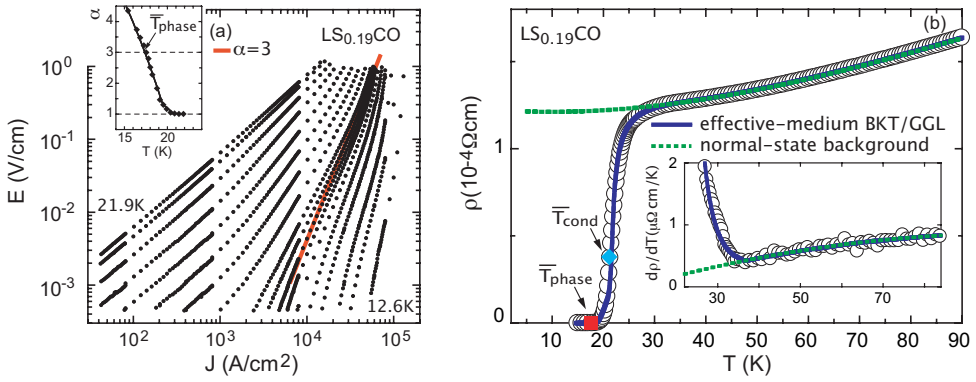

Figure 4.8: Results for the $LS_{0.19}CO$ overdoped sample. In panel (a) are represented the $E-J$ characteristics. The inset shows the corresponding α exponent obtained as the log-log slope of the $E-J$ curves in the range $10^{-3} < E < 0.1$ V/cm. Panel (b) shows the experimental $\rho(T)$ curves (open circles) together with their corresponding background (green dashed line) and BKT/GGL effective-medium theory (blue solid line). Red squares and cyan diamonds represent $\overline{T}_{\rm phase}$ and $\overline{T}_{\rm cond}$ temperatures respectively.

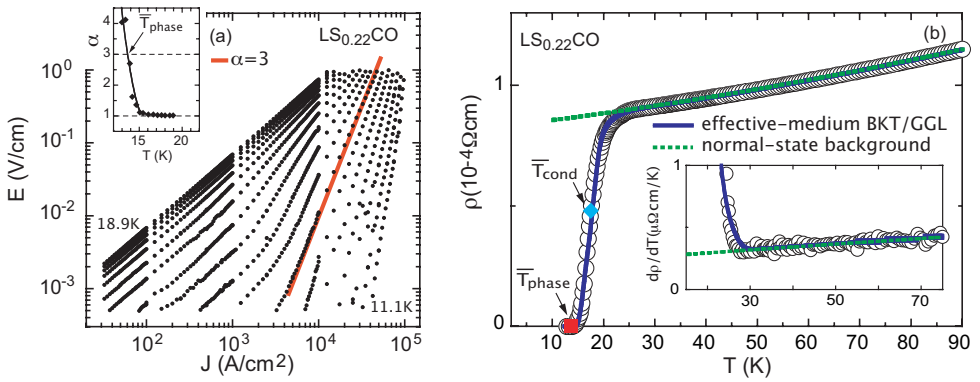

Figure 4.9: Results for the $LS_{0.22}CO$ overdoped sample. In panel (a) are represented the $E-J$ characteristics. The inset shows the corresponding α exponent obtained as the log-log slope of the $E-J$ curves in the range $10^{-3} < E < 0.1$ V/cm. Panel (b) shows the experimental $\rho(T)$ curves (open circles) together with their corresponding background (green dashed line) and BKT/GGL effective-medium theory (blue solid line). Red squares and cyan diamonds represent $\overline{T}_{\rm phase}$ and $\overline{T}_{\rm cond}$ temperatures respectively.

4.3.2 Analyses to obtain $\overline{T}_{\rm cond}$

Panels (b) of figures 4.3 to 4.9 show the $\rho(T)$ curves measured with small current densities, $J \sim 10^3 \mathrm{A/cm^2}$, in the same films as for panels (a). Note that $\overline{T}_{\rm phase}$ (marked as a red solid square in panels (b)) corresponds to the tail of the resistive decay. Above it, the transition to the normal state is spread over an easily accessible temperature range.

A quantity commonly used to study the fluctuation roundings in the resistivity is the so-called paraconductivity, $\Delta\sigma \equiv \rho^{-1} - \rho_n^{-1}$, where ρ_n is the normal-state background (i.e., the resistivity in absence of superconductivity). To obtain the ρ_n, most studies of $\Delta\sigma$ in HTS had to deal with the uncertainty of what is the temperature well above the transition above which the normal-state behaviour can be fitted.(see, *e.g.*, [64]) In the present case, however, our data present a change in slope at a well-defined temperature, T^{C}, well above the transition. This is clearly visible in the insets of panels (b) of figures 4.3 to 4.9, in which $\mathrm{d}\rho/\mathrm{d}T$ is plotted and T^{C} marks a strong change in the behaviour of this derivative. It seems then reasonable to assume that T^{C} signals the appearance of the first visible deviations of the pure normal-state behaviour. Therefore, we obtain ρ_n by means of a fit to the $\rho(T)$ and $\mathrm{d}\rho/\mathrm{d}T$ data above that temperature, in the range $T^{\mathsf{C}} < T < T^{\mathsf{C}} + 50\mathrm{K}$ using for all dopings a two-step procedure: First, we fit the $\mathrm{d}\rho/\mathrm{d}T$ data to a parabolic law between $T^{\mathsf{C}} < T < T^{\mathsf{C}} + 50\mathrm{K}$ and obtain as free parameters the three coefficients of such fitting. Second, and using the values obtained before, we fit the $\rho(T)$ data to the primitive function of the $\mathrm{d}\rho/\mathrm{d}T$ parabola, having now only one free parameter in our fitting (*i.e.*, the independent coefficient). The resulting background is

shown as green dashed lines in panels (b) of figures 4.3 to 4.9 and in their insets.

To analyze the corresponding $\Delta\sigma$, we will use expressions that take into account the different regimes of superconducting fluctuations expected to occur for any type-II 2D superconductor above $T_{\rm phase}$:

i) Immediately above $T_{\rm phase}$ (in the often-called strong phase fluctuation or full-critical regime) the relevant excitations are topological (vortex and antivortex positions) and they may be well described by the renormalization group approaches. In that regime, as shown by BKT the coherence length ξ depends exponentially on $(b_0\Delta_{\rm BKT}/(T-T_{\rm phase}))^{1/2}$, where $\Delta_{\rm BKT}=T_{\rm cond}-T_{\rm phase}$ is the BKT displacement and b_0 a constant of the order of unity. As first predicted by HN [43], by using the Josephson relation it follows a fluctuation conductivity $\Delta\sigma_{\rm BKT}\propto n_f^{-1}\propto\xi^2$, where n_f is the planar density of free vortices, and hence [43]

$$\Delta\sigma_{\rm BKT}=A_{\rm BKT}\exp\sqrt{\frac{4b_0\Delta_{\rm BKT}}{T-T_{\rm phase}}}. \tag{4.1}$$

Here $A_{\rm BKT}$ is a constant that may be directly obtained by continuity of $\Delta\sigma_{\rm BKT}$ with the results of the following temperature regime *ii*).

ii) Sufficiently above $T_{\rm cond}$, topological excitations are no longer dominant, and the superconducting fluctuations must become mean-field-like and well described as Gaussian perturbations over the Ginzburg-Landau minimum free energy solutions, usually called the GGL approach (see section 1.2). In this regime, often also known as the amplitude fluctuation regime, $\xi\propto\varepsilon^{-1/2}$ with ε being the reduced-temperature $\varepsilon\equiv\ln(T/T_{\rm cond})$ ($\simeq 1-T/T_{\rm cond}$ for small ε). According to the classical calculations by Aslamazov and Larkin (AL) the fluctuation conductivity is then $(e^2/16\hbar d)\varepsilon^{-1}$. However, the latter result is not expected to remain valid in the high reduced-temperature region $\varepsilon\gtrsim 0.1$, as it does not take into account short-wavelength fluctuations associated to the smallness of ξ as ε increases. Full expressions accounting for the short-wavelength effects were calculated in [89] on the grounds of a total-energy cutoff approach (developing the ideas first sketched by Patton in [83] for the fluctuation diamagnetism). These calculations lead to

$$\Delta\sigma_{\rm GGL}=\frac{e^2}{16\hbar d\varepsilon}\left(1-\frac{\varepsilon}{\varepsilon^c}\right)^2. \tag{4.2}$$

In this expression, ε^c is a cutoff reduced temperature at which fluctuations experience a rapid fall, so that for $\varepsilon>\varepsilon^c$ they effectively become null. As shown in [85, 86], this ultimately reflects the fact that for such temperatures ξ is already below its $T=0$K value and hence superconducting excitations would be constrained to spaces smaller than what the uncertainty principle allows (as it is the latter what determines ξ at $T=0$K). In our case, it is natural to take $\varepsilon^c=\ln(T^{\sf C}/\overline{T}_{\rm cond})$ with $T^{\sf C}$ the temperature at which deviations from the normal state behaviour are seen in the $\rho(T)$ and $\mathrm{d}\rho/\mathrm{d}T$ plots (see, however, our appendix 4.6).

Calculating the precise location, $T_{\rm LG}$, of the boundary between the temperature regions *i*) and *ii*) is a still open theoretical problem. However, the Levanyuk-Ginzburg

criterion for the breakdown of the Gaussian hypothesis of the GGL approach could be taken as a first crude approximation for that boundary. [71] This predicts for layered superconductors in the 2D limit a GGL breakdown above $T_{\rm cond}$ at the temperature $T_{\rm cond}\exp(\varepsilon_{\rm LG}) \simeq T_{\rm cond}(1+\varepsilon_{\rm LG})$, with $\varepsilon_{\rm LG} = k_{\rm B}/(4\pi\xi_{\rm ab}(0)s\Delta C)$, being $k_{\rm B}$ the Boltzmann constant, $\xi_{\rm ab}(0)$ the in-plane coherence length, s the distance between adjacent superconducting CuO_2 planes and ΔC the mean-field jump of the heat capacity. Previous analyses of the superconducting fluctuations in HTS above $T_{\rm cond}$ suggest that $\varepsilon_{\rm LG} \simeq 10^{-2}$. [16]

When trying to study in terms of the above predictions the $\rho(T)$ rounding in actual superconductors, it is important to take inhomogeneities into account, particularly when analyzing the data so close to the transition as in the present work. For that, we will use our independent $\Delta T_{\rm c}$ measurements (see chapter 2) and the effective-medium approximation [127, 145] for a material with resistive inhomogeneities uniformly distributed in space already presented in equation (3.5). Now $\sigma = 1/\rho$ is the global conductivity of the sample, $\sigma_{T_{\rm c}'}$ is the conductivity of a domain with single values of the condensation temperature $T_{\rm cond} = T_{\rm c}'$, $T_{\rm phase} = T_{\rm c}' - \Delta_{\rm BKT}$ ($\Delta_{\rm BKT}$ being considered constant all trough the superconductor) and $\overline{T}_{\rm cond}$ is the average condensation temperature.

In panels (b) of figures 4.3 to 4.9 we show, as blue continuous lines, the fits to our $\rho(T)$ data using the $\rho_n(T)$ and $\Delta\sigma$ described above. The insets show also the agreement with $\mathrm{d}\rho/\mathrm{d}T$. In each of those fits the only fully free parameter is $\overline{T}_{\rm cond}$ (marked as a solid cyan diamond in the figures). The rest of parameters are constrained as follows: For $\overline{T}_{\rm phase}$, we use the results from the $\alpha = 3$ condition; for $\Delta T_{\rm c}$, we use the values determined from magnetometry in chapter 2; for ε^{C} we use $\varepsilon^{\mathsf{C}} = \ln(T^{\mathsf{C}}/\overline{T}_{\rm cond})$; $\varepsilon_{\rm LG}$ is constrained as $0.5\times10^{-2} \lesssim \varepsilon_{\rm LG} \lesssim 2\times10^{-2}$; and for b_0 we impose that the seven fits corresponding to the studied dopings share a common value, which for our analyses is $b_0 = 4$. The obtained agreement with the data is excellent for all the temperatures from above $T_{\rm phase} + 1$K up to T^{C}. The temperature $T_{\rm phase} + 1$K roughly corresponds, for all dopings, to the beginning of the non-ohmic regime ($\alpha = 1.5$). As shown in chapter 3, this condition is actually expected to mark the appearance of percolating-like current paths breaking the effective-medium approximation, in agreement with our present results.

4.4 Results for the $La_{2-x}Sr_xCuO_4$ phase diagram

Finally, we plot in figure 4.10 the $\overline{T}_{\rm cond}(x)$ and $\overline{T}_{\rm phase}(x)$ obtained in this work. It is evident that both result in similar domes, displaced only about 4K from each other. Figure 4.10 also shows (dotted cyan line) a fit to the $\overline{T}_{\rm cond}(x)$ dome using the conventional parabolic law ${T_{\rm cond}}^{x=0.16}\left[1-((x-0.16)/0.11)^2\right]$ [123] plus a concave downward Gaussian peak for the depression near $x = 1/8$, $-\delta T_{c1/8}\exp[-((x-1/8)/0.01)^2]$ (see chapter 2). We obtain $\delta T_{c1/8} = 3.1$K. This figure also shows as a red dashed line the same fit results minus a constant displacement $\overline{\Delta}_{\rm BKT} = 3.3$K. Moreover, we summarize in table 4.2 the main parameters obtained in our analyses.

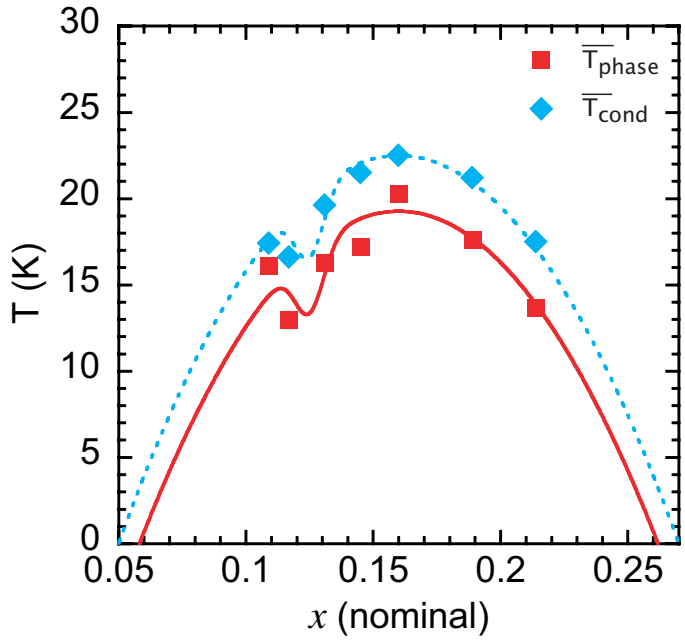

Figure 4.10: Resulting phase diagram for $\overline{T}_{\rm phase}$ (red squares) and $\overline{T}_{\rm cond}$ (cyan diamonds) of our $La_{2-x}Sr_xCuO_4$ thin films. Both red solid and cyan dashed lines are fits to $\overline{T}_{\rm phase}$ and $\overline{T}_{\rm cond}$ data respectively. See main text for details on the construction of these fits.

4.5 Conclusions

In this chapter, we have completed our study by performing resistivity and $V-I$ measurements in the films synthesized by us with dopings $0.11 < x < 0.22$. From these measurements we derive $T_{\rm phase}(x)$ and $T_{\rm cond}(x)$ phase diagrams, in which $T_{\rm phase}$ is obtained through the $\alpha = 3$ condition and $T_{\rm cond}$ through the comparison with our effective-medium fluctuation approach. The so-resulting $T_{\rm cond}(x)$ and $T_{\rm phase}(x)$ lines are parabolas (with a slight depression near $x = 1/8$) that for all dopings are not further away than $\sim$ 4K from the $T_{\rm c}(x)$ line in which the macroscopic superconducting phenomenology (*e.g.*, the full Meissner effect) appears. These small differences between $T_{\rm cond}$, $T_{\rm phase}$ and $T_{\rm c}$ for the underdoped, optimally-doped and overdoped samples suggest theoretical scenarios different from the strong phase-fluctuation pairing models, [3, 20–22] in which $T_{\rm c}$ is primarily determined by the vortex-antivortex binding instead of the pairing between single-particle normal carriers (*i.e.*, $T_{\rm cond} \gg T_{\rm phase}$ and $T_{\rm phase} \simeq T_{\rm c}$). Our results are coherent instead with pairing models in which both $T_{\rm cond} - T_{\rm phase}$ and $T_{\rm cond} - T_{\rm c}$ are small ($\lesssim$ 5K) for all dopings. [5, 30, 48, 49, 51–58].

sample	$\overline{T}_{\rm phase}$ (K)	$\overline{T}_{\rm cond}$ (K)	T^{c} (K)	$\Delta T_{\rm c}$ (K)	ε^{c}	ε_{LG}	b_0
$LS_{0.11}CO$	16.1	17.4	40.0	1.1	0.8	0.010	4
$LS_{0.12}CO$	13.0	16.6	40.0	1.4	0.9	0.015	4
$LS_{0.13}CO$	16.3	19.6	40.0	2.3	0.7	0.020	4
$LS_{0.15}CO$	17.2	21.5	38.0	1.2	0.5	0.010	4
$LS_{0.16}CO$	20.3	22.5	38.0	1.3	0.5	0.005	4
$LS_{0.19}CO$	17.6	21.2	36.0	0.7	0.5	0.005	4
$LS_{0.22}CO$	13.7	17.5	28.0	1.6	0.5	0.020	4

Table 4.2: Main parameters resulting from our analyses for all the samples.

4.6 Appendix: Analyses of $\rho(T)$ using for ε^{c} the BCS value

In our analyses in section 4.3.2, we have employed the condition $\varepsilon^c = \ln(T^{\mathsf{c}}/\overline{T}_{\rm cond})$, based on the fact that superconducting fluctuations are theoretically expected to vanish above ε^c in an homogeneous superconductor. This is consistent with the interpretation in the extended GGL approach of ε^{c} as the reduced-temperature above which fluctuations disappear in an homogeneous sample. This led to ε^{c} in the range $0.5 \leq \varepsilon^{\mathsf{c}} \leq 0.9$. These values are close to the theoretical prediction $\varepsilon^{\mathsf{c}} = 0.55$ obtained in [85] using the BCS approach in the clean limit (see section 1.2.3 for the details of the obtainment of the $\varepsilon^{\mathsf{c}} = 0.55$ prediction). However, it may be asked what reasons may exist for the ε^{c} variability. Let us show here that our data are in fact compatible with fits imposing $\varepsilon^{\mathsf{c}} = 0.55$ if we consider for the inhomogeneities the possibility of $T_{\rm c}$ distributions with slight asymmetry (instead of the simple and symmetrical Gaussian $T_{\rm c}$ distributions used in our figures 4.3 to 4.9). The probed asymmetry takes the form of an additional upper tail comprising just about between 2% and 4.5% of the sample, and is too small to be resolved in our SQUID measurements of the $T_{\rm c}$ distributions. We will also show that this ε^{c} uncertainty does not affect the values of $\overline{T}_{\rm phase}$ or $\overline{T}_{\rm cond}$ obtained in our analyses.

Figure 4.11(a) shows a comparison of two $T_{\rm c}$ distributions being probed for the film with $x = 0.11$. The first (blue dashed line) is a symmetrical Gaussian peak. For the second (red continuous line) we added to the first an additional small tail towards higher $T_{\rm c}$'s. In both distributions the main part of the peak is centered at $\overline{T}_{\rm cond} = 17.4$K and has a FWHM of $\Delta T_{\rm c} = 1.1$K (as we have already said, they correspond to $La_{1.89}Sr_{0.11}CuO_4$). To construct the upper tail we added for $T_{\rm cond} > \overline{T}_{\rm cond}$ a second Gaussian peak centered again at $\overline{T}_{\rm cond}$ but with much smaller amplitude ($\sim 1/10$ of the main peak) and much

wider. The differences between both distributions occur almost exclusively for $T_{\rm cond} > \overline{T}_{\rm cond} + \Delta T_{\rm c}$ and the area between both distributions within this region (the grey shaded area in figure 4.11(a)) accounts for only a 4% of the superconductor. At first sight both distributions are indistinguishable but we can see the differences by making a zoom (inset of figure 4.11(a)).

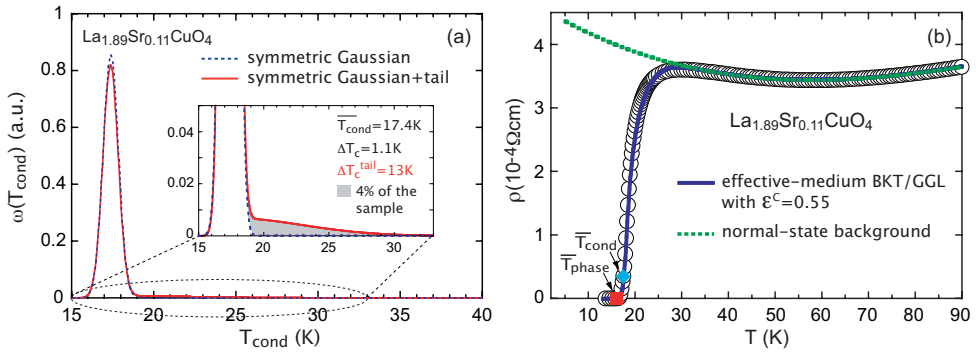

Figure 4.11: (a) Comparison between two $T_{\rm c}$'s distributions for $La_{1.89}Sr_{0.11}CuO_4$: blue dashed line corresponds to a symmetrical Gaussian distribution with mean value $\overline{T}_{\rm cond}$=17.4K and $\Delta T_{\rm c}$=1.1K. Red continuous line corresponds to the same distribution plus an asymmetrical distribution with an upper tail added towards higher $T_{\rm c}$'s (with $\overline{T}_{\rm cond}$=17.4 and $\Delta T_{\rm c}$=13K). (b) Results of the analysis for the clean limit value (ε^{C}=0.55) using the new distribution of $T_{\rm c}$'s obtained in (a).

Figure 4.11(b) shows our $\rho(T)$ data for $La_{1.89}Sr_{0.11}CuO_4$ and their fit by the same effective-medium BKT-GGL approach as in the main text, but now employing $\varepsilon^{\mathsf{C}} = 0.55$ and the $T_{\rm c}$ distribution with the upper asymmetric tail of figure 4.11(a). The agreement with the data is excellent, at the same level as in figure 4.3(b) (that uses $\varepsilon^{\mathsf{C}} = 0.8$ and the Gaussian distribution without the enlarged upper tail). Importantly, both fits produce the same values for $\overline{T}_{\rm cond}$. They also use the same $\overline{T}_{\rm phase}$, b_0, $\varepsilon_{\rm LG}$ and background. Therefore, the uncertainty in the precise value of ε^{C} does not affect the main conclusions of our analysis, that concern the location of $\overline{T}_{\rm cond}$ and $\overline{T}_{\rm phase}$. This is coherent with the fact that ε^{C} actually only influences the fit well above both temperatures. We have checked that the same is valid also for the rest of our films that produced fits with $\varepsilon^{\mathsf{C}} > 0.55$ in our main analysis, *i.e.*, for films with x =0.12 and 0.13 (results can be seen in figures 4.12 and 4.13).

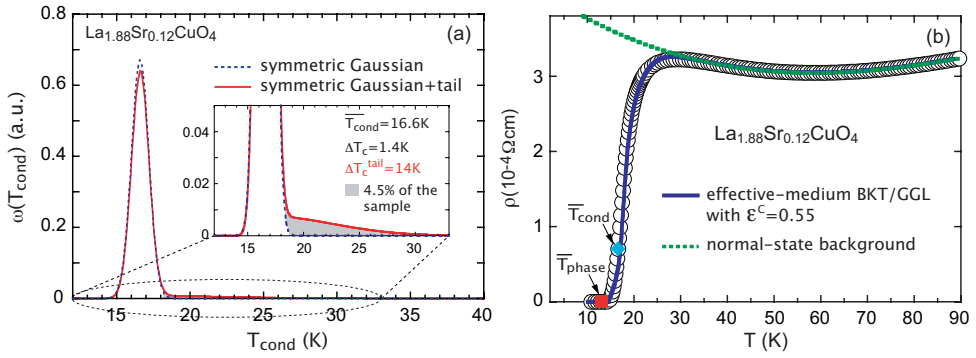

Figure 4.12: (a) Comparison between two T_c's distributions for $La_{1.88}Sr_{0.12}CuO_4$: blue dashed line corresponds to a symmetrical Gaussian distribution with mean value $\overline{T}_{\rm cond}$=16.6K and ΔT_c=1.4K. Red continuous line corresponds to the same distribution plus an asymmetrical distribution with an upper tail added towards higher T_c's (with $\overline{T}_{\rm cond}$=16.6 and ΔT_c=14K). (b) Results of the analysis for the clean limit value (ε^C=0.55) using the new distribution of T_c's obtained in (a).

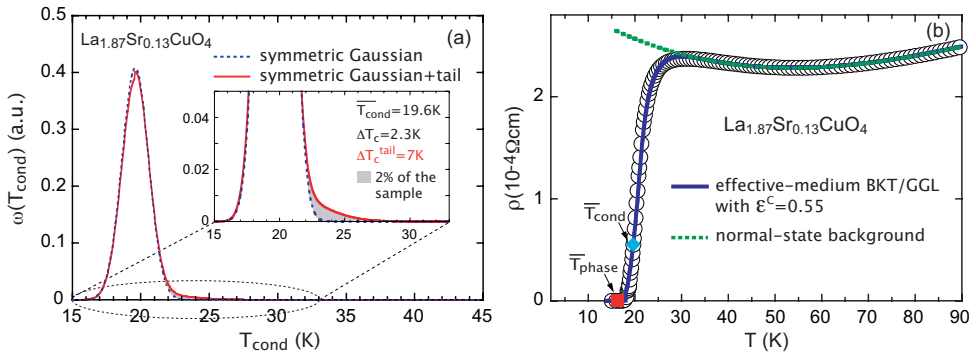

Figure 4.13: (a) Comparison between two T_c's distributions for $La_{1.87}Sr_{0.13}CuO_4$: blue dashed line corresponds to a symmetrical Gaussian distribution with mean value $\overline{T}_{\rm cond}$=19.6K and ΔT_c=2.3K. Red continuous line corresponds to the same distribution plus an asymmetrical distribution with an upper tail added towards higher T_c's (with $\overline{T}_{\rm cond}$=19.6 and ΔT_c=7K). (b) Results of the analysis for the clean limit value (ε^C=0.55) using the new distribution of T_c's obtained in (a).

USC
UNIVERSIDADE
DE SANTIAGO
DE COMPOSTELA

USC
UNIVERSIDADE
DE SANTIAGO
DE COMPOSTELA

Final conclusions

In this thesis we have proposed an unambiguous answer to a central and until now debated question of the phenomenological descriptions of the superconducting transition in cuprates, a question already stated in our Introductory chapter: Where are located the temperatures of superconducting phase coherence, $T_{\rm phase}$, and superconducting pair condensation, $T_{\rm cond}$? Our results strongly indicate that they are situated close to each other, with $T_{\rm cond} - T_{\rm phase} \lesssim 4$K, suggesting then a conventional superconducting fluctuations scenario. This conclusion contrast with the, at present, most popular scenario of strong phase fluctuations where the distance between $T_{\rm phase}$ and $T_{\rm cond}$ is of the order of tens or even hundreds of Kelvin. [3, 20–28]

For this purpose, we have developed a pulsed laser deposition technique able to grow, over substrates of (100)$SrTiO_3$, thin films of $La_{2-x}Sr_xCuO_4$ with various dopings levels x from two separate parent targets of $La_{1.1}Cu_{0.9}O_{2.4}$ and $SrCuO_2$, instead of one single target with a specific composition determining the final composition of the film. To our knowledge, this is the first time that this procedure is applied to vary systematically the doping of any single material HTS: By varying the number of laser shots over the surface of the $La_{1.1}Cu_{0.9}O_{2.4}$ target with respect to the $SrCuO_2$ target, we have obtained various films with different doping compositions ($0.09 \lesssim x \lesssim 0.22$). Our samples have homogeneities similar to the best reported in the literature, as determined from high-precision magnetometry SQUID measurements. We have also shown that the x-dependence of the critical temperature dispersions obtained in such measurements, $\Delta T_{\rm c}(x)$, can be explained in terms of the unavoidable randomness of the positioning of the Sr ions (the so-called intrinsic chemical inhomogeneity) between the CuO_2 planes of the crystal lattice of $La_{2-x}Sr_xCuO_4$, and a separate residual $T_{\rm c}$-inhomogeneity contribution of the order of 0.5K (associated with the structural inhomogeneities of the samples and their substrates). This chemical disorder is compatible with $T_{\rm c}$ domains of effective in-plane radius ~ 80 CuO_2 unit cells.

We have also calculated the electrical behaviour near the BKT vortex-antivortex transition of planar superconductors with critical temperature inhomogeneities through two different methods: In the first one, we have implemented several simulations in which the superconducting inhomogeneities had larger characteristics lengths than the in-plane superconducting coherence length and were supposed to be randomly located in space. For such a purpose, we have analyzed numerically, in terms of finite-element computations,

how the voltage-current ($V-I$) characteristics near the BKT superconducting transition were affected by a Gaussian distribution of critical temperature inhomogeneities. Our samples under study were modeled as a $N \times N$ square mesh of resistors (with $N = 10$) with each node having a different mean field temperature $T_{\rm cond}$ and a different phase coherence temperature $T_{\rm phase}$, taken from Gaussian distributions with mean values $\overline{T}_{\rm cond}$ and $\overline{T}_{\rm phase}$ respectively, and with dispersion $\Delta T_{\rm c}$. These calculations focus on the exponent α in $V \propto I^{\alpha}$ and the resistance V/I. They show that the sharp jump in the exponent α from ohmic behaviour to the value $\alpha = 3$ provides a good estimate of the location of $\overline{T}_{\rm phase}$. They also reveal that strong redistributions of the local current and map voltages occur around $\overline{T}_{\rm phase}$, when approximately 50% of the sample has experienced the vortex-antivortex binding transition. The simulations have also allowed us to quantify the broadening of the transition due to inhomogeneities in both the exponent α and the resistance V/I, manifesting that the inhomogeneities are detectable over a larger T-range on V/I than on the exponent α. In addition, we have implemented effective-medium calculations. We have obtained that the effective-medium results agree well with the finite-element ones except for the region close to $\overline{T}_{\rm phase}$, where the percolation-like current redistributions appear.

We have completed our study by performing resistivity and $V-I$ measurements in the films synthesized by us with dopings $0.11 \lesssim x \lesssim 0.22$. From these measurements we derive $T_{\rm phase}(x)$ and $T_{\rm cond}(x)$ phase diagrams, in which $T_{\rm phase}$ is obtained through the $\alpha = 3$ condition and $T_{\rm cond}$ through the comparison with our effective-medium fluctuation approach. The so-resulting $T_{\rm cond}(x)$ and $T_{\rm phase}(x)$ lines are parabolas (with a slight depression near $x = 1/8$) that for all dopings are not further away than ~ 4K from the $T_{\rm c}(x)$ line in which the macroscopic superconducting phenomenology (*e.g.*, the full Meissner effect) appears. These small differences between $T_{\rm cond}$, $T_{\rm phase}$ and $T_{\rm c}$ for the underdoped, optimally-doped and overdoped samples suggest theoretical scenarios different from the strong phase-fluctuation pairing models, [3, 20–22] in which $T_{\rm c}$ is primarily determined by the vortex-antivortex binding instead of the pairing between single-particle normal carriers (*i.e.*, $T_{\rm cond} \gg T_{\rm phase}$ and $T_{\rm phase} \simeq T_{\rm c}$). Our results are coherent instead with pairing models in which both $T_{\rm cond} - T_{\rm phase}$ and $T_{\rm cond} - T_{\rm c}$ are small ($\lesssim 5$K) for all dopings. [5, 30, 48, 49, 51–58].

USC
UNIVERSIDADE
DE SANTIAGO
DE COMPOSTELA

USC
UNIVERSIDADE
DE SANTIAGO
DE COMPOSTELA

Bibliography

[1] For a review of the importance of understanding the superconducting transition in HTS (and in particular the location of the superconducting condensation and phase coherence temperatures) in connection with the search of the pairing mechanism in these materials see, *e.g.*, M. Franz, *Nature Physics* **3**, 686 (2007). See also [2–8].

[2] M.R. Norman, D. Pines and C. Kallin, *Adv. Phys.* **54**, 715 (2005).

[3] V.J. Emery and S.A. Kivelson, *Nature* **374**, 434 (1995).

[4] For a review of the current state of the theories of pairing in HTS see, *e.g.*, vol. **2** of *Nature Physics* (march 2006), in particular its editorial commentaries (pp. 133 and 138-143) and Refs. [5, 6]. See also Refs. [7, 8].

[5] A.J. Leggett, *Nature Physics* **2**, 134 (2006).

[6] D.A. Bonn, *Nature Physics* **2**, 159 (2006).

[7] V.Z. Kresin and S.A. Wolf, *Rev. Mod. Phys.* **81**, 481 (2009).

[8] D.J. Scalapino, *Rev. Mod. Phys.* **84**, 1383 (2012).

[9] For a review of some previous studies of the superconducting transition in HTS see, *e.g.*, F. Vidal and M.V. Ramallo, in *The Gap Symmetry and Fluctuations in High-T_c Superconductors*, vol 371, edited by J. Bok, G. Deutscher, D. Pavuna and S.A. Wolf (New York: Nato Advanced Science Institutes Series), p 443, 1998. See also [10, 11]

[10] M. Tinkham, *Introduction to Superconductivity*, chapters 8 and 9, 2nd edition McGraw-Hill, New York, 1996.

[11] J.R. Waldram, *Superconductivity of Metals and Cuprates*, chapter 5, IOP Publishing, Bristol, 1996.

[12] K. Maki and R.S. Thompson, *Phys. Rev. B* **39**, 2767 (1989).

[13] R.A. Klemm, *Phys Rev. B* **41**, 2073 (1990).

[14] C. Torrón, A. Díaz, A. Pomar, J.A. Veira and F. Vidal, *Phys Rev. B* **49**, 13143 (1994).

[15] M.V. Ramallo, A. Pomar and F. Vidal, *Phys. Rev. B* **54** 4341 (1996).

[16] M.V. Ramallo and F. Vidal, *Phys. Rev. B* **59**, 4475 (1999).

[17] S.K. Yip, *J. Low Temp. Phys.* **81**, 129 (1990); *Phys. Rev. B* **41**, 2612 (1990).

[18] M.T. Béal-Monod and O.T. valls, *Europhys. Lett.* **30**, 415 (1995); K. Maki and M.T. Béal-Monod, *Phys. Lett. A* **208**, 365 (1995); K. Maki and M.T. Béal-Monod *Europhys. Lett.* **33**, 309 (1996).

[19] M.V. Ramallo, C. Carballeira, J. Viña, J.A. Veira, T. Mishonov, D. Pavuna and F. Vidal, *Europhys. Lett.* **48**, 79 (1999).

[20] S.A. Kivelson and E.H. Fradkin, *Physics* **3**, 15 (2010).

[21] P.W. Anderson, *Nature Physics* **3**, 160 (2007).

[22] P.W. Anderson, *Phys. Rev. Lett.* **100**, 215301 (2008).

[23] A. Lascialfari, A. Rigamonti, L. Romanò, P. Tedesco, A. Varlamov and D. Embriaco, *Phys. Rev. B* **65**, 144523 (2002).

[24] E. Bernardi, A. Lascialfari, A. Rigamonti, L. Romanò, M. Scavini and C. Oliva, *Phys. Rev. B* **81**, 064502 (2010).

[25] Z.A Xu, N.P. Ong, Y. Wang, T. Kateshita and S. Uchida, *Nature* **406**, 486 (2000).

[26] Y. Li, V. Balédent, N. Barišić, Y. Cho, B. Fauqué, Y. Sidis, G. Yu, X. Zhao, P. Bourges and M. Greven, *Nature* **455**, 372 (2008).

[27] L. Li, Y. Wang, S. Komiya, S. Ono, Y. Ando, G.D. Gu and N.P. Ong, *Phys. Rev. B* **81**, 054510 (2010).

[28] Y. Li, V. Balédent, G. Yu, N. Barišić, K. Hradil, R.A. Mole, Y. Sidis, P. Steffens, X. Zhao, P. Bourges and M. Greven, *Nature* **468**, 283 (2010).

[29] P.M.C. Rourke, I. Mouzopoulou, X. Xu, C. Panagopoulos, Y. Wang, B.Vignolle, C. Proust, E.V. Kurganova, U. Zeitler, Y. Tanabe, T. Adachi, Y. Koike and N. Hussey, *Nature* **7** 455 (2011).

[30] O. Cyr-Choiniere, R. Daou, F. Laliberté, D. LeBoeuf, N. Doiron-Leyraud, J. Chang, J.Q. Yan, J.G. Cheng, J.S. Zhou, J.B. Goodenough, S. Pyon, T. Takayama, H. Takagi, Y. Tanaka and L. Teillefer, *Nature* **458**, 743 (2009).

[31] I. Ussishkin, S.L. Sondhi and D.A. Huse, *Phys. Rev. Lett.* **89**, 287001 (2002).

[32] F. Rullier-Albenque, R. Tourbot, H. Alloul, P. Lejay, D. Colson and A. Forget, *Phys. Rev. Lett.* **96**, 067002 (2006).

[33] M.V. Ramallo, C. Carballeira, R.I. Rey, J. Mosqueira and F. Vidal, *Phys. Rev. B* **85**, 106501 (2012).

[34] J. Mosqueira, L. Cabo and F. Vidal, *Phys. Rev. B* **80** 214527 (2009).

[35] J. Mosqueira, J.D. Dancausa and F. Vidal, *Phys. Rev. B* **84** 174518 (2011).

[36] R.I. Rey, A. Ramos-Álvarez, J. Mosqueira, M.V. Ramallo and F. Vidal, *Phys. Rev. B* **87**, 056501 (2013).

[37] K. Epstein, A.M. Goldman and A.M. Kadin, *Phys. Rev. Lett.* **47** 534 (1981).

[38] D.J. Resnick, J.C. Garland, J.T. Boyd, S. Shoemaker and R.S. Newrock, *Phys. Rev. Lett.* **47** 1542 (1981).

[39] D.A. Abraham, C.J. Lobb, M. Tinkham and T.M. Klapwijk, *Phys. Rev. B* **26** 5268 (1982).

[40] A. M. Kadin, K. Epstein and A.M. Goldman, *Phys. Rev. B* **27** 6691 (1983).

[41] N. Reyren, S. Thiel, A.D. Caviglia, L. Fitting Kourkoutis, G. Hammerl, C. Richter, C.W. Schneider, T. Kopp, A.S. Rüetschi, D. Jaccard, M. Gabay, D.A. Muller, J.M. Triscone and J. Mannhart, *Science* **317** 1196 (2007).

[42] A.D. Caviglia, S. Gariglio, N. Reyren, D. Jaccard, T. Schneider, M. Gabay, S. Thiel, G. Hammerl, J. Mannhart and J.M. Triscone, *Nature* **456** 624 (2008).

[43] B.I. Halperin and D.R. Nelson, *J. Low Temp. Phys.* **36** 599 (1979).

[44] V.L. Berezinskii, *Sov. Phys. JETP* **32** 493 (1971).

[45] J.M. Kosterlitz and D.J. Thouless, *J. Phys. C* **6** 1181(1973).

[46] M.R. Beasley, J.E. Mooij and T.P. Orlando, *Phys. Rev. Lett.* **42** 1165 (1979).

[47] S. Doniach and B.A. Huberman, *Phys. Rev. Lett.* **42** 1169 (1979).

[48] A.J. Leggett, *Phys. Rev. Lett.* **83**, 392 (1999).

[49] S. Chakravarty, R.B. Laughlin, D.K. Morr and C. Nayak, *Phys. Rev. B* **63**, 094503 (2001).

[50] C. Zhang, S. Tewari and S. Chakravarty, *Phys. Rev. B* **81**, 104517 (2010).

[51] C.M. Varma, *Phys. Rev. B* **55**, 14554 (1997).

[52] C.M. Varma, *Phys. Rev. B* **73**, 155113 (2006).

[53] C.M. Varma, *Nature* **468**, 184 (2010).

[54] S.A. Kivelson, I.P. Bindloss, E. Frandkin, V. Ognesyan, J.M. Tranquada, A. Kapitulnik and C. Howald, *Rev. Mod. Phys.* **75**, 1201 (2003).

[55] L. Taillefer, *J. Phys.: Condens. Matter* **21**, 164212 (2009).

[56] V.B. Geshkenbein, L.B. Ioffe and A.I. Larkin, *Phys. Rev. B* **55**, 3173 (1997).

[57] S. Tan and K. Levin, *Phys. Rev. B* **69**, 064510 (2004).

[58] A.S. Aleksandrov, *Phys. Rev. B* **48**, 10571 (1993); *J. Phys.: Condens. Matter* **22**, 426004 (2010).

[59] D.H. Kim, A.M. Goldman, J.H. Kang and R.T. Kampwirth, *Phys. Rev. B* **40** 8834 (1989).

[60] Q.Y. Ying and H.S. Kwok, *Phys. Rev. B* **42** 2242 (1990).

[61] S. Martin, A.T. Fiory, R.M. Fleming, G.P. Espinosa and A.S. Cooper, *Phys. Rev. Lett.* **62** 677 (1989).

[62] S.M. Ammirata, M. Friesen, S.W. Pierson, L.A. Gorham, J.C. Hunnicutt, M.L. Trawick and C.D. Keener, *Physica C* **313** 225 (1999).

[63] L.X. You, A. Yurgens, D. Winkler, C.T. Lin and B. Liang, *Supercond. Sci. Technol.* **19** S205 (2006).

[64] S.R. Currás, G. Ferro, M.T. González, M.V. Ramallo, M. Ruibal, J.A. Veira, P. Wagner and F. Vidal, *Phys. Rev. B* **68** 094501 (2003).

[65] L. Cabo, F. Soto, M. Ruibal, J. Mosqueira and F. Vidal, *Phys. Rev. B* **73** 184520 (2006).

[66] P.G. Radaelli, D.G. Hinks, A.W. Mitchell, B.A. Hunter, J.L. Wagner, B. Dabrowski, K.G. Vandervoort, H.K. Viswanathan and J.D. Jorgensen, *Phys. Rev. B* **49** 4163 (1994).

[67] M. Kofu, H. Kimura and K. Hirota, *Phys. Rev. B* **72** 064502 (2005).

[68] W.J. Skocpol and M. Tinkham *Rep. Prog. Phys.* **38**, 1049 (1975).

[69] A.P. Levanyuk, *Sov. Phys. JETP* **36**, 571 (1959).

[70] V.L. Ginzburg, *Fiz. Tverd. Tela* **2**, 1829 (1960).

[71] M.V. Ramallo and F. Vidal, *Europhys. Lett.* **39** 177 (1997).

[72] S.K. Ma, *Modern Theory of Critical Phenomena*, Benjamin, Reading, MA, 1976.

[73] M.V. Ramallo, Ph.D. Thesis, Universidade de Santiago de Compostela, 1998.

[74] N.D. Mermin and H. Wagner, *Phys. Rev. Lett.* **17** 1133 (1966).

[75] L.I. Glazman and A.E. Koshelev, *Phys. Rev. B* **43**, 2835 (1991).

[76] L.N. Bulaevskii, M. Ledvij and V.G. Kogan, *Phys. Rev. Lett.* **68** 3773 (1992).

[77] D. Feinberg, *J. Phys. III France* **4**, 169 (1994).

[78] B. Chattopadhyay and S.R. Shenoy, *Phys. Rev. Lett.* **72**, 400 (1994).

[79] S.R. Shenoy and B. Chattopadhyay, *Phys. Rev. B* **51**, 9129 (1995).

[80] L. Benfatto, C. Castellani and T. Giamarchi, *Phys. Rev. Lett.* **98**, 117008 (2007).

[81] J.P. Gollub, M.R. Beasley, R.S. Newbower and M. Tinkham, *Phys. Rev. Lett.* **22**, 527 (1969).

[82] L.G. Aslamazov and A.A. Varlamov, *L. Low Temp. Phys.* **38**, 223 (1980).

[83] B.R. Patton, V. Ambegaoker J.W. and Wilkins, *Solid State Commun.* **7**, 1287 (1969).

[84] See the comments in the Ref. 19 of J. Mosqueira, M.V. Ramallo, S.R. Currás, C. torrón and F. Vidal, *Phys. Rev. B* **65**, 174522 (2002).

[85] F. Vidal, C. Carballeira, S.R. Currás, J. Mosqueira, M.V. Ramallo, J.A. Veira and J. Viña, *Europhys. Lett.* **59**, 754 (2002).

[86] A.B. Pippard, *Proc. R. Soc. London, Ser. A* **216**, 547 (1953).

[87] F. Vidal, M.V. Ramallo, J. Mosqueira and C. Carballeira, *Int. J. Mod. Phys. B* **17**, 3470 (2003).

[88] P.G. de Gennes, *Superconductivity of Metals and Alloys*, sections 1-4, W.A. Benjamin, New York, 1966.

[89] C. Carballeira, S.R. Currás, J. Viña, J.A. Veira, M.V. Ramallo and F. Vidal, *Phys. Rev. B* **63** 144515 (2001).

[90] J. Mosqueira, C. Carballeira and F. Vidal, *Phys. Rev. Lett.* **87**, 167009 (2001).

[91] T. Timusk and B. Statt, *Rep. Prog. Phys.* **62** 61 (1999).

[92] S. Komiya, H.D. Chen, S.C. Zhang and Y. Ando, *Phys. Rev. Lett.* **94** 207004 (2005).

[93] F. Zhou, W.X. Ti, J.W. Xiong, Z.X. Zhao, X.L. Dong, P.H. Hor, Z.H. Zhang and W.K. Chu, *Supercond. Sci. Technol.* **16** L7 (2003).

[94] See B. Batlogg, H.Y. Hwang, H. Tagaki, R.J. Cava, H.L. Kao and J. Kwo, *Physica C* **235-240**, 130 (1994) and references therein.

[95] J.L. Tallon and J.W. Loram, *Physica C* **349**, 53 (2001).

[96] B. Fauqué, Y. Sidis, V. Hinkov, S. Pailhès, C.T. Lin, X. Chaud and P. Bourges, *Phys. Rev. Lett.* **96**, 53 (2006).

[97] J. Xia, E. Schemm, G. Deutscher, S.A. Kivelson, D.A. Bonn, W.N. Hardy, R. Liang, W. Siemons, G. Koster, M.M. Fejer and A. Kapitulnik, *Phys. Rev. Lett.* **100**, 127002 (2008).

[98] M.V. Ramallo, C. Carballeira, R.I. Rey, J. Mosqueira and F. Vidal, arXiv: cond-mat/1103.3314 (2011).

[99] F. Vidal, J.A. Veira, J. Maza, J. Mosqueira, C. Carballeira, in S.-L. Drechsler and T. Mishonov (Eds.) *High-T_c Superconductors and Related Materials: Materials Science, Fundamental Properties and Some Future Electronic Applications*, NATO Science series, Dordrecht, The Netherlands, 2001, p. 289 (also in arXiv: cond-mat/0510467). See also [100–102].

[100] E. Dagotto, *Science* **309** 257 (2005).

[101] K. McElroy, J. Lee, J.A. Slezak, D.H. Lee, H. Eisaki, S. Uchida and J.C. Davis, *Science* **309** 1048 (2005).

[102] Ø. Fischer, M. Kugler, I. Maggio-Aprile and C. Berthod, *Rev. Mod. Phys.* **79** 353 (2007).

[103] A. Guarino, R. Fittipaldi, A. Romano, A. Vecchione and A. Nigro, *Thin Solid Films* **524** 282 (2012).

[104] P. Berberich, B. Utz, W. Prusseit and H. Kinder, *Physica C* **219** 497 (1994).

[105] M. Lorenz, H. Hochmuth, D. Matusch, M. Kusunoki, V.L. Svetchnikov, V. Riede, I. Stanca, G. Kastner and D. Hesse, *IEEE Trans. Appl. Supercond.* **11** 3209 (2001). See also [104].

[106] M.R. Norman, *Science* **332** 196 (2011).

[107] D.N. Basov and A.V. Chubukov, *Nature Phys.* **7** 272 (2011). See also references therein.

[108] H.L. Kao, J. Kwo, R.M. Fleming, M. Hong and J.P. Mannaerts, *Appl. Phys. Lett.* **59** 2748 (1991).

[109] I.E. Trofimov, L.A. Johnson, K.V. Ramanujachary, S. Guha, M.G. Harrison, M. Greenblatt, M.Z. Cieplak and P. Lindenfeld, *Appl. Phys. Lett.* **65** 2481 (1994).

[110] M.Z. Cieplak, M. Berkowski, S. Guha, E. Cheng, A.S. Vagelos, D.J. Rabinowitz, B. Wu, I.E. Trofimov and P. Lindenfeld, *Appl. Phys. Lett.* **65** 3383 (1994).

[111] H. Sato and M. Naito, *Physica C* **274** 221 (1997).

[112] M. Suzuki, *Phys. Rev. B* **39** 2312 (1989).

[113] M. Suzuki and M. Hikita, *Phys. Rev. B* **44** 249 (1991); M. Suzuki and M. Hikita, *Phys. Rev. B* **47** 2913 (1993).

[114] G. Logvenov, A. Gozar and I. Bozovic, *Science* **326** 699 (2009).

[115] P.M. Singer, T. Imai, F.C. Chou, K. Hirota, M. Takaba, T. Kakeshita, H. Eisaki and S. Uchida, *Phys. Rev. B* **72** 014537 (2005).

[116] B.W. Hussey and A. Gupta, *J. Appl. Phys.* **72** 287 (1992).

[117] A. Gupta, B. Mercey, H. Hervieu and B. Raveau, *Chem. Mater.* **6** 1011 (1994).

[118] Y. Moriwaki, T. Sugano, A. Tsukamoto, C. Gasser, K. Nakanishi, S. Adachi and K. Tanabe, *Physica C* **303** 65 (1998).

[119] B. Mercey, P.A. Salvador, W. Prellier, T.D. Doan, J. Wolfman, J.F. Hamet, M. Hervieu and B. Raveau, *J. Mater. Chem.* **9** 233 (1999).

[120] P.A. Salvador, A.H. Haghiri-Gosnet, B. Mercey, M. Hervieu and B. Raveau, *Appl. Phys. Lett.* **75** 2638 (1999).

[121] W.C. Sheets, B. Mercey and W. Prellier, *Appl. Phys. Lett.* **91** 192102 (2007).

[122] Y. Thimont, Ph.D. Thesis, Université de Caen, 2009.

[123] J.L. Tallon, C. Bernhard, H. Shaked, R.L. Hitterman and J.D. Jorgensen, *Phys. Rev. B* **51** 12911 (1995).

[124] M.R. Presland, J.L. Tallon, R.G. Buckley, R.S. Liu and N.E. Flower, *Physica C* **176** 95 (1991).

[125] D. Most, J. Choi, L.J. Belenky and C.B. Eom, *Solid-State Electron.* **47** 2249 (2003).

[126] J. Mosqueira, M.V. Ramallo, A. Revcolevschi, C. Torrón and F. Vidal, *Phys. Rev. B* **59** 4394 (1999).

[127] J. Maza and F. Vidal, *Phys. Rev. B* **43** 10560 (1991).

[128] C. Carballeira, J. Mosqueira, A. Revcolevschi and F. Vidal, *Physica C* **384** 185 (2003).

[129] A. Pomar, M.V. Ramallo, J. Maza and F. Vidal, *Physica C* **225** 287 (1994).

[130] C. Torrón, A. Díaz, J. Jegoudez, A. Pomar, M.V. Ramallo, A. Revcolevschi, J.A. Veira and F. Vidal, *Physica C* **212** 440 (1993).

[131] F. Soto, C. Carballeira, J. Mosqueira, M.V. Ramallo, M. Ruibal, J.A. Veira and F. Vidal, *Phys. Rev. B* **70** 060501 (2004).

[132] D. Mihailovic, *Phys. Rev. Lett.* **94** 207001 (2005).

[133] Y.Q. Zhang, J.F. Ding, X.Q. Xiang, X.G. Li and Q.H. Chen, *Supercond. Sci. Technol.* **22** 085010 (2009).

[134] V.G. Kogan, *Phys. Rev. B* **75** 064514 (2007).

[135] L. Benfatto, C. Castellani and T. Giamarchi, *Phys. Rev. B* **80** 214506 (2009).

[136] D. Chang, B. Rosenstein and C.L. Wu, *Phys. Rev. B* **55**, 1162 (1997); W.Y. Chen, M.J. Chou and C.J. Lin, *Chinese J. Phys.* **36**, 250 (1998).

[137] J.P. Hurault, *Phys. Rev.* **179** 494 (1969).

[138] A. Schmid, *Phys. Rev.* **180** 527 (1969).

[139] A.A. Varlamov and L. Reggiani, *Phys. Rev. B* **45** 1060 (1992).

[140] C. Carballeira and V.V. Moshchalkov, *Phys. Rev. B* **71** 052503 (2005).

[141] I. Puica and W. Lang, *Phys. Rev. B* **68** 054517 (2003).

[142] A. Pomar, A. Díaz, M.V. Ramallo, C. Torrón, J.A. Veira and F. Vidal, *Physica C* **218** 257 (1993).

[143] See, *e.g.*, B.R. Patton, *Phys. Rev. Lett.* **27** 1273 (1971).

[144] See, *e.g.*, S. Kirkpatrick, *Rev. Mod. Phys.* **45** 574 (1973).

[145] A. Pomar, M.V. Ramallo, J. Mosqueira, C. Torrón and F. Vidal, *Phys. Rev. B* **54** 7470 (1996).

[146] S. Caprara, M. Grilli, L. Benfato and C. Castellani, *Phys. Rev. B* **84**, 014514 (2011).

[147] J. Viña, Ph.D. Thesis, Universidade de Santiago de Compostela, 2002.

[148] G. Ferro, Ph.D. Thesis, Universidade de Santiago de Compostela, 2010.

List of Figures

USC
UNIVERSIDADE
DE SANTIAGO
DE COMPOSTELA

List of Tables

USC
UNIVERSIDADE
DE SANTIAGO
DE COMPOSTELA

Resumen

Siguiendo el reglamento de los estudios de Tercer Ciclo de la Universidade de Santiago de Compostela, aprobado en la Junta de Gobierno el día 7 de abril de 2000 (DOG de 6 de marzo de 2001) y modificado por la Junta de Gobierno del 14 de noviembre de 2000, el Consejo de Gobierno del 22 de noviembre de 2003, del 18 de julio de 2005 (artículos 30 a 45), del 11 de noviembre de 2008 y del 14 de mayo de 2009; y, concretamente, cumpliendo las especificaciones indicadas en el capítulo 4, artículo 30, apartado 3 de dicho reglamento, mostramos a continuación un resumen en castellano de la tesis.

Entender los fenómenos críticos alrededor de la transición superconductora de los superconductores de alta temperatura (HTS) es un primer paso crucial para poder describir los mecanismos que conducen al apareamiento superconductor en estos materiales. [1–11] Hasta hace algunos años, la investigación en ambas temáticas avanzó de forma independiente la una de la otra, en correspondencia con el hecho de que la mayoría de las predicciones de las teorías para las fluctuaciones críticas, como la teoría Gaussiana-Ginzburg-Landau o las aproximaciones del grupo de renormalización, son universales e independientes de las interacciones microscópicas responsables del apareamiento.[1]

Recientemente ambos temas se han ido interrelacionando cada vez más entre sí, principalmente debido al creciente interés en relación con el problema de la localización de forma inambigua de las temperaturas de transición para la coherencia de fase superconductora y la condensación de la función de onda superconductora (T_{phase} y T_{cond} respectivamente), así como las distancias que las separan de la temperatura en la que aparece la superconductividad a escala macroscópica, T_{c}. [1–3, 20–36] Esta cuestión todavía abierta ha pasado a ser de relevante importancia debido a las propuestas (y a su enorme popularidad) hechas por varios autores, [3, 20–28] en las que se pone de manifiesto que la transición superconductora macroscópica en HTS podría ser determinada por fuertes fluctuaciones de la fase del parámetro de orden. En este denominado escenario de "fuertes fluctuaciones de la fase" y, al contrario de lo que ocurre en superconductores

[1] No obstante, existen varios precedentes en los cuales el estudio de las fluctuaciones superconductoras y el apareamiento sueperconductor en HTS han compartido problemáticas específicas: por ejemplo, el papel que juega la laminaridad de los planos de CuO_2, [9, 12–16] la simetría en onda d del apareamiento, [9, 15–18] o el tiempo de relajación de la función de onda superconductora [19].

convencionales de baja temperatura,[2] la condensación de la función de onda ocurriría a temperaturas $T_{\rm cond}$ mucho mayores que $T_{\rm phase}$ y $T_{\rm c}$, siendo en particular $T_{\rm phase} \simeq T_{\rm c}$, y $T_{\rm cond} - T_{\rm c}$ del orden de decenas o incluso cientos de Kelvin (dependiendo del autor y del HTS en concreto). [3, 20–28] Es importante mencionar que si $T_{\rm cond} \gg T_{\rm phase}$, entonces la búsqueda de los mecanismos que se esconden detrás de la superconductividad *a escala macroscópica* (y también los esfuerzos para intentar incrementar $T_{\rm c}$) debería centrarse en las correlaciones entre vórtices preformados, en lugar de entre los portadores del estado normal. Además, los fenómenos críticos asociados a la transición deberían ser muy diferentes de los que ocurren en los superconductores convencionales de baja temperatura. [3, 9–11, 20, 43]

Hasta ahora, la mayoría de los grupos que han investigado experimentalmente el escenario de fuertes fluctuaciones de la fase han buscado evidencias de trazas de señales de vórtices precursores por encima de la transición superconductora macroscópica, lo que confirmaría que $T_{\rm cond} \gg T_{\rm phase}$. [23–29] Sin embargo, las posibles confirmaciones positivas así resultantes han sido cuestionadas por explicaciones alternativas en términos de, por ejemplo, el desorden químico y las resultantes inhomogeneidades de temperatura crítica [34–36], o también en términos de la dependencia con el campo magnético de varias posibles formas de orden no superconductor en el estado normal [30, 50–53, 55, 58].

El objetivo principal de esta tesis es explorar este problema a través de la medida simultánea de dos características exclusivas que se espera que se produzcan en las curvas de voltaje-intensidad ($V - I$) cerca de $T_{\rm phase}$ y $T_{\rm cond}$: El salto desde un comportamiento óhmico hasta $V \propto I^3$ (el llamado salto de Nelson) en $T_{\rm phase}$, y para $T_{\rm cond}$ el redondeo crítico de la resistividad óhmica debido a las fluctuaciones críticas superconductoras. Con el fin de obtener resultados inambiguos, es importante llevar a cabo estas medidas en un conjunto de muestras con un rango de niveles de dopaje que cubran las regiones subdopadas, óptimamente dopadas y sobredopadas. También es fundamental para caracterizar de la forma más completa posible, los efectos de las inhomogeneidades de temperatura crítica, tanto a partir del crecimiento de muestras especialmente homogéneas y caracterizando cuidadosamente los efectos de las inhomogeneidades en las medidas de curvas $V - I$Ėstos aspectos nos permiten mejorar las medidas anteriores de otros autores en los cupratos $Tl_2Ba_2CaCu_2O_8$ [59], $YBa_2Cu_3O_7$ [60] y $Bi_2Sr_2CaCu_2O_8$ [61–63] que midieron el salto de Nelson y el redondeo de la resistividad, pero no los midieron en función del dopaje, ni se tuvieron en cuenta los efectos de las inhomogeneidades de temperatura crítica. En este trabajo se extienden también resultados anteriores de nuestro grupo en películas delgadas de $La_{2-x}Sr_xCuO_4$ que se centraban sólo en el redondeo de resistividad. [64]

Para entender el trabajo y las conclusiones que conforman esta tesis, antes definiremos mejor las temperaturas de coherencia de fase $T_{\rm phase}$ y de condensación superconductora $T_{\rm cond}$ que hemos introducido antes, así como las distintas propuestas que hay para situar

[2] En los superconductores de baja temperatura es bien sabido [37–47] que en muestras masivas $T_{\rm cond}$, $T_{\rm phase}$ y $T_{\rm c}$ son experimentalmente indistinguibles unas de otras. En algunas películas delgadas, la diferencia $T_{\rm cond} - T_{\rm phase}$ puede ser mayor, pero solo de hasta $\sim$ 3K. Es interesante mencionar que, de hecho, las primeras y principales comprobaciones experimentales de estos valores de $T_{\rm cond}$ y $T_{\rm phase}$ se obtuvieron en medidas de curvas voltaje-intensidad [37–42] similares a las que se presentan en esta tesis.

estas temperaturas en el diagrama de fases de los HTS.

Resumen de las temperaturas características para las fluctuaciones en un superconductor 2D: T_{phase}, T_{cond}, T_{LG} y T^{C}.

Para introducir y contextualizar de forma más precisa nuestro objetivo, antes vamos a presentar una descripción de las principales temperaturas características relacionadas con la transición superconductora y con las fluctuaciones superconductoras en un superconductor de tipo II bidimensional (2D) y homogéneo sin campo magnético. Complementariamente, la figura 1 ilustra las distintas temperaturas objeto de discusión.

Debemos enfatizar que esta descripción es general tanto para el escenario de "fuertes fluctuaciones de la fase" como para el escenario de "fluctuaciones convencionales". Las diferencias entre ambos escenarios radicarán en los valores específicos de estas temperaturas, especialmente en la distancia entre T_{phase} y T_{cond}.

La transición sin efectos de fluctuaciones.

Comenzamos esta descripción considerando un caso preliminar y simple en el que los efectos de las fluctuaciones son despreciables. Teniendo en cuenta esta simplificación, la función de onda superconductora Ψ es nula por encima de una cierta temperatura crítica que, por conveniencia, denotaremos como T_{cond} (temperatura de condensación de la función de onda). Por debajo de T_{cond}, Ψ toma un valor dependiente de la temperatura cuyo módulo es positivo y su fase es arbitraria. Esta es simplemente la solución que resulta al minimizar la energía libre superconductora de Ginzburg-Landau (GL) $\Delta F[\Psi]$. Hay que destacar que cualquier variación espacial de Ψ contribuiría positivamente a $\Delta F[\Psi]$ (siendo el término asociado en el modelo GL $\propto |\nabla\Psi|^2$) y además tanto el módulo como la fase de Ψ serían espacialmetne uniformes por debajo de T_{cond}. [10]

División de la transición en T_{phase} y T_{cond}.

Incluyamos ahora los efectos de las fluctuaciones asociadas a la proximidad de la transición. Seguimos definiendo T_{cond} como la temperatura en la que el valor de Ψ es el primer mínimo de $\Delta F[\Psi]$ distinto de cero. En otras palabras, se corresponde con la temperatura en la que por primera vez es energéticamente favorable formar pares superconductores. Sin embargo, debido a las fluctuaciones, esos pares pueden existir ya por encima de T_{cond}, correspondiéndose así con las configuraciones de Ψ que no minimizan $\Delta\Psi[F]$.[3] Suficientemente por encima de T_{cond}, los efectos de las fluctuaciones se pueden describir como pequeñas perturbaciones de tipo Gaussiano. [10, 68] Ésto es lo que se

[3]La función de onda global es la media de todos los posibles valores de Ψ, cada uno de ellos ponderado por el factor $\omega[\Psi] \propto \exp(-\Delta F[\Psi]/k_{\mathrm{B}}T)$, donde k_{B} es la constante de Boltzmann. [10,68] Naturalmente, este peso estadístico $\omega[\Psi]$ es máximo en el valor de Ψ que minimiza $\Delta F[\Psi]$, pero cuando el pico de $\omega[\Psi]$ se anchea (por ejemplo, debido a la proximidad de T_{c}) también las configuraciones de Ψ que no minimizan $\Delta F[\Psi]$ contribuyen a los promedios estadísticos. [10, 68]

denomina aproximación Gaussiana de Ginzburg-Landau (GGL). Las predicciones GGL se dan generalmente en términos de la temperatura reducida $\varepsilon \equiv \ln(T/T_{\rm cond})$, que se puede aproximar como $\varepsilon \simeq (T-T_{\rm cond})/T_{\rm cond}$ para valores pequeños de $\varepsilon \lesssim 0.1$. [10,68] La región de validez de la aproximación GGL (región GGL) se encuentra en la zona de temperaturas reducidas por encima de un determinado valor, $\varepsilon \gtrsim \varepsilon_{\rm LG}$. Usamos el subíndice LG en reconocimiento a los trabajos pioneros de Levanyuk [69] y Ginzburg [70] que fueron los primeros que consideraron esta región GGL. Levanyuk y Ginzburg también desarrollaron un criterio para estimar $\varepsilon_{\rm LG}$ mediante la comparación entre el salto de campo medio de la capacidad calorífica y la capacidad calorífica inducida por fluctuaciones; cuando se aplica a los HTS laminares, este criterio produce $\varepsilon_{\rm LG} \sim 10^{-2}$ [71] (de modo que la región GGL se corresponde con $T > T_{\rm LG} \sim 1.01 T_{\rm cond}$). En la región GGL, las configuraciones de Ψ se pueden interpretar como "gotas" o islas dinámicas (en el sentido de que dependen del tiempo) de valores $\Psi \neq 0$, rodeadas por un "mar" donde $\Psi = 0$ (véase la figura 1). El tamaño típico de estas islas se corresponde con la longitud de coherencia de Ginzburg-Landau $\xi(\varepsilon) = \xi(0)\varepsilon^{-1/2}$, donde $\xi(0)$ es la amplitud GL en la dirección planar. [10,68] El término "fluctuaciones de la amplitud" se asocia a menudo con la región GGL [1–3,20–28] para destacar que estas configuraciones no son descriptibles en términos de excitaciones topológicas, es decir, en términos de vórtices. Sin embargo, esta denominación también es algo confusa ya que tanto la amplitud como la fase de Ψ fluctúan en la región GGL por encima de la transición superconductora.[4]

En cambio, cuando nos acercamos más a la transición, para $\varepsilon < \varepsilon_{\rm LG}$,los efectos de las fluctuaciones se vuelven más importantes y deben ser tratados en términos de aproximaciones completamente críticas tales como por ejemplo el método del grupo de renormalización. [72] En el caso 2D, como demostraron simultáneamente Berezinskii [44] y Kosterlitz y Thouless [45] (BKT) en superfluidos, y más tarde varios autores en superconductores de tipo II (ver, por ejemplo, [43, 46, 47]), las excitaciones relevantes son topológicas y formadas por vórtices, incluso en ausencia de campo magnético externo. Además se produce un cambio importante en sus configuraciones a una temperatura que generalmente se conoce como "temperatura BKT" o "temperatura de coherencia de fase", $T_{\rm phase}$: [1–3, 20–29, 44, 45] Para $T > T_{\rm phase}$ los vórtices son esencialmente independientes unos de otros, mientras que para $T < T_{\rm phase}$ algunos vórtices de circulación opuesta se unen en pares (pares vórtice-antivórtice).[5] Como indicaron por primera vez BKT, [44,45] $T_{\rm phase}$ está localizada por debajo de $T_{\rm cond}$ y es en $T_{\rm phase}$ donde el parámetro de orden superconductor pasa a tener coherencia de largo alcance.[6] Esta coherencia de largo alcance es un requisito necesario para mostrar completamente las características superconductoras macroscópicas habituales, tales como, por ejemplo, un efecto Meissner completo.

Se ha argumentado que también para superconductores laminares y superconductores 3D las teorías del grupo de renormalización conducen a que los vórtices sean las

[4] De hecho, para $\varepsilon > \varepsilon_{\rm LG}$ ambos grados de libertad contribuyen de igual forma a la densidad superfluida de fluctuaciones. [72, 73]

[5] Cabe destacar que el apareamiento vórtice-antivórtice sucede en el espacio real, al contrario que el apareamiento BCS convencional que se produce en el espacio de momentos.

[6] O de cuasi-largo alcance, en correspondencia con el teorema de Mermin y Wagner que indica que en un sistema 2D con simetría continua no hay ningún orden de largo alcance a temperatura finita [74].

excitaciones relevantes de la función de onda superconductora incluso sin la presencia de un campo magnético externo. [75–80] Estos superconductores experimentarían una división de la transición en $T_{\rm cond}$ y $T_{\rm phase}$, aunque en este caso los apareamientos de vórtices pueden ser más complejos. Por ejemplo, en el caso 3D el apareamiento vórtice-antivórtice es sustituido por el entrelazamiento de bucles de vórtices, con una libertad de orientación más grande. [75–80] Además, mientras que la diferencia $T_{\rm cond} - T_{\rm phase}$ parece ser difícil de estimar en cualquier dimensión, sí parece claro (al menos a partir de experimentos en superconductores de baja $T_{\rm c}$ [37–42]) que cuanto más comportamiento 3D tiene el superconductor, más cerca están entre sí las temperaturas $T_{\rm cond}$ y $T_{\rm phase}$. [75–80]

El límite de altas temperaturas T^{C} de la región de fluctuaciones.

Como ya estipularon en 1969 Gollub y colaboradores en su trabajo pionero [81] (ver también Refs. [9,10]), las aproximaciones usuales GGL de campo medio sólo son válidas en la región $\varepsilon_{\rm LG} \lesssim \varepsilon \ll 1$. Desde entonces, ha habido varios intentos con propuestas para extender hasta regiones de altos valores de ε estas descripciones de campo medio, incluyendo la introducción de distintas versiones del convencional corte o "cutoff" en momentos, [82] o penalizaciones ad-hoc (que non son implícitamente cutoffs) de los modos de fluctuaciones de la longitud de onda que tienen en cuenta la localización cuántica. [83, 84] Sin embargo, ninguna de estas propuestas conduce al desvanecimiento de todos los modos de las fluctuaciones por encima de una temperatura bien definida, T^{C}. Esta T^{C} fue propuesta en la Ref. [85] teniendo en cuenta los límites impuestos por el principio de incertidumbre de Heisenberg al encogimiento, cuando la temperatura aumenta por encima de $T_{\rm cond}$, de la longitud de coherencia, $\xi(T)$, que no puede ser más pequeña que $\xi_{T=0\rm K}$, la longitud de coherencia real (o longitud de coherencia de Pippard [86]) a $T = 0$K, es decir,

$$\xi(T) \gtrsim \xi_{T=0\rm K}. \tag{1}$$

Esta condición conlleva directamente a una temperatura T^{C} bien definida, dada por $\xi(T^{\mathsf{C}}) = \xi_{T=0\rm K}$, por encima de la cual todos los modos de fluctuaciones son nulos. El correspondiente cutoff en temperatura reducida es simplemente $\varepsilon^{\mathsf{C}} \equiv \ln(T^{\mathsf{C}}/T_{\rm cond})$. Hay que destacar además que la condición (1) es de hecho compatible con la superconductividad en muestras de tamaños menores que $\xi_{T=0\rm K}$, ya que, como se citó anteriormente en la Ref. [87], en dichos superconductores la longitud de coherencia de Pippard pierde su sentido convencional (desde un punto de vista simplista, en estos superconductores de pequeño tamaño la amplitud de la longitud de coherencia también se ve reducida respecto al tamaño que tiene en superconductores masivos).

Como también se pone de manifiesto en la Ref. [85], la condición (1) es general, y debe aplicarse a cualquier descripción teórica de la transición superconductora. Solamente el valor de ε^{C} dependerá de cada aproximación particular a través de la dependencia con la temperatura de $\xi(T)$ y la relación entre $\xi(T)$ y $\xi_{T=0\rm K}$. Un ejemplo relevante para este caso se corresponde con la combinación de la dependencia de la longitud de coherencia con la temperatura de campo medio $\xi(T) = \xi(0)\varepsilon^{-1/2}$ (y, por lo tanto, $\varepsilon^{\mathsf{C}} = (\xi(0)/\xi_{T=0\rm K})^2$), con la relación entre $\xi(T)$ y $\xi_{T=0\rm K}$ propuesta por la teoría BCS, para la cual en el límite limpio se tiene $\xi(0) = 0.74\xi_{T=0\rm K}$. [88] Esto lleva entonces a $\varepsilon^{\mathsf{C}} \approx 0.55$, es decir,

$T^{\mathsf{C}} \approx 1.7T_{\mathrm{cond}}$. [85, 89] Una estimación similar usando las relaciones del límite sucio produce $\varepsilon^{\mathsf{C}} \simeq 0.6$. [11, 90] Una forma usual de introducir estas ideas en la aproximación GGL es a través de un cutoff en energía total en los promedios estadísticos como se hizo, por ejemplo, en las Refs. [64, 89]: en unidades de $\hbar^2/(2m^*)$ (donde $\hbar$ es la constante de Planck reducida y m^* es la masa efectiva de los pares superconductores),

$$k^2 + \xi^{-2}(\varepsilon) < \varepsilon^{\mathsf{C}}\ \xi^{-2}(0), \tag{2}$$

donde k^2 se corresponde con la contribución de cutoff en momentos, mientras que $\xi^{-2}(\varepsilon)$ se puede interpretar como la localización en energía de Heisenberg.

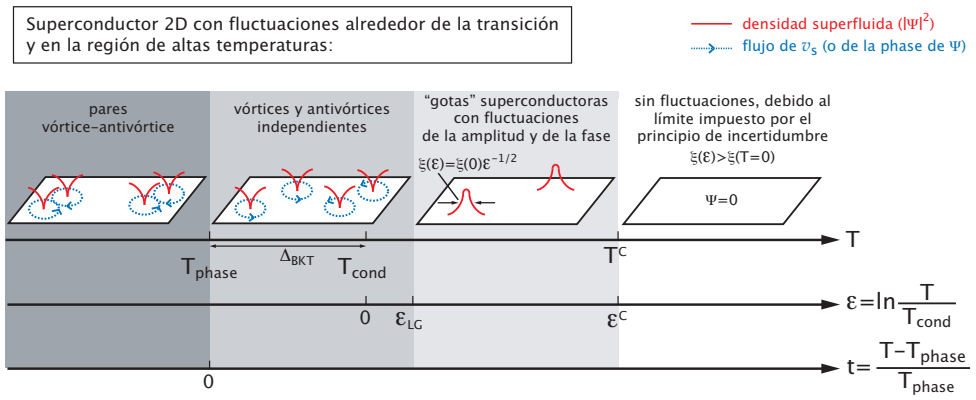

Figura 1: Principales temperaturas características para las fluctuaciones en un superconductor 2D.

Dos posibles escenarios para el diagrama de fases de T_{phase} y T_{cond} de los HTS.

El escenario de "fuertes fluctuaciones de la fase".

Como ya se ha mencionado al principio de este resumen, la investigación de los mecanismos de apareamiento en HTS ha llevado a varios autores a proponer la posibilidad de que T_{cond} esté decenas o incluso cientos de Kelvin por encima de T_{phase}. De hecho, estas propuestas también están vinculadas con la búsqueda de explicaciones para tratar de comprender el apareamiento superconductor y la llamada temperatura de pseudogap T_{pgap} que aparece en el diagrama de fases de los cupratos. Esta temperatura se corresponde con la aparición de diversas características experimentales que indican que alrededor de T_{pgap} la densidad de estados de portadores normales cerca de la superficie de Fermi (DOS) experimenta una depresión, es decir, alrededor de T_{pgap} los portadores del estado

normal son eliminados de los estados capaces de presentar excitaciones de partículas aisladas (como se puede observar en varios experimentos basados en fotoemisión ARPES, efecto Hall o resistividad, entre otros [91]). Esta reducción de DOS parece explicar, al menos cualitativamente, las principales características anómalas del estado normal de los cupratos. [2, 91]

Las propuestas que se basan en que T_{cond} podría ser en HTS mucho mayor que T_{phase} surgieron a partir de la idea de un nuevo estado en el que los portadores normales se mueven cuando $T \simeq T_{\mathrm{pgap}}$ podría ser algún tipo de precondensación de pares con comportamiento similar a los de un superconductor, como fue propuesto primeramente por Emery y Kivelson [3] y luego por otros autores. [3, 20–29] La razón por la cual estos pares podrían en un principio no dar lugar a una fenomenología superconductora a escala macroscópica sería que la función de onda superconductora formada por esos pares experimentaría fuertes fluctuaciones de su fase. [3] La fenomenología macroscópica aparecería sólo cuando se estableciese la coherencia de fase. Por lo tanto, estas propuestas se pueden resumir diciendo que T_{cond} sería esencialmente igual a T_{pgap}, y T_{phase} sería esencialmente igual a la temperatura crítica superconductora macroscópica T_{c}. [3, 20–29] Resumimos ese escenario en el recuadro principal (a) de nuestra figura 2. En esta figura, así como en el resto de este trabajo, x determina el nivel de dopaje.[7] Hay que tener en cuenta que el valor de T_{pgap} varía fuertemente con el dopaje x, siendo en particular para los cupratos subdopados ($x < 0.16$) mucho mayor que T_{c}.[8] Todavía no está claro cuál es la línea de $T_{\mathrm{pgap}}(x)$ para los HTS con dopaje óptimo ($x = 0.16$) y para los sobredopados ($x > 0.16$). En el recuadro principal (a) de la figura 2 se ha escogido la opción en la que para $x \geq 0.16$ se cumple también $T_{\mathrm{pgap}} > T_{\mathrm{c}}$ como se propone, por ejemplo, en estudios basados en medidas resistividad Hall, etc. [91, 94]

Otros autores como por ejemplo [95–97] proponen que para $x \geq 0.16$ es $T_{\mathrm{pgap}} \leq T_{\mathrm{c}}$, basándose principalmente en medidas de resistividad y capacidad calorífica. En ese caso T_{cond} sería bastante mayor que T_{phase} sólo para las composiciones subdopadas. En el recuadro (b) de la figura 2 se representa el diagrama de fases de esta variación del escenario de "fuertes fluctuaciones de la fase".

Aún existe una tercera variante, [23–29] que se representa en el recuadro (c) de la figura 2. En este caso T_{cond} no se identifica tan directamente con T_{pgap}, pero sí con la temperatura en la que algunas muestras exhiben un cambio relativamente brusco en la dependencia con la temperatura y el campo magnético del coeficiente de Nernst, [25, 26] la magnetización en corriente continua dc, [23, 24, 27, 28] o las derivadas de la resistividad en corriente continua [29]. Los autores de estas medidas atribuyen esos efectos a un inicio de la superconductividad debido a la entrada en la región de $T < T_{\mathrm{cond}}$. En este tercer escenario, no está claro aún cuál sería el motivo de la discrepancia entre T_{cond} y

[7] Concretamente, x determina la densidad de huecos por celda unidad. Para el $La_{2-x}Sr_xCuO_4$, coincide con el índice estequiométrico del Sr (siempre para concentraciones saturadas de oxígeno). En general, la correspondencia entre x y los índices de las fórmulas estequiométricas es específica para cada compuesto HTS.

[8] En cuanto a la dependencia $T_{\mathrm{c}}(x)$, es bien sabido que tiene forma de parábola, centrada alrededor de $x = 0.16$ y con una cierta depresión alrededor de $x = 1/8$ (denominado normalmente "dopaje mágico"). [66, 92, 93] Los valores $x = 0.16$ y $x = 1/8$ son universales para todos los HTS dopados con huecos, mientras que la profundidad de la depresión en $x = 1/8$ depende del compuesto en particular.

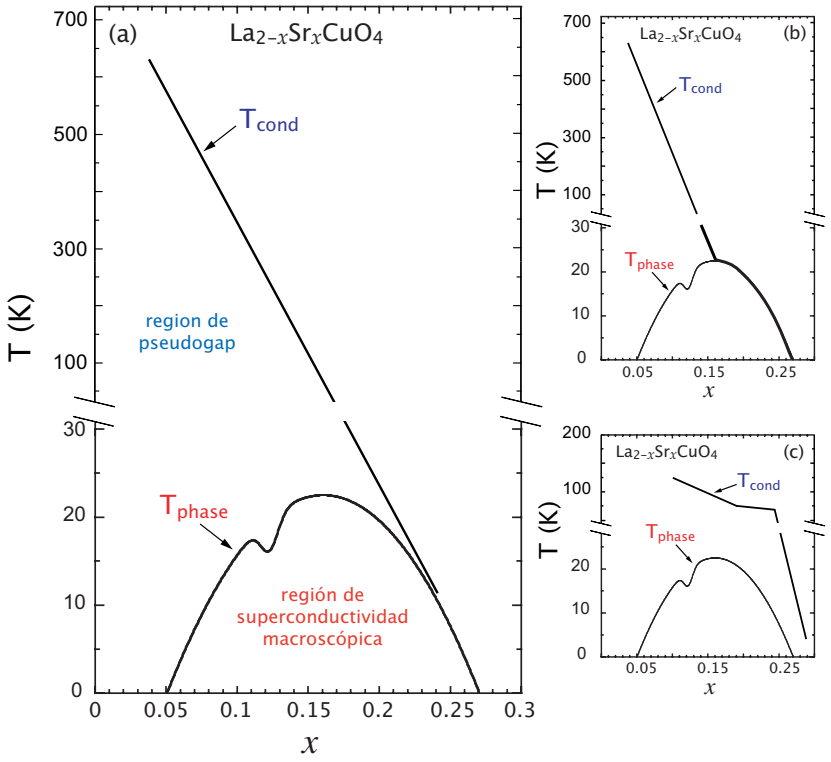

Figura 2: Tres alternativas para el escenario de *"fuertes fluctuaciones de la fase"* en los HTS. En el recuadro principal (a) $T_{\rm cond}$ es esencialmente $T_{\rm pgap}$ y puede ser mucho mayor que $T_{\rm phase}$, que es esencialmente $T_{\rm c}$. En este recuadro (a), $T_{\rm cond}$ y $T_{\rm pgap}$ están siempre por encima de $T_{\rm phase}$ para todos los dopajes x. En el recuadro (b) $T_{\rm pgap}$ puede estar por debajo de la campana superconductora para $x \gtrsim 0.13$, y entonces $T_{\rm cond}$ es el máximo entre $T_{\rm pgap}$ y $T_{\rm c}$. En el recuadro (c) $T_{\rm cond}$ no se asocia directamente con $T_{\rm pgap}$ sino con un límite máximo ("onset") por encima de $T_{\rm c}$ para varios observables que dependen de la temperatura y del campo magnético como, por ejemplo, el efecto Nernst (ver el texto principal para más detalles).

$T_{\rm pgap}$, aunque dos posibilidades obvias serían *i)* que las medidas no son lo suficientemente sensibles como para detectar el verdadero inicio de superconductividad precursora, y por lo tanto la línea de $T_{\rm phase}(x)$ en el recuadro (c) de la figura 2 se correspondería en realidad con un límite inferior para esa temperatura, o *ii)* que $T_{\rm phase}$ y $T_{\rm pgap}$ no estarían relacionadas en absoluto.

El escenario de "fluctuaciones superconductoras convencionales".

En el escenario de "fluctuaciones superconductores convencionales", $T_{\rm cond}$ y $T_{\rm phase}$ están relativamente cerca una de la otra en los HTS para todos los dopajes (al igual que ocurriría en un superconductor convencional de baja temperatura de dimensiones similares). En este caso, tanto las líneas de $T_{\rm cond}(x)$ como de $T_{\rm phase}(x)$ del diagrama de fases deben mostrar parábolas más o menos similares a la línea que establece la aparición de la fenomenología superconductora a escala macroscópica $T_{\rm c}(x)$. Cabe esperar que estas parábolas sean esencialmente paralelas entre sí separadas mediante una distancia $\Delta_{\rm BKT}$ por debajo de aproximadamente 5K. Este escenario para el diagrama de fases se representa en la figura 3.

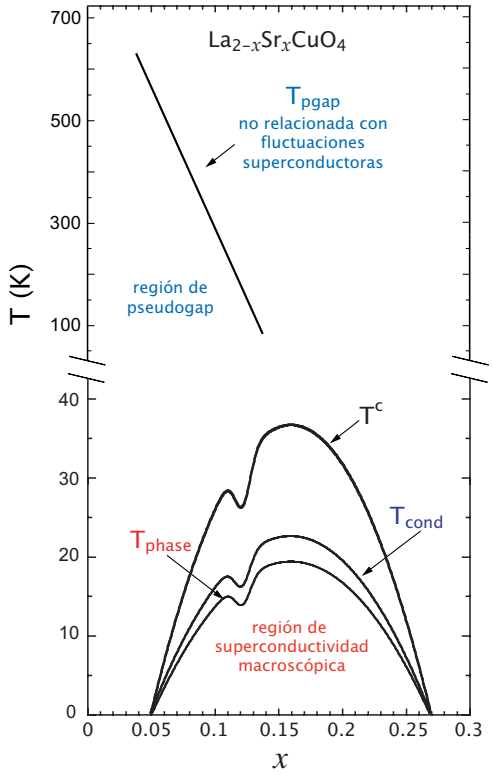

Figura 3: Esquema del diagrama de fases de los HTS en un escenario de *"fluctuaciones superconductoras convencionales"*. En esta situación $T_{\rm cond}$ y $T_{\rm phase}$ estarían relativamente cerca una de la otra para todos los dopajes.

Por todo lo anteriormente expuesto, la motivación principal de la presente tesis doctoral puede reformularse a partir de la siguiente cuestión: "Para tratar de determinar

cuál es la verdadera situación que se da en los HTS, ¿cuál es el escenario correcto? ¿El que se representa en la figura 2, o el de la figura 3?"

En el escenario de "fluctuaciones superconductoras convencionales", uno también se puede preguntar cuál sería la explicación de los fenómenos que se observan muy por encima de T_c y que llevaron a proponer el escenario de "fuertes fluctuaciones de la fase". En particular, nos podemos preguntar si existen explicaciones que no sean $T_{cond} \gg T_c$ capaces de explicar las líneas de $T_{pgap}(x)$ en las figuras 2(a) y 2(b), así como la línea en la figura 2(c) en la que algunas muestras exhiben un cambio relativamente brusco en la dependencia con la temperatura y el campo magnético de varios observables y de hecho, varias explicaciones alternativas han sido propuestas por diferentes autores:

Por un lado, se han expuesto explicaciones para los fenómenos experimentales en los que algunas muestras exhiben un cambio relativamente brusco en la dependencia con la temperatura y el campo magnético de varios observables, en términos de desorden químico y las correspondientes inhomogeneidades en la temperatura crítica. Por ejemplo, se ha demostrado en [34–36, 98] que incluso cantidades muy pequeñas (e inevitables) de inhomogeneidades, pueden imitar los comportamientos de señales de superconductividad precursora observadas en las Refs. [23–29] e interpretadas en esos trabajos como evidencias de $T_{cond} \gg T_c$. Es importante mencionar que estas inhomogeneidades también explicarían la observación importante de que, en medidas de magnetización de polvos de HTS, se produce una disminución de estos comportamientos cuando las muestras son resintetizadas tras varios ciclos de calentamiento y molido (que mantienen el dopaje global y mejoran la homogeneidad de las muestras). [34, 35]

En segundo lugar, existen propuestas teóricas para explicar la física del apareamiento en HTS que reivindican la aparación muy por encima de T_c de diferentes tipos de orden (distinto al orden superconductor), y que en un principio son capaces de producir una reducción de DOS en T_{pgap}.[9] Ejemplos conocidos son las propuestas de formación de densidades de ondas de carga y spin con simetría d dadas (por Chakravarty, Laughlin y colaboradores [49,50]), de corrientes de carga circulares (por Varma y colaboradores [51–53]) de formaciones filamentares oscilantes de carga (por ejemplo, por Kivelson y colaboradores [54], ver también [30, 55]), o de localización de pares condensados tipo Bose apantallados por portadores normales (por Geshkenbein y colaboradores [56]; en este caso, *no* serían *pares superconductores* debido al apantallamiento, ver también los trabajos relacionados [57, 58]). Además, varios trabajos experimentales recientes señalan la posibilidad de una reconstrucción de la superficie de Fermi en función de la temperatura, principalmente para composiciones subdopadas. [30, 55] Esta reconstrucción también podría producir una reducción efectiva de DOS.

[9] De hecho, estos órdenes pueden también aumentar las respuestas en función de la temperatura y del campo magnético.

Principales aportaciones y conclusiones.

Una vez que hemos situado y contextualizado el objetivo fundamental de esta tesis, pasamos a describir los principales avances que aportamos en este trabajo de investigación:

Crecimiento de películas delgadas de $La_{2-x}Sr_xCuO_4$ y determinación de su dispersión en temperaturas críticas ΔT_c.

Hemos desarrollado un nuevo método de deposición mediante láser pulsado ("Pulsed Laser Deposition", PLD) capaz de crecer sobre sustratos de $SrTiO_3$ películas delgadas (de espesor ~ 200 nm) de $La_{2-x}Sr_xCuO_4$ con diversos dopajes x a partir de dos blancos de $La_{1.1}Cu_{0.9}O_{2.4}$ y $SrCuO_2$. Hemos desarrolado este método ya que la técnica habitual de emplear un solo blanco limitaría la homogeneidad final de nuestras películas. Los parámetros básicos de nuestras muestras pueden consultarse en nuestra tabla 1. Creemos que esta es la primera vez que se aplica este procedimiento para variar sistemáticamente el dopaje de un HTS: Al variar el número de disparos del láser sobre la superficie del blanco de $La_{1.1}Cu_{0.9}O_{2.4}$ con respecto al blanco de $SrCuO_2$, hemos podido obtener varias películas con diferentes composiciones de dopaje ($0.09 \lesssim x \lesssim 0.22$). También hemos llevado a cabo medidas básicas de caracterización (XRD, AFM, SEM, EDX) en estas películas, que indican su buena calidad estructural. Además caracterizamos la homogeneidad de la temperatura crítica superconductora T_c por medio de magnetometría de alta resolución SQUID, que permite determinar no sólo el valor medio $\overline{T}_c$ sino también la dispersión debida a las inhomogeneidades, ΔT_c, en cada muestra (las ΔT_c en cada muestra han sido obtenidas a partir del ancho de la derivada de la susceptibilidad a la altura media del pico de la transición; lo que comúnmente se denota como FWHM). Estas medidas se resumen en la figura 4. Los resultados muestran que la homogeneidad de nuestras películas está entre las mejores reportadas hasta ahora para cualquier HTS, ya sea en superconductores masivos o en películas. De hecho, también se muestra que sus dispersiones ΔT_c están en la mayoría de los casos a un nivel comparable con el mínimo e inevitable desorden debido a la aleatoriedad intrínseca en el posicionamiento o colocación de los iones de Sr (el llamado desorden químico intrínseco). Se ha comprobado además que este desorden químico es compatible con tener dominios de T_c en los planos de CuO_2 cuyo radio efectivo es ~ 80 celdas unidad de CuO_2. Los resultados de esta parte de la tesis se ponen de manifiesto en el capítulo 2 de esta tesis doctoral y en un artículo que será publicado en breve en la revista *Superconductor Science and Technology*.

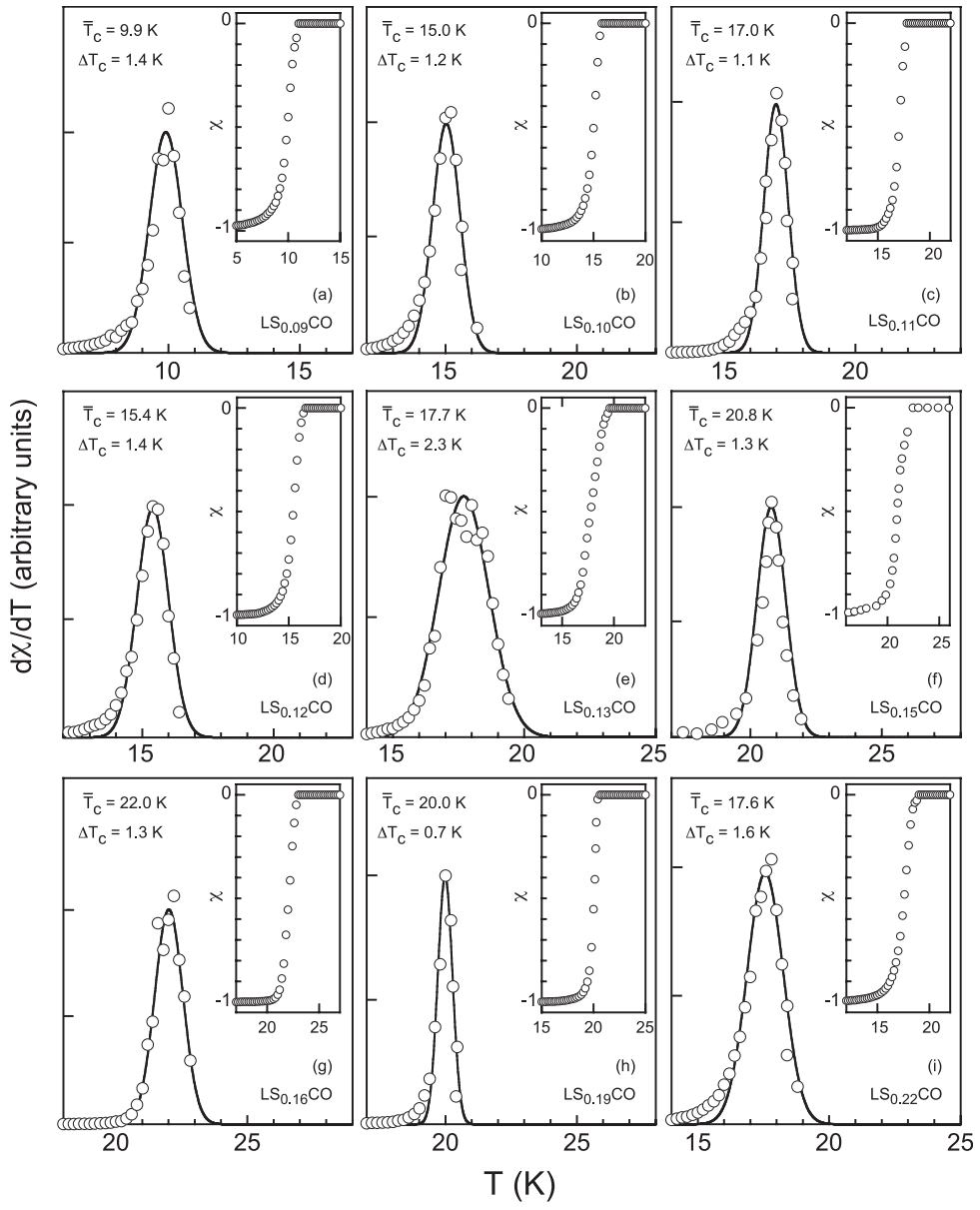

Figura 4: Medidas a ZFC de la susceptibilidad magnética en películas delgadas de $La_{2-x}Sr_xCuO_4$.

muestra	x (nominal)	espesor (nm, ±10%)	$\overline{T}_c$ (K)	ΔT_c (K)
$LS_{0.09}CO$	0.09	325	9.9	1.4
$LS_{0.10}CO$	0.10	200	15.0	1.2
$LS_{0.11}CO$	0.11	175	17.0	1.1
$LS_{0.12}CO$	0.12	275	15.4	1.4
$LS_{0.13}CO$	0.13	300	17.7	2.3
$LS_{0.15}CO$	0.15	150	20.8	1.3
$LS_{0.16}CO$	0.16	275	22.0	1.3
$LS_{0.19}CO$	0.19	250	20.0	0.7
$LS_{0.22}CO$	0.22	200	17.6	1.6

Tabla 1: Principales parámetros de las películas de $La_{2-x}Sr_xCuO_4$ sintetizadas mediante PLD estudiadas en este trabajo.

Simulación numérica del comportamiento eléctrico de un superconductor con inhomogeneidades de la temperatura crítica en la transición BKT.

Con el objetivo de contar con indicadores teóricos fiables para identificar de forma inambigua $T_{\rm cond}$ y $T_{\rm phase}$, se ha estudiado el comportamiento eléctrico cerca de la transición BKT de tipo vórtice-antivórtice de los superconductores planos con inhomogeneidades de la temperatura crítica. Para ello se ha analizado en términos de cálculos por elementos finitos las curvas de voltaje-intensidad cerca la transición superconductora BKT. Las muestras estudiadas se modelaron como una malla cuadrada de resistencias de dimensión $N \times N$ (con $N = 10$) donde cada nodo tenía una temperatura crítica $T_{\rm cond}$ diferente y una temperatura de coherencia de fase $T_{\rm phase}$ también distinta extraídas de distribuciones Gaussianas con valores medios $\overline{T}_{\rm cond}$ y $\overline{T}_{\rm phase}$ respectivamente. Ambas distribuciones además tenían igual dispersión, ΔT_c. Para cada resistencia $T_{\rm cond}$ y $T_{\rm phase}$ eran iguales a las de su correspondiente nodo inferior izquierdo y se incluyó en nuestro modelo una fuente de corriente externa conectada (con resistencia cero) a los bordes opuestos de la muestra, para así ser capaces de extraer los resultados de las simulaciones, siendo I la corriente aplicada, V la caída de tensión o voltaje entre los dos bordes de la muestra y $V \propto I^{\alpha}$ la relación entre ellos (es decir, el exponente α se corresponde con la pendiente en escala logarítmica de las curvas $V - I$). Ejemplos de los resultados de dichas simulaciones pueden verse en las figuras 5, 6 y 7. Los resultados de tales simulaciones demuestran que el fuerte salto que se produce en el exponente (pasando éste de seguir un comportamiento óhmico con $\alpha = 1$ a tener el valor $\alpha = 3$ en la región de voltajes $3 < V < 30$ μV) es válido para proporcionar una buena estimación de la ubicación del valor medio $\overline{T}_{\rm phase}$. Los resultados también revelan que se producen fuertes redistribuciones de la corriente local y del mapa de voltajes alrededor de $\overline{T}_{\rm phase}$ cuando aproximadamente el 50 % de la muestra ha experimentado ya la transición BKT. Las simulaciones nos han permitido por otra parte cuantificar el ancheamiento que se produce

en la transición en función de las inhomogeneidades tanto para el exponente α como para la resistencia $R = V/I$, manifestándose así que las inhomogeneidades son detectables en un rango de temperaturas mayor en la resistencia R que en el exponente α.

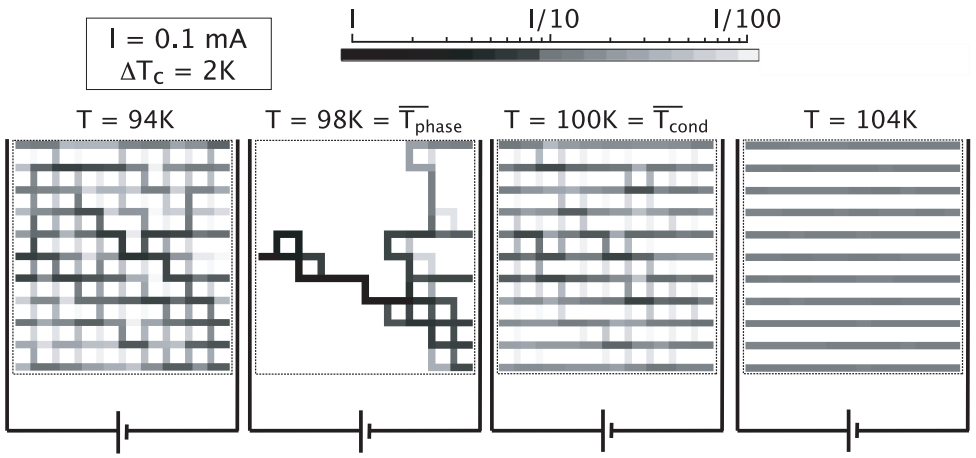

Figura 5: Ejemplo de un mapa de intensidades en un superconductor alrededor de la transición BKT obtenidas mediante simulación por elementos finitos para varias temperaturas.

Además, hemos implementado cálculos de medio efectivo en lugar de cálculos mediante elementos finitos en las mismas muestras y hemos obtenido que los resultados de ambos métodos concuerdan bien a excepción de la región cercana a $\overline{T}_{\rm phase}$, donde aparecen fuertes redistribuciones de corriente que provocan caminos percolativos, siendo así necesario un cálculo más detallado en lugar de uno basado en interpolaciones. Estos cálculos numéricos han dado lugar a dos publicaciones: N. Cotón *et al.*, *Supercond. Sci. Technol.* **24**, 085013 (2011) y N. Cotón *et al.*, *J. Supercond. Nov. Mag.* DOI 10.1007/s10948-013-2129-0, (2013).

Medida de las temperaturas $T_{\rm phase}$ y $T_{\rm cond}$.

Finalmente, para la localización de $T_{\rm phase}$ y $T_{\rm cond}$ e función del dopaje x, en base a nuestra disponibilidad de muestras y resultados teóricos, hemos implementado medidas de las curvas $V - I$ cerca de la transición superconductora en nuestras películas (abarcando, por lo tanto, todo el rango de dopajes). En particular, se midieron las curvas $V - I$ en función de la temperatura T, obteniendo el exponente α en la relación $V \propto I^{\alpha}$ (extrayéndolo a partir de la región de campo eléctrico $0.1 < E < 10^{-3}$ V/cm), así como también la resistencia óhmica V/I cuando $\alpha = 1$. Los resultados de estas medidas se pueden ver en la figura 8 (para una muestra subdopada), en la figura 9 (para una muestra óptimamente dopada) y en la figura 10 (para una muestra sobredopada). En los paneles (a) de estas figuras se muestran las curvas de campo eléctrico en función de la

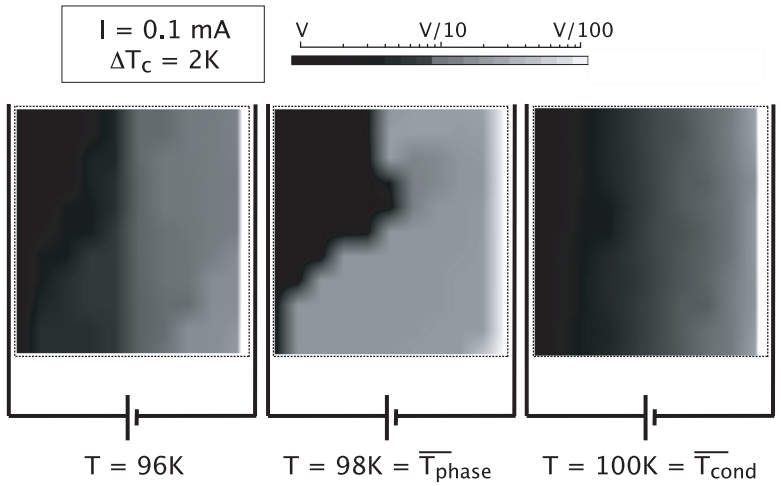

Figura 6: Ejemplo de un mapa de voltajes en un superconductor alrededor de la transición BKT obtenidas mediante simulación por elementos finitos para varias temperaturas.

densidad de corriente y en sus insets, se puede ver el exponente α obtenido en cada caso. En los paneles (b) se observan los datos experimentales de la resistividad, junto con sus correspondientes backgrounds (línea discontinua verde) y ajustes por teoría de medio efectivo (línea contínua azul oscura). También se destacan en estos paneles (b) las temperaturas T_{phase} (cuadrados rojos) y T_{cond} (rombos azul claro), así como la derivada de la resistividad en los insets. Una exploración directa de la condición $\alpha = 3$ en estas medidas nos permitió representar un diagrama de fases para T_{phase} en función del dopaje x. El diagrama de fases para $T_{\mathrm{cond}}(x)$ también se obtuvo a partir de la comparación de nuestros datos de la resistividad óhmica cerca de la transición con cálculos de medio efectivo para el redondeo crítico. Las curvas obtenidas para $T_{\mathrm{cond}}(x)$ y $T_{\mathrm{phase}}(x)$ son parábolas (con una ligera depresión cerca de $x = 1/8$) paralelas entre sí y alejadas como máximo sólo 4K una de la otra (ver la figura 11). Este diagrama de fases para los HTS sugiere escenarios teóricos diferentes a los modelos basados en fuertes fluctuaciones de la fase. Sin embargo, sí podemos afirmar que nuestros resultados son coherentes con los escenarios de fluctuaciones convencionales. Como resultado de esta parte de la tesis, está previsto el envío de un artículo a una revista del campo científico correspondiente.

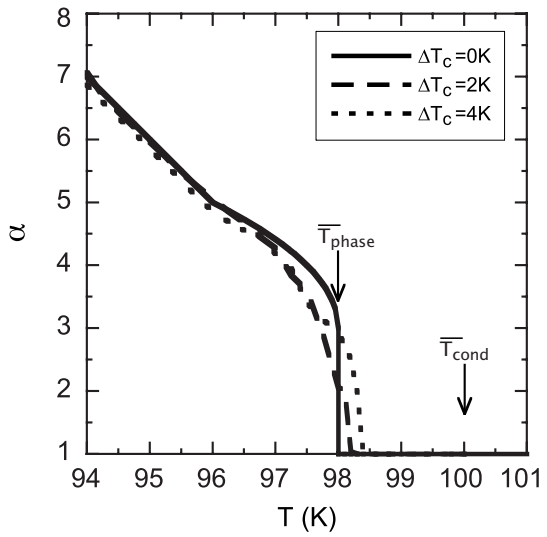

Figura 7: Exponente α en la relación $V \propto I^{\alpha}$ obtenido a partir de la pendiente de las curvas $V - I$ en la región de voltajes $3 < V < 30$ μV.

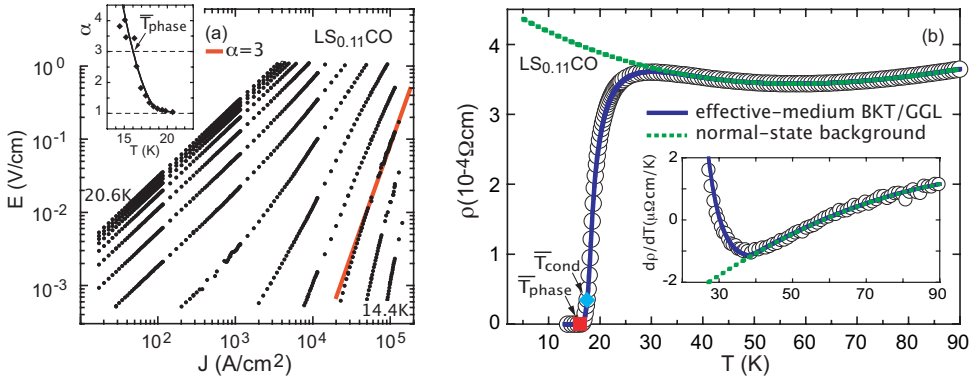

Figura 8: Medidas de las curvas $E - J$ y de la resistividad en una película subdopada de $La_{1.89}Sr_{0.11}CuO_4$.

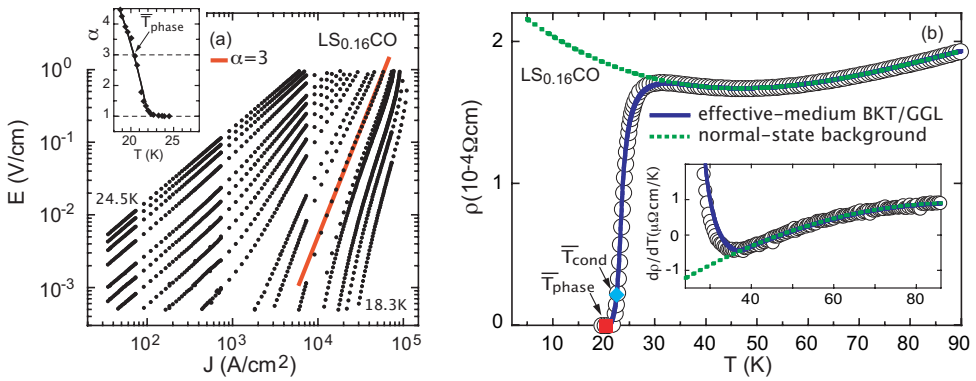

Figura 9: Medidas de las curvas $E - J$ y de la resistividad en una película con dopaje óptimo(x=0.16) de $La_{2-x}Sr_xCuO_4$.

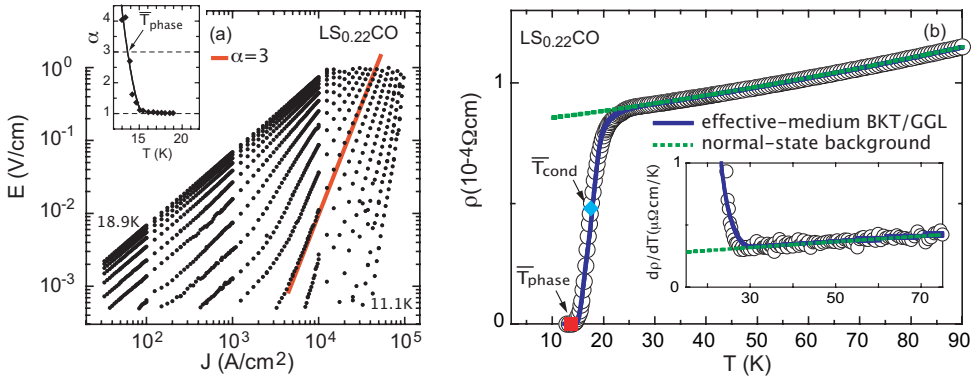

Figura 10: Medidas de las curvas $E - J$ y de la resistividad en una película sobredopada de $La_{1.81}Sr_{0.19}CuO_4$.

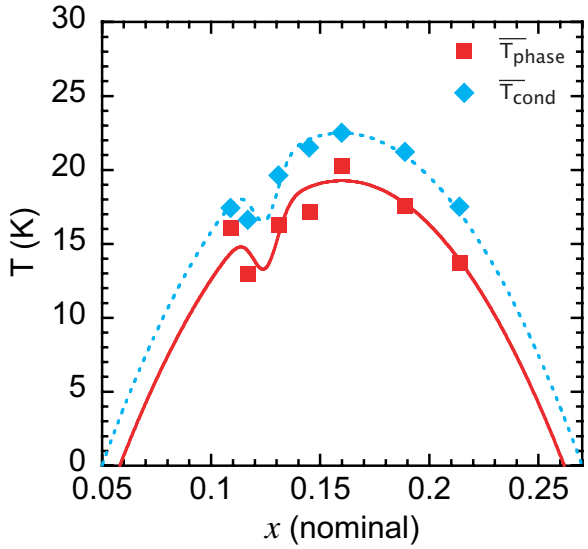

Figura 11: Diagrama de fases para las muestras de $La_{2-x}Sr_xCuO_4$ medidas en esta tesis.

USC
UNIVERSIDADE
DE SANTIAGO
DE COMPOSTELA

USC
UNIVERSIDADE
DE SANTIAGO
DE COMPOSTELA

Noelia Cotón publications

The following is a list of published (or accepted for publication) works authored by Noelia Cotón related to this thesis, presenting investigations of different aspects of the superconducting transition in cuprates:

- N. Cotón, F.J. Guzmán, M.V. Ramallo, A. Ríos, C. Torrón and F. Vidal, *Thermal fluctuations near a phase transition probed through the electrical resistivity of high-temperature superconductors*, Am. J. Phys. **78**, 3 (2010).
- N. Cotón, M.V. Ramallo and F. Vidal, *Effects of critical temperature inhomogeneities on the voltage-current characteristics of a planar superconductor near the Berezinskii-Kosterlitz-Thouless transition*, Supercond. Sci. Technol **24**, 085013 (2011).
- N. Mori, H. Enomoto, Y. Takano, N. Cotón and M.V. Ramallo, *Superconducting fluctuations of the specific heat in the short wavelength fluctuation regime*, Physics Procedia **27**, 68 (2012).
- J.D. Dancausa, N. Cotón, J.M. Doval, J. Mosqueira, M.V. Ramallo, A. Ramos-Álvarez, R.I. Rey and F. Vidal, *New Results on the Anomalous Precursor Diamagnetism in the Underdoped* $La_{1.9}Sr_{0.10}CuO_4$ *Superconductor*, J. Supercond. Nov. Magn., **26**, 1115 (2013).
- R.I. Rey, J. Mosqueira, N. Cotón, J.D. Dancausa, J.M. Doval, A. Ramos-Álvarez, A. Wahl, M. Tello and F. Vidal, *Angular Dependence of the Fluctuation Magnetization Vector Above the Superconducting Transition of a Highly Anisotropic High-*T_c *Cuprate*, J. Supercond. Nov. Magn., **26**, 1119 (2013).
- F. Soto, N. Cotón, J.D. Dancausa, J.M. Doval, A. Ramos-Álvarez, R.I. Rey, L. Rodríguez, C. Carballeira, J. Mosqueira, M.V. Ramallo and F. Vidal, *Precursor superconducting diamagnetism in* $YBa_2Cu_3O_{7-\delta}$ *with in-plane or intercalated magnetic impurities*, Supercond. Sci. Technol., **26**, 045007 (2013).
- N. Cotón, J.D. Dancausa, J.M. Doval, M.V. Ramallo, A. Ramos-Álvarez, R.I. Rey and F. Vidal, *Finite-Element and Effective-Medium Calculations of the Electrical*

Behaviour Near the Vortex-Antivortex Binding Transition of Planar Superconductors with Critical Temperature Inhomogeneities, J. Supercond. Nov. Magn., DOI 10.1007/s10948-013-2129-0 (2013).

- N. Cotón, B. Mercey, J. Mosqueira, M.V. Ramallo and F. Vidal, *Synthesis from separate oxide targets of high quality* $La_{2-x}Sr_xCuO_4$ *thin films and dependence with doping of their superconducting transition width*, accepted for publication at Supercond. Sci. Technol.